# INVESTIGATING THE OPTICAL SIGNALS IN THE BRAIN AND SPINAL CORD DURING NOCICEPTION

by

JI-WEI HE

Presented to the Faculty of the Graduate School of
The University of Texas at Arlington in Partial Fulfillment
of the Requirements
for the Degree of

DOCTOR OF PHILOSOPHY

THE UNIVERSITY OF TEXAS AT ARLINGTON
May 2010

Copyright © by Ji-Wei He 2010

All Rights Reserved

ACKNOWLEDGEMENTS

I am heartily grateful to my parents for their consistent financial and spiritual supports. Without them, I could not achieve anything in my life. For the past five years, after I joined UT Arlington, I received enormous help from my mentor, Dr. Yuan Bo Peng, and many faculties from psychology and other departments. I really appreciate their patience and passion on guiding me through a big transition from an engineer to a scientist.

Particularly, for my dissertation work, I have heartfelt gratitude to all my committee members, Drs. Yuan Bo Peng, Hanli Liu, Perry Fuchs, Linda Perrotti and Andrew Baum, for their constructive advice on experimental design and writing. I am also grateful to Christopher Hagains, Vijayalakshmi Chinta, Farah Maqsood, Sweta Narvenkar, Amuktha Rao, Venkatagir Krishnamurthy, Sudeep Upadhye, Hanan Elfallal, Manish Khatiwada, Binod Thapa, Nimit Patel, Vikrant Sharma, Fenghua Tian and Ted Huppert for their generous assistance on data collection, instrumentation support and data processing. I'd also like to thank Drs. Pablo Mora and Angela Dougall, and Jason Popan for their valuable suggestion on statistical analysis. Finally, I greatly appreciate the Neural Systems and Graphic Computing Laboratory at the University of Oslo in Norway for their 3-D rat brain atlas software package.

May 4, 2010

ABSTRACT

INVESTIGATING THE OPTICAL SIGNALS IN
THE BRAIN AND SPINAL CORD
DURING NOCICEPTION

Ji-Wei He, PhD

The University of Texas at Arlington, 2010

Supervising Professor: Yuan Bo Peng

Neuroimaging technologies have been widely used to study brain functioning based on a tight correlation between neurons and neighboring vasculature during neural activation, called neurovascular coupling. However, many studies suggested some degree of uncoupling. Optical techniques are unique tools to directly measure tissue oxygen dynamics and other physiological parameters to reflect local metabolism. The objective of my dissertation was to seek for biomarkers of pain in the brain and spinal cord. Two distinct optical methods were used in an *in vivo* rat model, including a diffuse optical imager to monitor the whole brain-scaled hemodynamics and a fiber optic system to detect focal hemodynamics and light scattering alternation in the spinal cord and primary somatosensory cortex (SI). Results were summarized in four manuscripts, which were reorganized into four chapters in this report. In particular, Chapters 1 and 2 focused on hemodynamic signatures of formalin- and mechanical pinch-induced nociception (i.e. an objective description of pain perception) over a whole rat brain, respectively. Chapter 3 described a validation of the fiber optic system in a periphery

inflammation model. Finally, Chapter 4 discussed functional significances of multiple physiological parameters collected by the fiber optical system. In conclusion, hemodynamic signatures of nociception tended to be stimulus- and brain region-dependent. A brief noxious stimulus tended to induce a regional hyperemia, whereas a decrease in regional oxygen saturation rate (i.e. the proportion of oxy-hemoglobin concentration in total-hemoglobin concentration) tended to be a reliable indicator of sustained nociception in the spinal cord and SI. Moreover, over a whole brain, a noxious stimulus tended to induce a different pattern of hemodynamics, from which was shown during innocuous somatosensory stimulation and reported by other studies with visual stimulation and motor tasks. As hemodynamic parameters reflect a balance of oxygen supply and consumption from different aspects, optical methods provide multiple reliable measures of local metabolism during neural activation, especially in pain processing; they will benefit our understanding of brain functioning.

TABLE OF CONTENTS

LIST OF ILLUSTRATIONS

Figure Page

LIST OF TABLES

# CHAPTER 1

# FORMALIN-INDUCED HEMODYNAMICS

## 1.1 Background

Subcutaneous injection of formalin into animal's paw produces an immediate short-term (Phase I, within the first 5 min) and then a quiescent period (10-15 min), followed by a long-term (Phase II, usually lasting more than 1 hour) nociceptive response as demonstrated by behavioral measurements (e.g. licking, paw elevation etc.) in conscious animals (Dubuisson and Dennis, 1977; Alreja et al., 1984), and single-unit electrophysiological recordings of the spinal dorsal horn neurons in anesthetized animals (Dickenson and Sullivan, 1987; Pitcher and Henry, 2002). Formalin-induced biphasic excitatory response provides a useful inflammatory pain model to study neurophysiological mechanism of the central nervous system (i.e. from the spinal cord to the brain) in nociception processing.

An increasing number of neuroimaging studies suggest that several brain areas may play critical roles of pain processing, including the primary somatosensory cortex (SI), secondary somatosensory cortex (SII), thalamus, anterior cingulate cortex (ACC), insular cortex, dorsolateral prefrontal cortex, and periaqueductal gray (PAG). In human, those brain areas were active when participants were in pain. Their activation was quantified in terms of the regional cerebral blood flow examined by positron emission tomography (PET), the blood oxygen level dependent (BOLD) signals examined by functional magnetic resonance imaging (fMRI), and the neural electrical signals examined by electroencephalography and magnetoencephalography (MEG) (Tracey and Mantyh, 2007; Seifert and Maihofner, 2009). Animal models also showed supportive evidence of the analogous brain regions participating in pain processing by using fMRI (Lowe et al., 2007), autoradiogram (Morrow et al., 1998), and electrophysiological recording techniques (Kuo and Yen, 2005). Particularly, formalin injection in

anesthetized rats elevated blood flow in the SI, thalamus, and PAG during both Phase I and II (Morrow et al., 1998). Furthermore, fMRI-BOLD signals were enhanced in the ACC and thalamus in Phase I (Shih et al., 2008).

Functional MRI uses BOLD signals to indirectly assess neuronal activities of regions of interest. There is a tight correlation between electrophysiological and BOLD signals (Logothetis et al., 2001). However, relationship between neuronal electrical activity and BOLD signal remains under debate. On the other hand, diffuse optical imaging (DOI) provides a new neuroimaging means, decoupling the changes in cerebral blood concentration from cerebral blood flow. It measures changes in oxy-hemoglobin ([HbO]), deoxy-hemoglobin ([Hb]), and total hemoglobin ([HbT]) concentration at a relatively high sampling rate. Optical imaging has been successfully used to detect brain activities (Berwick et al., 2008; Becerra et al., 2008), to mark tumor boundaries (Tromberg et al., 2005; Xu et al., 2008), and to determine peripheral vascular oxygenation changes in the skin and muscle (Quaresima et al., 2003; Davis et al., 2006). There is a reliable and strong correlation between a positive BOLD signal change and a decrease in [Hb] as derived from optical measurements in the human brain during motor tasks (Mehagnoul-Schipper et al., 2002; Huppert et al., 2006) and visual stimulation (Schroeter et al., 2006). Therefore, hemodynamic parameters offer a valuable perspective to unveil neurovascular mechanism during brain functioning.

Our goal is to understand the pain processing in multiple brain regions by means of spatial and temporal optical hemodynamic signals in response to formalin injection into rat hind paw. When light is emitted into the tissue, it will be absorbed, scattered, or reflected by the brain. Hemoglobin molecules in the cerebral circulation are the main optical absorbers. By measuring the amount of light reflected at two wavelengths, the change in light absorption due to brain activation can be calculated (Li et al., 2004; Liu et al., 2008). It was hypothesized that three components of hemodynamics (HbO, Hb, and HbT) would change as a result of the change in neuronal activities in the brain, in response to peripheral noxious formalin assault.

## 1.2 Methods

### *1.2.1 Animal Preparation*

Six male Sprague-Dawley rats were recruited. Their ages were 118.5 ± 23.4 days (mean ± SEM) and weights were 365 ± 27.1 g (mean ± SEM). All animals were initially anesthetized by intraperitoneal injection of pentobarbital sodium solution (50 mg/kg). A PE10 tubing was inserted into the jugular vein for continuous intravenous administration of pentobarbital sodium (5 mg/ml) at a fixed rate of 0.02 ml/min to maintain anesthesia during data acquisition. The scalp was removed, and the dorsal part of the skull was completely exposed. Animal's head was positioned on a stereotaxic frame to prevent any possible motion during experiment. An electrical cautery pen (Bovie, Aaron Medical, FL, US) was used to stop bleeding if necessary. All procedures were approved by the Institutional Animal Care and Use Committee (IACUC) at the University of Texas at Arlington. Procedures were also followed by the guidelines described by the Committee for Research and Ethical Issues of IASP (Zimmermann, 1983).

### *1.2.2 Formalin Injection*

After a 5-min baseline measurement, formalin solution (50 µl, 3%) was injected subcutaneously into the center of the plantar area in rat hind paw unilaterally. The injection side was pseudorandom: 3 rats on the right side, and 3 rats on the left side.

### *1.2.3 Instrumentation*

A commercialized, continuous-wave, NIRS brain imager for Dynamic Near-Infrared Optical Tomography (DYNOT, NIRx Medical Technologies, US) was used to measure hemodynamics of the rat brain continuously. Twenty-six bifurcated optical optodes (2 mm in diameter) were utilized in two wavelengths of light (760 and 830 nm), and were arranged by a plastic frame in a horizontal plane to cover the entire rat cerebrum (See details in Appendix). The sampling rate was at 2 Hz.

*1.2.4 Image Reconstruction*

Two distinct methods, tomography and topography, were used to reconstruct brain images from optical signals. Tomography provides an image at a lateral layer (i.e. in axial view) of a rat brain or tissue phantom by integrating data from all measures of source-detector pairs. This usually requires mathematical models (e.g. a diffusion of light model) and complex computations in order to reconstruct hemodynamic tomography images (Arridge, 1999; Tian et al., 2009a). Tomography was performed by HOMER (PMI, US), and Matlab (MathWorks, US). In contrast, topography provides an overall response pattern for the areas directly underneath the optic probes using a limited number of source-detector pairs. The latter one requires relatively simple calculations without use of diffusion theory. Topography was performed by Matlab. Detailed procedures for both methods could be found in Appendix.

*1.2.5 Statistical Analysis*

One-sample t-test was used for each pixel of tomographic image (as well as each subdivision of topographic image) to assess a statistical significance of hemodynamic change in [HbO], [Hb], and [HbT] at a given time point with one tail assumption (Matlab). Several isolable regions of interest (ROIs) of tomography were defined on a basis of the previous t test results. For each ROI, an averaged value over a 3X3-pixels-square (where the center pixel was determined by a regional maximum) was used as a dependent variable. A one-way within-subject ANOVA with 10 time levels (e.g. 5 s before injection and 5 - 50 min post injection in a 5-min-bin) was utilized to assess any statistically significant change post injection in [HbO], [Hb], and [HbT], respectively. Post hoc multiple comparisons between baseline and all the other time levels were performed with Bonferroni correction if a main effect occurred. The ANOVAs and post hoc tests were performed by SAS (SAS, US). Alpha = .05.

## 1.3 Results

### *1.3.1 Comparison between Topography and Tomography*

The hemodynamic changes of the rat brain were reconstructed in tomographic (left panel in Figure 1.1) and topographic images (right panel in Figure 1.1). General patterns of hemodynamics after formalin injection are shown in [HbO], [Hb], and [HbT] over 6 rats at 10 selected time points. Side-by-side comparisons of images between two reconstruction methods indicated that (a) a short-term increase in [HbO] tended to occur within the first 5 min post formalin injection, followed by a long-term monotonic decrease over the whole brain (top row in Figure 1.1), (b) a short-term decrease in [Hb] tended to occur within the first 5 min post injection, followed by a long-term monotonic increase over nearly entire brain (middle row in Figure 1.1), and (c) a decrease in [HbT] tended to occur at some isolated areas after 5 min post injection (bottom row in Figure 1.1). In light of the fact that tomography used 100% source-detector pairs (676) with a diffuse light mathematical model, whereas topography only used 1.8% of total source-detector pairs (12 out of 676), spatial resolution of tomography was better than that of topography as expected. On the other hand, the comparisons also demonstrated validity of the mathematical model used in tomography in this pragmatic scenario. Based on the tomographic hemodynamic responses, five regions of interest (ROIs) in anterior midline, lateral, central midline, and posterior midline areas were selected for further analysis to reveal their temporal profiles.

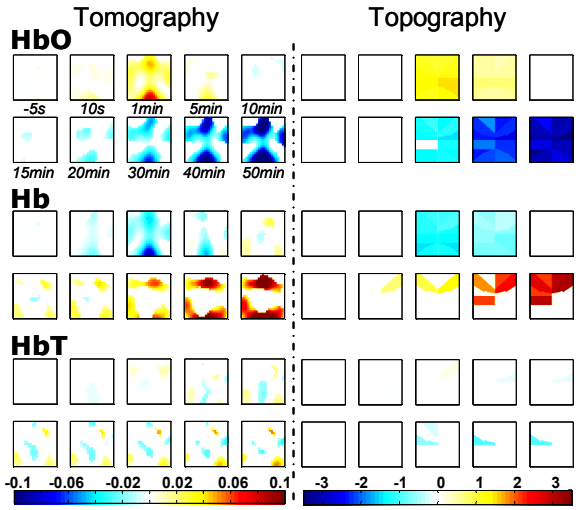


Figure 1.1 A Comparison between Tomography (left panel; at a depth of 5 mm below optode array) and Topography (right). On each panel, there are 3 blocks: top ([HbO]), middle ([Hb]), and bottom ([HbT]). Within each block, there are 10 images at selected time points. Visualization of tomography and topography was determined by statistical significance ($n$ = 6) and an averaged intensity of signal changes over animals at a specific time point. White color indicates no significant change. Blue color (towards left on the color bar at the bottom) indicates a significant decrease, whereas red color (towards right) indicates an increase. Color map was generated in a linear manner as related to the intensity of change. Image directions: right indicates ipsilateral side; left contralateral; top rostral; bottom caudal.

*1.3.2 Temporal Profiles of ROIs in Tomography*

Five ROIs were identified by a maximal change in tomographic images at a specific time point, respectively (See the last column of Table 1.1). As marked by crossline in images at some typical time points post formalin injection, these five ROIs include the anterior midline (Figure 1.2A), contralateral (Figure 1.3A), ipsilateral (Figure 1.4A), central midline (Figure 1.5A), and posterior midline (Figure 1.6A). At each ROI, hemodynamic responses were analyzed for the initial 300 s (Figures 1.2-6B) and the entire 50 min (Figures 1.2-6C) post injection, respectively. For an ease of visualization, error bars were shown at only few time points. After grouping all time points into 11 bins (shown in Figures 1.2-6D), one-way within-subject ANOVAs were performed (shown in Table 1.1), and post hoc analyses with Bonferroni error correction were conducted accordingly.

Table 1.1 Statistics of Hemodynamics Over Time in [HbO], [Hb], and [HbT] at Five ROIs. One-way within-subject ANOVA was utilized to assess each hemodynamic over 11 time levels, including 5-s-baseline, and 5-50 min post injection with a 5-min-bin. The depth of tomographic images for each ROI is shown, along with a brief explanation of how to location such ROI.

| ROI | Area | [HbO] | [Hb] | [HbT] | Img Dept (mm) | Center Location |
|---|---|---|---|---|---|---|
| 1 | Anterior midline | $F(10,50) = 12.2$ $p < .001$ (*) | $F(10, 50) = 7.63$ $p < .001$ (*) | $F(10,50) = .97$ $p = .48$ | 3 | A maximal increase in [HbO] at 1 min |
| 2 | Contralateral | $F(10,50) = 5.42$ $p < .001$ (*) | $F(10,50) = 3.62$ $p = .001$ (*) | $F(10,50) = 3.0$ $p = .98$ | 2 | A maximal decrease in [HbO] at 10 min |
| 3 | Ipsilateral | $F(10,40) = 17.9$ $p < .001$ (*) | $F(10,40) = 11.6$ $p < .001$ (*) | $F(10,40) = 5.84$ $p < .001$ (*) | 6 | A maximal increase in [HbO] at 1 min |
| 4 | Central midline | $F(10,50) = 11.4$ $p < .001$ (*) | $F(10,50) = .99$ $p = . 46$ | $F(10,50) = 1.77$ $p = .091$ | 6 | A maximal decrease in [Hb] at 10 min |
| 5 | Posterior midline | $F(10,50) = 13.8$ $p < .001$ (*) | $F(10,50) = 9.30$ $p < .001$ (*) | $F(10,50) = .62$ $p = .79$ | 6 | A maximal increase in [HbO] at 1 min |

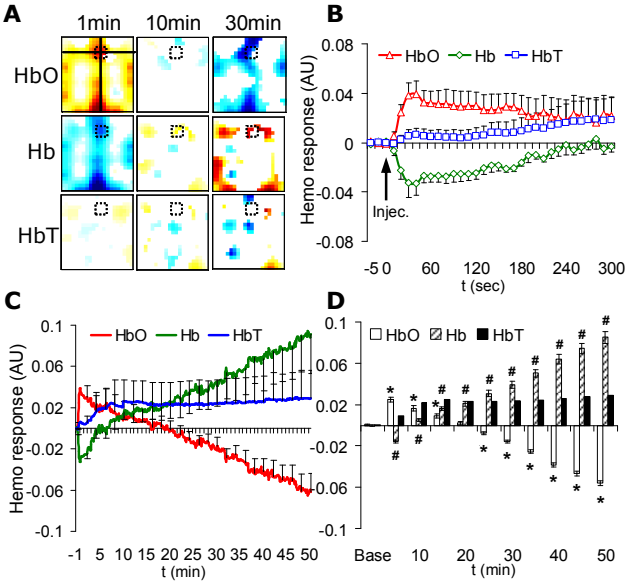


Figure 1.2 Summary of Temporal Tomographic Hemodynamic Change in The Anterior Midline ROI. Dependent variable was an average of a 3-by-3-pixels area (shown in A) for each chromophore. Changes in [HbO], [Hb], and [HbT] (in arbitrary unit) are plotted in the first 300 s (B), the full 50 min (C), and another full 50 min in 5-min-bin (D) post injection. In D, post hoc significant differences ($p < .05$) over baseline were noted by * for [HbO], # for [Hb], and + for [HbT] at corresponding time levels. In B, C, D, the error bar presents SEM ($n = 6$).

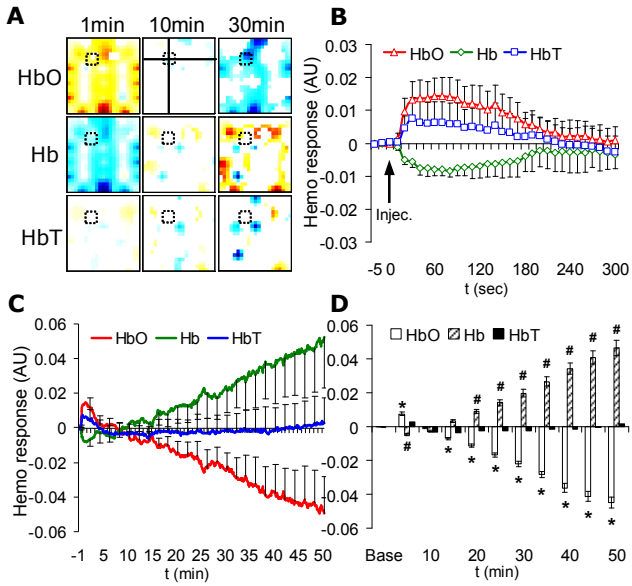


Figure 1.3 Summary of Temporal Tomographic Hemodynamic Change in The Contralateral ROI (*n* = 6). Similar instructions can be found in caption of Figure 1.2.

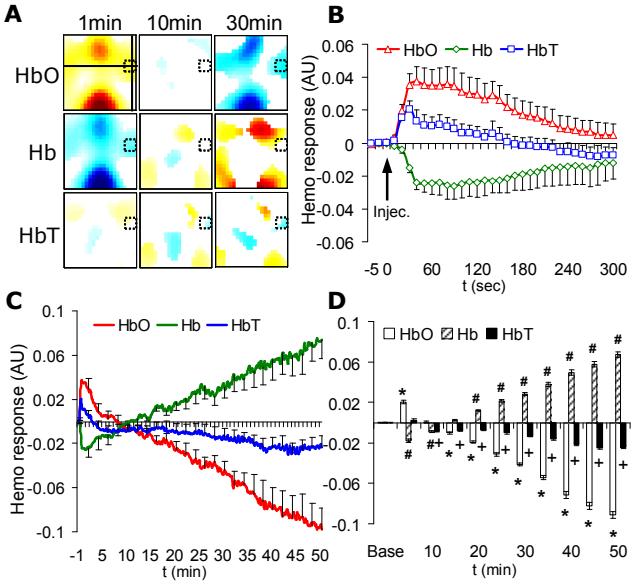


Figure 1.4 Summary of Temporal Tomographic Hemodynamic Change in The Ipsilateral ROI (*n* = 5). Similar instructions can be found in caption of Figure 1.2.

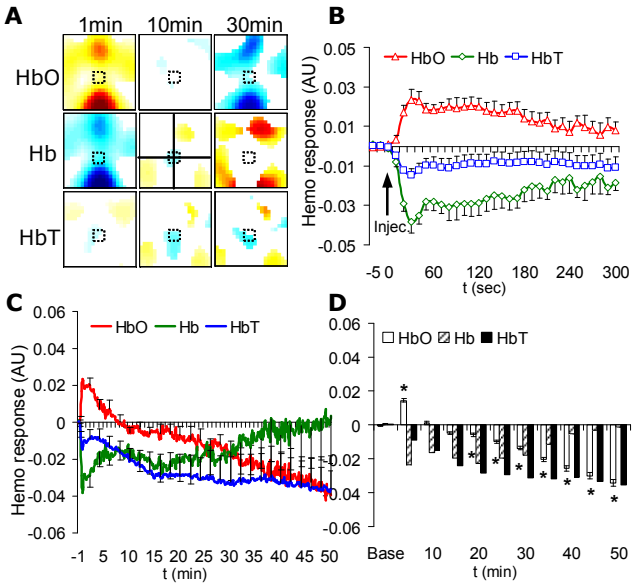


Figure 1.5 Summary of Temporal Tomographic Hemodynamic Change in The Central Midline ROI (*n* = 6). Similar instructions can be found in caption of Figure 1.2.

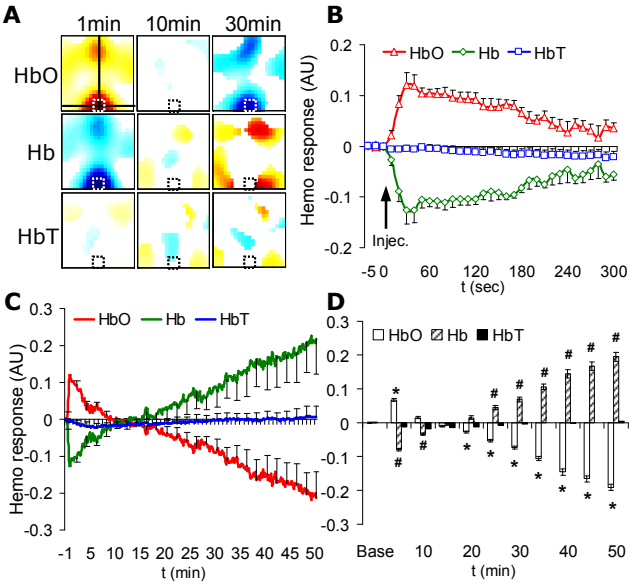


Figure 1.6 Summary of Temporal Tomographic Hemodynamic Change in The Posterior Midline ROI (*n* = 6). Similar instructions can be found in caption of Figure 1.2.

In general, there were significant changes in [HbO] over time at all five ROIs (Table 1.1). Specifically, significant initial increases were found at 5 min post injection (Figures 1.2-6D).

This effect returned to baseline level between 10 and 20 min. Immediate after that, a continuous monotonic decrease persisted up to 50 min. Significant changes were also found in [Hb] over time at all ROIs, except the one on the central midline (Table 1.1). Particularly, significant initial decreases were observed at 5 min post injection (Figures 1.2-4, 5D). Similar to [HbO], this effect returned to baseline level between 10 and 20 min. It was followed by a continuous monotonic increase persisted up to 50 min. Unlike the [HbO] or [Hb], the regional [HbT] failed to show significant changes in these ROIs, except on the ipsilateral side (Table 1.1). At this ROI, a decrease occurred at 10 min and sustained up to 50 min. It was noteworthy that one animal was excluded at the ROI on the ipsilateral side, because a sudden step-wise regional increase in [HbT] was observed at 10 min. A regional bleeding on the skull was noted at the same site after removal of the optode-array at the end of experiment.

*1.3.3 Identification of ROIs*

Four 3D representations of a rat brain atlas are shown in dorsal (Figure 1.7A), coronal (Figure 1.7B), sagittal (Figure 1.7C), and dorsolateral (Figure 1.7D) view (Atlas3D, NeSys, Oslo, Norway). Five well-known pain-processing-related brain nuclei are highlighted in colors. The ROI on the anterior midline (Region #1) completely overlaps the anterior portion of the Cg1 (in red), and some part of the Cg2 (in green; beneath the Cg1; visible in Figures 7B and 7C). The ROI on the contralateral side (Region #2) overlaps the anterior tip of the contralateral SI (in yellow). The ROI on the ipsilateral side (Region #3) moderately overlaps the anterior portion of the SII (in pink). Some tomographic images in [HbO] and [Hb] shown in Figure 1.1 indicate concomitant responses in the contralateral region (a symmetrical area of the Region #3). This area is located more laterally than Region #2 in the contralateral hemisphere, and partially overlaps the anterior contralateral SII. The ROI on the central midline (Region #4) completely overlaps the thalamus (in light blue). The ROI on the posterior midline (Region #5) heavily overlaps the posterior port of the PAG (in blue). A rectangle in dash line outlines the size of

DYNOT optode array, where five aforementioned ROIs are labeled numerically and sequentially (Figure1. 7A).

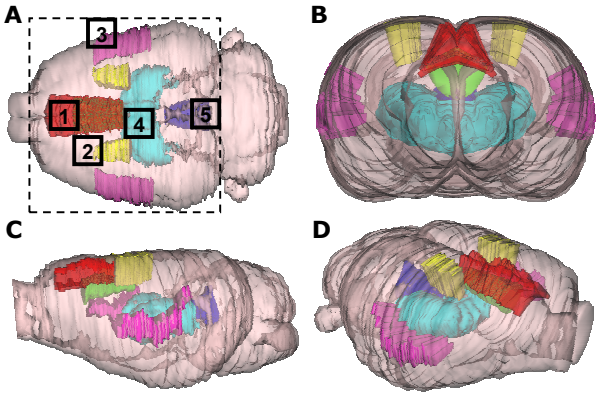


Figure 1.7 Identification of ROIs in a 3-D rat atlas (Atlas3D, NeSys, Oslo, Norway) in a dorsal-ventral (A), a coronal (B), a sagittal (C), and a dorsolateral (D) orientation. Several pain-processing-related brain regions are labeled in colors: red for the dorsal ACC (Cg1); green for the ventral ACC (Cg2); yellow for the SI; pink for the SII; light blue for the thalamus; and blue for the PAG. Size of the reconstructed tomographic image is shown by a dashed rectangle. Five ROIs described in Table 1 (labeled from 1 to 5) are the anterior midline, contralateral, ipsilateral, central midline, and posterior midline regions.

## 1.4 Discussion

We found that (i) NIR tomography was capable of detecting functional hemodynamics in an entire rat cerebral brain with good spatial and temporal resolutions. (ii) Following formalin injection, five identifiable brain regions were highly activated, in which [HbO] and [Hb] tended to change with opposite directions in time-resolved patterns. A different pattern from the formalin biphasic response was observed by current knowledge. (iii) By overlapping with a 3D rat brain atlas, the five activated brain regions were highly correlated with the ACC, SI/II, thalamus, and PAG. These regions are well-known for their roles in pain processing.

### *1.4.1 Physiological Significance of Hemodynamics*

Speaking of the formalin-induced nociception, we observed a clear biphasic pattern of changes in [HbO] and [Hb] over most ROIs in 50 min post formalin injection (Figures 1.2-6C). Except with the direction of hemodynamic response in Phase II, this pattern was correlated well

to a formalin-induced response as examined by behavioral (Dubuisson and Dennis, 1977) and electrophysiological techniques (Dickenson and Sullivan, 1987), indicating a neurovascular substrate of the formalin-induced nociception in the rat brain.

More importantly, our data were the first time to suggest a functional significance of a unique decrease in [HbO] paired with an increase in [Hb] in pain processing. Historically, an increase in [HbO] with a concomitant decrease in [Hb] was believed to be a typical hemodynamic signature of brain functioning (Villringer et al., 1993). Functional NIRI studies in humans with visual (Seiyama et al., 2004; Schroeter et al., 2006), somatosensory stimulations (Seiyama et al., 2004; Becerra et al., 2008) and motor tasks (Huppert et al., 2006) had provided converging evidence to this pattern of neurovascular coupling signature (i.e. a relationship between local neuronal activity and vascular perturbation during brain functioning) in related cortices. However, this signature was less likely to be found in the frontal area in a heat pain (Becerra et al., 2008), and instead, a reversed pattern, i.e. a decrease in [HbO] with an increase in [Hb], was found in a prefrontal area in anagram tasks (Tian et al., 2009b). Thus, a hemodynamic signature tends to depend on the region of the brain and a task that the brain engages in. When the brain receives input (e.g. noxious formalin injection), neurons in a functionally-related brain areas (e.g. the thalamus, SI, SII, ACC, and PAG) are activated with an increasing demand of oxygen (e.g. the first 5 min post formalin injection). Local vascular structures respond to this demand by providing more HbO through arterial vasodilatation with increased volume and velocity, bumping up speeds of releasing oxygen from HbO, moving Hb to venules, and accelerating the transportation of Hb away from the site. This results an increase in [HbO] and a decrease in [Hb]. If the brain activation is relatively brief, there is no need for additional oxygen, and the local vascular tension is, therefore, released. However, if the peripheral input is long-lasting (e.g. second phase of formalin), there is a constant demand for oxygen. Local vascular bed will, sooner or later, reach to its limit to further dilate the vessels, reaching the ceiling effect. At this time, an initial increase in [HbO] cannot maintain by

vasodilatation and arterial blood influx. [HbO] will decrease as the neuronal oxygen consumption still remains at high level. Meanwhile, local vascular structure cannot remove the accumulated Hb efficiently when the vascular capability also reaches at a ceiling level. Therefore, [Hb] will increase, as observed in the Phase II of formalin-induced nociception.

*1.4.2 Comparison between The Results in NIR Hemodynamics and FMRI-BOLD Signal*

The fMRI-BOLD signal was shown to be related to blood oxygen dynamic in the brain (Ogawa et al., 1990). A positive fMRI-BOLD signal was believed to reflect an increased neuronal activity. This notion was supported by studies with simultaneous recordings of both neuronal electrical signals and local BOLD response (Logothetis et al., 2001; Goense and Logothetis, 2008). On the other hand, a negative BOLD was shown to be associated with a decreased neuronal activity (Shmuel et al., 2006; Pasley et al., 2007). However, a recent study indicated that negative BOLD signals were concurrent with an increased neuronal activity (Schridde et al., 2008). In addition, negative BOLD signals were pervasively observed, and produced conflicting results between studies. For instance, in pain studies, a positive BOLD signal was shown in the ACC in response to painful stimulation in humans (Peyron et al., 2000; Ruehle et al., 2006), whereas a negative BOLD signal was also presented in the same region in human (Mohr et al., 2005; Lui et al., 2008) and animal (Lowe et al., 2007) models. A substantial proportion of neurons in the ACC were responsive to various painful stimuli as examined by electrophysiological and immunohistochemical techniques in various species (Shyu et al., 2008; Sikes et al., 2008). Thus, despite that a positive BOLD signal is a reliable indicator of neuronal excitation, a negative BOLD signal does not necessarily indicate neuronal inhibition. The origin of a BOLD signal was suggested to depend on several factors, such as region, pathological condition (e.g. normal subject or subject with diseases), state (e.g. related to a task a subject is assigned to perform) (Schridde et al., 2008).

The BOLD signal is influenced by numerous vascular parameters, including the cerebral blood flow, blood volume, and oxygen-related metabolic rate (Ogawa et al., 1990).

These parameters are also correlated to the NIR hemodynamic components, i.e. [HbO], [Hb], and [HbT]. Human subject studies with simultaneous fMRI-NIR measures revealed a strong relationship between a positive BOLD response and a decrease in [Hb] under visual, somatic sensory stimulations, and motor tasks (Mehagnoul-Schipper et al., 2002; Huppert et al., 2006; Sakatani et al., 2007). Our observations of a decrease in [Hb] in the ACC, SI, and PAG during the first 5 min were in line with fMRI studies, in which an enhanced BOLD signal was detected in the corresponding regions in response to formalin injection (Shah et al., 2005; Shih et al., 2008) or other noxious stimuli (Malisza et al., 2003; Hess et al., 2007).

According to our data, [Hb] change was followed by a curvilinear manner over time, and a prolonged increase in [Hb] was observed in the late phase (15 to 50 min post injection; Figures 2-6). However, BOLD signal demonstrated a monotonic increase and a plateau up to 90 min (Shah et al., 2005). The discrepancy suggested that relationship between hemodynamic response and BOLD signal was dependent on a stimulus and a state of the brain (e.g. processing an acute pain or sustained pain). In other words, a [Hb] decrease is not an exclusive and universal indicator of a positive BOLD. In our sustained pain condition, a [Hb] increase was also a reliable indicator of an increased cell metabolism, and in turn, was related to a positive BOLD. Furthermore, as depicted by our data, the hemodynamic response produced a more meaningful picture of the formalin-induced response than fMRI-BOLD did. The NIR hemodynamic signals provide a promising way to understand the neurovascular coupling and may provide a potential biomarker for such a noxious stimulus.

# CHAPTER 2

# MECHANICAL PINCH-INDUCED HEMODYNAMICS

## 2.1 Background

Many noninvasive neuroimaging technologies profoundly benefited our understanding of neurophysiology of brain activation in the last decade, such as positron emission tomography (PET), and functional magnetic resonance imaging (fMRI). These methods do not directly measure the neuronal electrical signal, but the neighboring vascular dynamic. The physiological relevance of the vascular dynamic during neuron functioning (i.e. termed neurovascular coupling) is not clearly established. For example, fMRI uses the blood-oxygen-level dependent (BOLD) signal to reflect brain activity (Ogawa et al., 1990). A tight neural correlates of BOLD was indicated by using simultaneous extracellular recording techniques (Logothetis et al., 2001; Goense and Logothetis, 2008). However, a paradoxical negative BOLD signal was pervasively found in the brain during functional activation (Mohr et al., 2005; Lui et al., 2008). Contradictory findings indicated that a negative BOLD was associated with both inhibition (Shmuel et al., 2006; Pasley et al., 2007) and excitation of neuronal activities (Schridde et al., 2008).

Pain perception is a complicated process involving a cerebral network, such as the primary/secondary somatosensory cortices (SI/II)), the anterior cingulate cortex (ACC), thalamus, and midbrain periaqueductal gray (PAG), as examined by various neuroimaging techniques in human (Tracey and Mantyh, 2007; Seifert and Maihofner, 2009) and animal models (Morrow et al., 1998; Kuo and Yen, 2005; Lowe et al., 2007). Several functional near infrared imaging (fNIRI) studies have demonstrated hemodynamic response in the SI and the frontal area in responses to acute painful stimuli in human (Slater et al., 2006; Bartocci et al., 2006; Becerra et al., 2008).

In contrast to other neuroimaging methods, fNIRI provides a direct approach to assess tissue oxygen consumption by measuring oxy- ([HbO]), deoxy- ([Hb]), and total-hemoglobin concentration ([HbT]) changes with a relatively high sampling rate. These hemodynamic parameters were correlated to local field potential (Horovitz and Gore, 2004; Rovati et al., 2007; Takeuchi et al., 2009), and BOLD signal in human brain (Strangman et al., 2002; Huppert et al., 2006; Toronov et al., 2007). However, fNIRI was mainly used to detect cortical activity, due to the limitation that the near infrared light can only penetrate a few centimeters of tissue. In a small animal model, this constraint may not be critical, and hemodynamic responses in the superficial and deep brain areas can be detected.

The objective of our current study was to identify the hemodynamic pattern of brain in pain processing by using fNIRI. The relative changes in [HbO], [Hb], and [HbT] (in arbitrary unit) in response to innocuous mechanical brush and noxious pinch stimuli were calculated from fNIRI signals.

## 2.2 Methods

### *2.2.1. Animal Preparation*

Eleven male Sprague-Dawley rats were recruited, with a mean age of 96 ± 1.3 days and a mean weight of 358 ± 7.7 g. All animals were initially anesthetized by intraperitoneal injection of pentobarbital sodium solution (50 mg/kg). A PE10 tubing was inserted into the jugular vein for continuous intravenous administration of pentobarbital sodium (5 mg/ml) at a fixed rate of 0.02 ml/min to maintain anesthesia during data acquisition (Peng et al., 1996a). After an incision in the midline of the scalp, the dorsal part of the skull was completely exposed. The head was positioned on a stereotaxic frame to prevent any possible motion during experiment. An electrical cautery pen (Bovie, Aaron Medical, FL, US) was used to stop bleeding if necessary. All procedures were approved by the Institutional Animal Care and Use Committee (IACUC) at the University of Texas at Arlington. Procedures were also followed by the

guidelines described by the Committee for Research and Ethical Issues of IASP (Zimmermann, 1983).

*2.2.2 Instrumentation*

A commercialized, continuous-wave, NIRI (DYNOT, NIRx Medical Technologies, US) was used to measure hemodynamics of the rat brain continuously. Twenty-six bifurcated optical optodes (2 mm in diameter) were utilized in two wavelengths of light (760 and 830 nm), and were arranged by a plastic frame above the skull (Figure 2.1A-C). The description on optodes arrangement can be found in Appendix. The sampling rate was at 2 Hz.

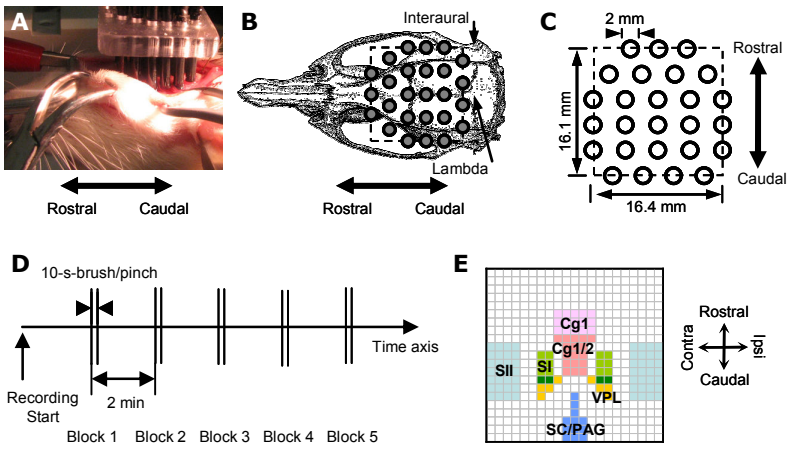


Figure 2.1 Instrumentation and Experiment Procedures. **A**: A photo presentation of optode placement on a rat dorsal skull after the scalp was removed. **B**: 26-optodes locations in the rat skull (Paxinos, 1998). **C**: Size of a reconstructed image (noted by dash line) determined by the optodes. **D**: A 5-blocks-design for 10 s brush and pinch. **E**: Segmentation of ROIs in a 21-by-21-pixels reconstructed image based on a rat atlas (Paxinos, 1998). Image directions: up, rostral; bottom, caudal; right, ipsilateral; left, contralateral. Abbreviation: Cg1, dorsal cingulate cortex area 1; Cg2, ventral cingulate cortex; SI, primary somatosensory cortex for the hind limb; SII, secondary somatosensory cortex; VPL, ventral posterolateral nucleus of thalamus; SC, superior colliculus; PAG, periaqueductal gray.

*2.2.3 Mechanical Brushing and Pinching*

Brush and pinch were applied on the plantar surface of a rat hind paw unilaterally. Innocuous brush stimulation was to briefly sweep a camel hair bush in a rhythmic fashion for 10 s. Noxious pinch was applied for 10 s by a straight arterial bulldog clamp ) (Peng et al., 1996b; Ativanichayaphong et al., 2008). Both stimulations were conducted in a block design (Figure

1D). Five consecutive brushes or pinches were applied on the same side of the paw with an interval of 2 min. Manipulation side was selected pseudorandomly: 6 rats received the stimuli on the left, and 5 on the right. Pinches were applied 5 min after brushes were completed on the same hind paw for each animal.

*2.2.4 Image Reconstruction*

Tomography was performed by an open-source software HOMER (PMI, US), and Matlab (MathWorks, US). The mathematical models and detail procedures can be found in Appendix. After a region of interest (ROI) was identified, the reconstruction depth was based on the brain structure associated with somatosensory and/or pain processing. In addition to the SI/II mentioned earlier, the ventral posterolateral nucleus (VPL) of thalamus and the superior colliculus (SC) were considered as ROIs associated with somatosensory processing. The VPL was suggested to be a critical relay center that directly receives somatosensory input from the spinothalamic tract (Boivie, 1971; Harris, 1978; Harris, 1980; Dykes et al., 1988). The SC, which lies dorsally to the PAG, was suggested to integrate multiple innocuous somatosensory inputs from the periphery including the hind limbs (Abrahams et al., 1988; Clemo and Stein, 1991; Wallace et al., 1996). Considering that the combined thickness of a rat skull, other soft tissues, and space is approximate 1 mm, the reconstructed images were set at 2, 3, 5 mm deep for SI, ACC, SC, respectively, and 6 mm deep for SII, VPL, and PAG.

*2.2.5 Segmentation of ROIs*

The reconstructed image was further divided to 21 x 21 pixels. Each pixel was registered as a specific ROI associated with somatosensory and/or pain processing based on a rat brain atlas (Paxinos, 1998). Pixels in different ROIs were filled in different colors for a better visualization (Figure 2.1E). They were the anterior part of the dorsal cingulate cortex (Cg1), the posterior part of the Cg1 and the ventral cingulate cortex (Cg2; noted by Cg1/2), the bilateral SI for the hind limb, the bilateral SII, the bilateral VPL, and the SC (for brush only) or the PAG (for pinch only). The overlapped area between the SI and VPL was colorized in dark green. The

temporal profiles of hemodynamic responses (i.e. [HbO], [Hb], or [HbT]) in a ROI were obtained by averaging of all pixels in the same region at each time point.

*2.2.6 Statistical Analysis*

A directional one-sample t test was utilized to assess any significant hemodynamic changes in [HbO], [Hb], and [HbT]. Alpha level was set at 0.05. All data were expressed in mean ± standard error of the mean (SEM). All statistical analyses were performed in either Matlab or SPSS 17.0 (SPSS Inc. US).

## 2.3 Results

Typical reconstructed horizontal images at 5 mm demonstrates responses to brush (upper row) and pinch (lower row), where [HbO], [Hb], and [HbT] changes (from left to right) are shown at several time points (Figure 2.2). Reconstructed images at different depths (2-6 mm) had no principle difference in the spatial profile of hemodynamic responses (data not shown). Generally, an increase in [HbO], and a decrease in [Hb] were observed at multiple regions for brush, whereas such changes were observed at fewer regions for pinch. It is noteworthy that one rat out of eleven was removed for brush, because of a global decrease in [HbO] and an increase in [Hb] for over a minute. The magnitudes of such responses at some regions were as great as 8.19-fold of standard deviation over all the other subjects. Thus, the sample size for brush was 10, and the sample size for pinch remained 11.

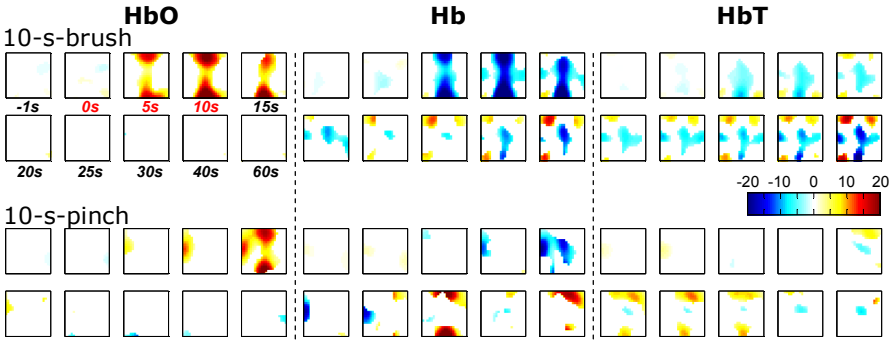


Figure 2.2 Hemodynamic Responses to Innocuous 10 s-Brush (upper row) and Noxious 10 s-Pinch (lower row) in [HbO], [Hb], and [HbT] Changes (in arbitrary unit). 10 typical time points were selected. The reconstruction depth was 5 mm. Color denotes the intensity of a hemodynamic response only if such response reached to a statistical significance at each pixel

by a one-sample t test (for brush: $n$ = 10; for pinch: $n$ =11). Particularly, red indicates a significant increase; blue a decrease; white a non-significant change.

The temporal profiles of hemodynamic responses to brush (Figure 2.3) and pinch (Figure 2.4) were shown at all nine ROIs. It appeared that brush tended to produce hemodynamic responses between 0 and 30 s, and the peak responses tended to occur within a 20 s period. Pinch, however, tended to produce a more dynamic response over time. In order to compare the brush- and pinch-induced responses in a controlled manner, we systemically used a maximal response in the 20 s-window (Max) and an overall response in the 30 s-window (Area) at all ROIs as two dependent variables for statistical analysis, respectively. It is worth mentioning that the spatial and temporal patterns of reconstructed images at depths of 5 and 6 mm were similar for brush and pinch (data not shown). In light of the functional differences between the SC and PAG during somatosensory processing (see details in Methods), we only selected a depth at 5 mm for brush (SC in Figure 2.3), and 6 mm (PAG in Figure 2.4) for pinch to obtain the hemodynamic responses at the posterior medial area.

*2.3.1 Brush-Elicited Hemodynamics*

Compared to the baseline, a typical increase in [HbO] coupled with a decrease in [Hb] was indicated in the ACC, bilateral SI, and SC (Table 2.1). No statistically significant response in the SII was able to be detected. In the VPL, an increase in [HbO] was indicated only in the contralateral hemisphere, whereas a decrease in [Hb] was shown bilaterally. A decrease in [HbT] was suggested in the ACC, ipsilateral VPL, and SC. In addition, lateralization was found only in the SI (pair-wised t test; Area in [Hb]: $t(9) = -1.91$, $p = 0.044$), which indicated that the ipsilateral SI showed a greater decrease in [Hb] than the contralateral side.

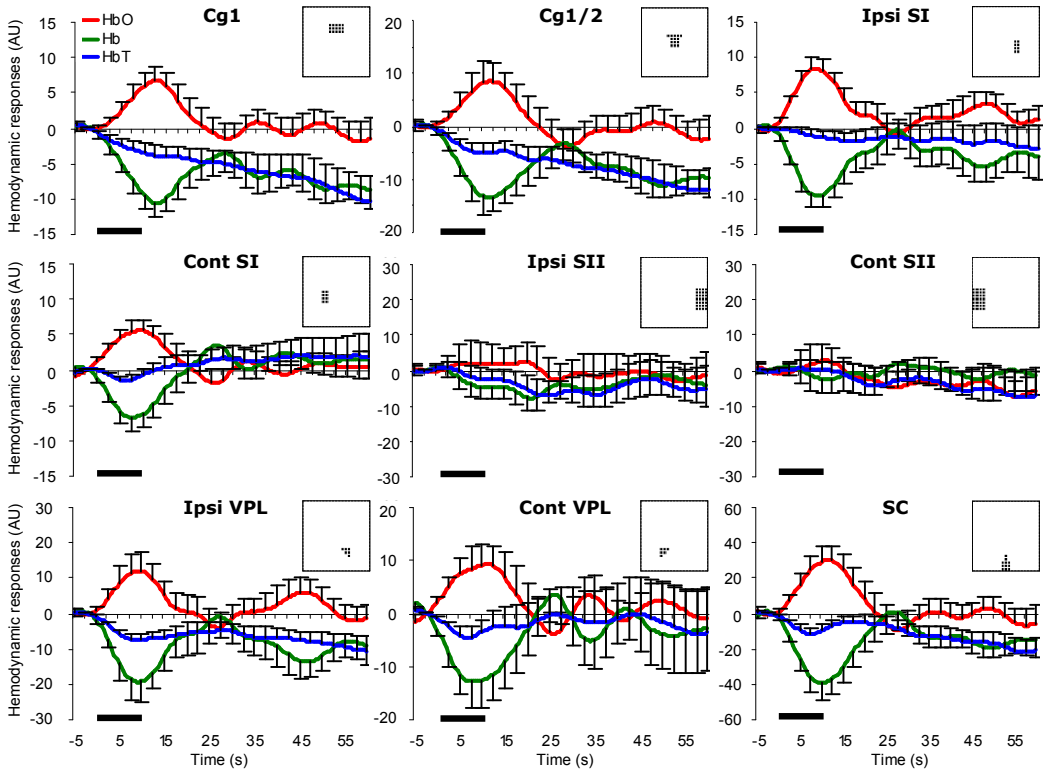


Figure 2.3 Time Serials of Hemodynamic Responses to Brush at Nine ROIs. An error bar is SEM. For an ease of visualization, it is shown every 2.5 s. The temporal resolution was 2 Hz. A bold line indicates 10 s brush. An inset in each subfigure describes the location of ROI.

Table 2.1 A Summary of [HbO], [Hb], and [HbT] Changes in Nine ROIs in Response to Brush (in arbitrary unit). Note: Max – maximal value between 0 and 20 s; Area – an integrated area between 0 and 30 s; I – ipsilateral; C – contralateral; *$p < 0.05$ ($n = 10$).
Numeric values are shown in a mean ± SEM.

| | HbO | | Hb | | HbT | |
|---|---|---|---|---|---|---|
| Region | Max | Area | Max | Area | Max | Area |
| Cg1 | 7 ± 3.1 * | 147.8 ± 70.3 * | -12.5 ± 2.2 * | -374 ± 73 * | -4.7 ± 1.7 * | -226.2 ± 81.2 * |
| Cg1/2 | 10.3 ± 5 * | 172.7 ± 123.4 | -17.8 ± 3 * | -475.8 ± 101.6 * | -7.8 ± 2.1 * | -303.3 ± 109.8 * |
| SI | 10.2 ± 1.3 (I) *<br>5.9 ± 2.6 (C) * | 212.3 ± 74.5 (I) *<br>126.1 ± 61.2 (C)* | -11.2 ± 2.2 (I) *<br>-6.3 ± 3 (C) * | -286.7 ± 84.2 (I) *<br>-114 ± 61.1 (C) * | -2.4 ± 1.5 (I)<br>-.4 ± 1.6 (C) | -74.6 ± 69.3 (I)<br>12.1 ± 59.4 (C) |
| SII | 4.5 ± 7.3 (I)<br>-.5 ± 5.9 (C) | 52.4 ± 259.6 (I)<br>-58.9 ± 190.2 (C) | -7.2 ± 5.1 (I)<br>-3.2 ± 6.5 (C) | -255.4 ± 167.4 (I)<br>-30.3 ± 232.8 (C) | -5.6 ± 4.3 (I)<br>-4.9 ± 5.5 (C) | -203 ± 156.6 (I)<br>-89.2 ± 178 (C) |
| VPL | 11.8 ± 6.9 (I)<br>12.2 ± 6.4 (C) * | 225 ± 199.8 (I)<br>215.4 ± 139.6(C) | -20.9 ± 6.6 (I) *<br>-17.3 ± 6.2 (C) * | -564.9 ± 237 (I) *<br>-349.9 ± 203.6 (C) | -10.3 ± 2.3 (I) *<br>-4.9 ± 4.6 (C) | -339.9 ± 103.6 (I) *<br>-134.8 ± 188.4 (C) |
| SC | 33.2 ± 12.7 * | 693.2 ± 318.7 * | -46.5 ± 10.2 * | -1125.6 ± 308.1 * | -12.1 ± 4.1 * | -432.4 ± 201.1 * |

*2.3.2 Pinch-Elicited Hemodynamics*

Compared to the baseline, an increase in [HbO] with a concomitant decrease in [Hb] was indicated only in the contralateral SII (Table 2.2), while a decrease in [HbT] was found in the Cg1 and contralateral SI. Lateralization was found in the SI (Max in [HbT]: $t(10) = 1.87$, $p = 0.045$) and SII (Area in [HbO]: $t(10) = -2.50$, $p = 0.016$). Furthermore, to find out if there were functional differences of hemodynamics between innocuous and noxious conditions, we only compared the ROIs showing significant changes for both brush and pinch. Comparisons between brush- and pinch-elicited hemodynamics failed to detect differences in the Cg1 (Max in [HbT]: $p = 0.22$; Area in [HbT]: $p = 0.12$) and contralateral SI (Max in [HbT]: $p = 0.25$; Area in [HbT]: $p = 0.21$).

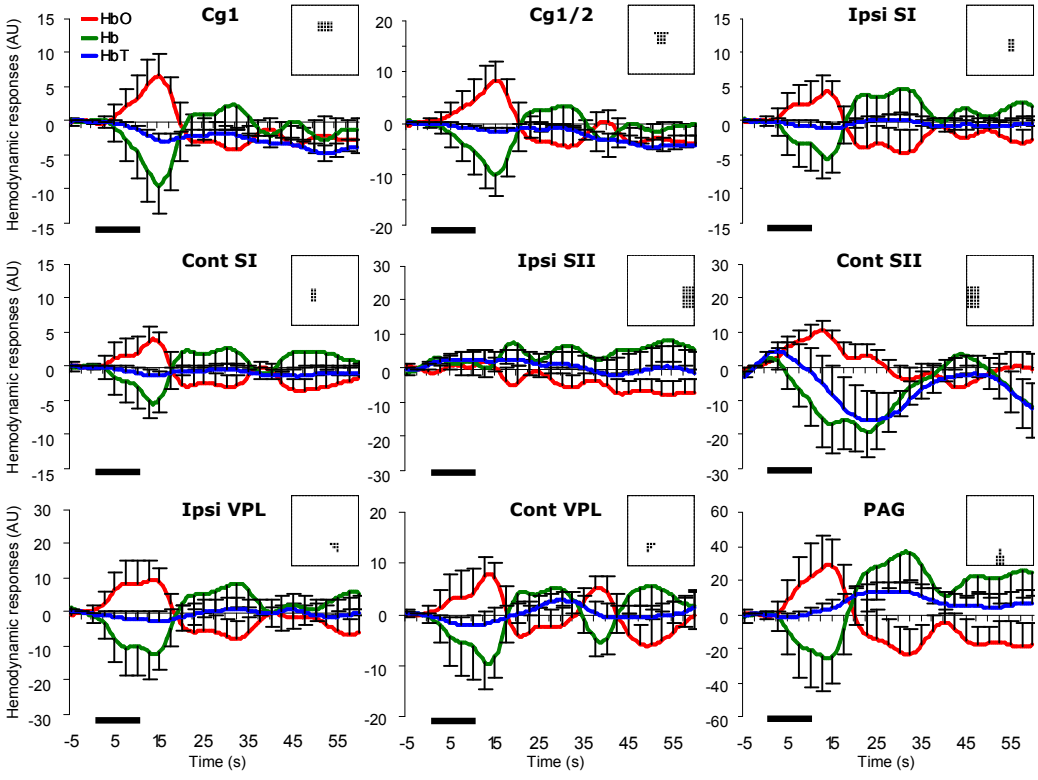


Figure 2.4 Time Serials of Hemodynamic Responses to Pinch at Nine ROIs. An error bar is SEM. For an ease of visualization, it is shown every 2.5 s. The temporal resolution was 2 Hz. A bold line indicates 10 s pinch. An inset in each subfigure describes the location of ROI.

Table 2.2 A Summary of [HbO], [Hb], and [HbT] Changes in Nine ROIs in Response to Pinch (in arbitrary unit). Note: Max – maximal value between 0 and 20 s; Area – an integrated area between 0 and 30 s; I – ipsilateral; C – contralateral; *$p < 0.05$ ($n = 11$). Numeric values are shown in a mean ± SEM.

| | HbO | | Hb | | HbT | |
|---|---|---|---|---|---|---|
| Region | Max | Area | Max | Area | Max | Area |
| Cg1 | 2.7 ± 4.5 | 51.3 ± 118.1 | -4.4 ± 5.4 | -138.5 ± 143 | -2.7 ± 1 * | -87 ± 33 * |
| Cg1/2 | 3.9 ± 5.3 | 88.3 ± 136.1 | -4.7 ± 5.8 | -144.1 ± 152.7 | -1.4 ± 1 | -55.6 ± 36.6 |
| SI | .7 ± 4.5 (I)<br>.7 ± 3.6 (C) | -5.7 ± 99.7 (I)<br>5.3 ± 79.8 (C) | -1.5 ± 5.2 (I)<br>-1.5 ± 4.3 (C) | -32.8 ± 124.6 (I)<br>-48 ± 105.8 (C) | -.8 ± .9 (I)<br>-1.6 ± .8 (C) * | -27.2 ± 35.7 (I)<br>-42.7 ± 34.2 (C) |
| SII | -.4 ± 5.8 (I)<br>7.3 ± 4.7 (C) | -45.3 ± 161.9 (I)<br>313.7 ± 146.2 (C) * | 4.6 ± 6.4 (I)<br>-17.5 ± 8.8 (C) * | 150 ± 203.1 (I)<br>-662.1 ± 318.3 (C) * | 2.7 ± 3.5 (I)<br>-7.2 ± 9.8 (C) | 104.7 ± 115.2 (I)<br>-348.3 ± 354.2 (C) |
| VPL | 9 ± 8.8 (I)<br>-4.3 ± 7.3 (C) | 136.2 ± 178.8 (I)<br>49.5 ± 175.7 (C) | -10 ± 11 (I)<br>-1.9 ± 8.4 (C) | -195.5 ± 268.7 (I)<br>-77.1 ± 185.8 (C) | -1.6 ± 3.4 (I)<br>-.7 ± 2.7 (C) | -59.3 ± 134.1 (I)<br>-27.7 ± 87.6 (C) |
| PAG | 13.9 ± 23.3 | 328.8 ± 646.3 | -10.6 ± 25.8 | -23.9 ± 686.8 | 7.5 ± 5.7 | 305 ± 190.4 |

A failure of detecting a significant change for pinch might be in part due to an inappropriateness of the time window. For instance, an increase in [HbT] tended to occur between 20 and 35 s in the PAG (bottom right in Figure 2.4). By using such window, a significant increase was confirmed (Max: 17.9 ± 5.6 AU, $t(10) = 3.18$, $p = 0.005$; Area: 360.6 ± 155.1 AU, $t(10) = 2.32$, $p = 0.02$). A temporal pattern of [HbT] change in response to pinch tended to be region-specific. However, for an error control purpose, we tried to avoid manually selecting multiple time windows for statistical analysis.

## 2.4 Discussion

Several brain regions, such as the ACC, SI, VPL, and SC, were activated in response to brush as shown by an increase in [HbO] and/or a decrease in [Hb]. It should be noted that two dependent variables (e.g. Max and Area) were used to assess a significant change in [HbO], [Hb], and [HbT]. The Max was designed to reveal a transient effect, whereas the Area to reveal an accumulated effect. Significant change in either variable should equally suggest a real effect. Activations of the aforementioned areas indicated an activities in somatosensory processing pathway, which were in accordance with other imaging studies in humans and animal models (Chen et al., 2002; Buchel et al., 2002; Bornhovd et al., 2002; Sutherland and Tang, 2006; Lowe et al., 2007; Blatow et al., 2007). Starting in the periphery, action potentials

are transmitted to the spinal cord by the primary afferents. The spinal cord further transmits the sensory signals to various supraspinal structures via spinothalamic, spinomesencephalic and other tracts. While the VPL dominantly receives sensory input from the spinothalamic tract (Dykes et al., 1988), the mesencephalic SC contains multi-sensory neurons that were believed to integrate various sensory modalities from the spinal cord (Abrahams et al., 1988; Wallace et al., 1996). The brush stimulus is perceived in the SI by receiving inputs from the VPL (Dykes, 1978). Meanwhile, as the mediodorsal and other subnuclei of thalamus delivers the signals to the prefrontal cortex (Rose and Woolsey, 1948; Berendse and Groenewegen, 1991; Groenewegen et al., 1997; Groenewegen, 2004), the ACC and other prefrontal regions are activated, which were believed to be responsible for attention and cognition (Peyron et al., 1999; Buchel et al., 2002; Bornhovd et al., 2002).

The contralateral SII was activated in response to pinch as shown by an increase in [HbO] and a decrease in [Hb]. A growing body of evidence indicated that the SII plays an important role in discriminating pain, and the magnitude of its activity was positively correlated to pain intensity (Peyron et al., 1999; Timmermann et al., 2001; Chen et al., 2002; Bornhovd et al., 2002; Maihofner and Kaltenhauser, 2009). Thus, our observations were in line with current understanding of pain and non-pain processing networks in the brain. However, we failed to find as many ROIs showing statistically significant hemodynamics for pinch as for brush.

*2.4.1 The Hemodynamic Signature of Brain Functioning: Linearity between [HbO] and [Hb] Changes*

Historically, an increase in [HbO] with a concomitant decrease in [Hb] was believed to be a typical hemodynamic signature of brain functioning (Villringer et al., 1993). FNIRI studies had provided converging evidence of activation in related cortices with visual (Seiyama et al., 2004; Schroeter et al., 2006), somatosensory stimulations (Seiyama et al., 2004; Becerra et al., 2008) and motor tasks (Huppert et al., 2006) stimuli in human. Our observations also showed such signature (Figure 3). However, a reversed pattern (i.e. a decrease in [HbO] coupled with

an increase in [Hb]) tended to occur in the PAG after 20 s in response to noxious pinch (Figure 4). A similar finding in a prefrontal area was reported in a human study with anagram tasks (Tian et al., 2009b). Another human study also failed to detect the conventional signature in the frontal area in response to a heat pain (Becerra et al., 2008). Therefore, the hemodynamic signature tends to be brain region- and task-dependent.

In order to investigate a hemodynamic signature of pain processing in rat brain, we used the regional [HbO] and [Hb] changes from all ROIs, because the temporal patterns at all ROIs (except for the SII) showed a high degree of resemblance for brush (Figure 2.3) and pinch (Figure 2.4), respectively. A frequency was utilized to assess how often a pair of regional [HbO] and [Hb] change (i.e. dyad) occurred in response to brush or pinch. Four kinds of such dyad were categorized into increases in both [HbO] and [Hb] (+HbO/+Hb, shown in quadrant 1 as Q1 in Figure 2.5A), an increase in [HbO] with a decrease in [Hb] (+HbO/-Hb, as Q2), decreases in both [HbO] and [Hb] (-HbO/-Hb, as Q3), and a decrease in [HbO] with an increase in [Hb] (-HbO/+Hb, as Q4). Five distinct time periods were used, including a 5 s-baseline (Figure 2.5A), an initial (0 – 20 s) and a late period (40 – 60 s) for brush (Figures 2.5B and 2.5C) and pinch stimuli (Figures 2.5D and 2.5E).

During the baseline and initial periods of brush and pinch, more than 80% of total dyads were either +HbO/-Hb (Q2) or –HbO/+Hb (Q4, see also Column 5 in Table 2.3). A significant linear relationship between [HbO] and [Hb] changes was suggested by the Pearson correlation coefficient and the slope (Column 6 and 7 in Table 2.3). Particularly, the negative slope indicated that [HbO] and [Hb] changes were constantly opposite to each other. Therefore, the negative linear relationship between [HbO] and [Hb] tended to be more representative for neurovascular signature of brain functioning.

During the late period of brush and pinch, there were more incidences of +HbO/+Hb (Q1) and –HbO/-Hb (Q3) in the brain (Table 2.3). This might be in part attributed to the vascular response to establish a new baseline. After a neurovascular perturbation (i.e. in response to

brush or pinch), the local vascular system will tend to return to the baseline status, where exchange of oxygen becomes less active, as reflected by reduction of dyads in Q2 and Q4. The regional [HbO] and [Hb] might be influenced by vascular change that is irrelevant to neuronal activity. When a vessel dilates, more HbO and Hb influx to this region which results in increases in local [HbO] and [Hb], and *vice versa*.

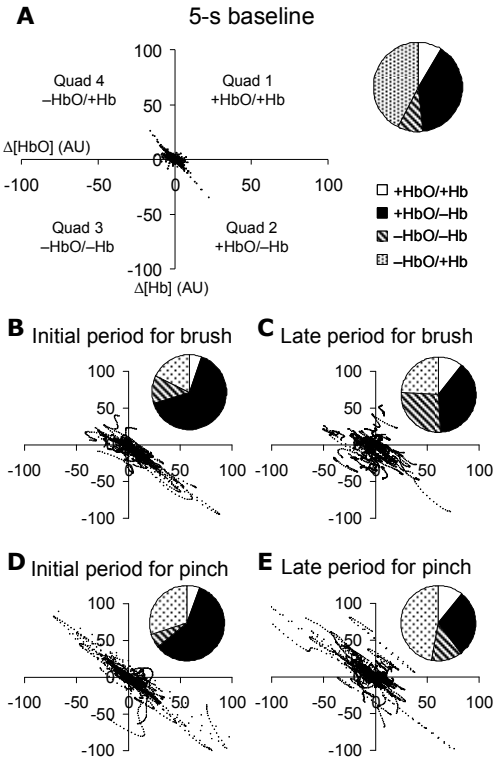


Figure 2.5 Distribution of The HbO-Hb-Dyads in 5 time Levels, Including A Baseline (-5 – -.5 s), Two Initial (0 – 30 s) and Late (40 – 60 s) Periods for Brush and Pinch. Each dyad indicates a pair of simultaneous [HbO] and [Hb] change within in a time level. All nine ROIs introduced in Results were used. A pie-chart demonstrates the percentages of 4 kinds of dyads in each time level. Note: Q1 - open area, Q2 - dark area, Q3 - hatched area, Q4 - dotted area.

Table 2.3 Distributions of The HbO-Hb Dyads and The Linear Relationship between [HbO] and [Hb] Changes. Columns 1 - 4 illustrate the percentages of 4 kinds of dyads in 5 time levels. Column 5 shows the percentage of a combination of the +HbO/-Hb and –HbO/+Hb dyads. Columns 6 and 7 describe a linear relationship in the Pearson correlation coefficient and the slope.

| | Quad 1 ΔHbO > 0 ΔHb > 0 | Quad 2 ΔHbO > 0 ΔHb < 0 | Quad 3 ΔHbO < 0 ΔHb < 0 | Quad 4 ΔHbO < 0 ΔHb > 0 | Quads 2&4 | Pearson Corr. | Slope (Mean ± SEM) |
|---|---|---|---|---|---|---|---|
| Baseline (-5 – -.5 s) | 8.6% | 39.7% | 9.23% | 42.43% | 82.1% | -.79 | -.91 ± .01 |
| Brush (0 – 20 s) | 5.2% | 65.2% | 12% | 17.7% | 82.9% | -.87 | -.91 ± .01 |
| Brush (40 – 60 s) | 10.7% | 38.5% | 26.7% | 24.1% | 62.6% | -.39 | -.46 ± .02 |
| Pinch (0 – 20 s) | 5.5% | 58.8% | 5.7% | 30% | 88.8% | -.91 | -1.04 ± .01 |
| Pinch (40 – 60 s) | 10.8% | 29% | 13.1% | 47.1% | 76.1% | -.75 | -.88 ± .01 |

It is worth mentioning that we failed to find a substantial linear relationship between [HbT] and either of two hemoglobin components (See Table 1 in Appendix B). In principle, since [HbT] is a linear function of [HbO] and [Hb], [HbT] should have strong linear relationship with either one. This unexpected result was most likely due to a weak signal-noise-ratio of [HbT] (See a mathematical proof in Appendix B).

*2.4.2 –HbO/+Hb Represents A Potential Hemodynamic Signature of Pain Processing*

Further analysis of four dyads indicated that pinch elicited significantly more -HbO/+Hb dyads (Q4) than brush during both the initial period (30% vs 17.7% of total dyads in Table 2.3, Figures 2.5B and 5D; chi-square test, $\chi^2(1) = 426.4$, $p < 0.0001$) and late period (47.1% vs 24.1% of total dyads in Table 2.3, Figures 2.5C and 5E; $\chi^2(1) = 1168.4$, $p < 0.0001$). Importantly, the +HbO/-Hb dyads (Q2) constantly outnumbered the –HbO/+Hb (Q4) during the initial period for brush (65.2% vs 17.7% of total dyads; $\chi^2(1) = 1006.9$, $p < 0.0001$) and pinch (58.8% vs 30% of total dyads; $\chi^2(1) = 378.3$, $p < 0.0001$), and such discrepancy hardly reached to a significant level during baseline (39.7% vs 42.43% of total dyads; $\chi^2(1) = 3.3$, $p > 0.05$). Thus, brain functioning in general appeared to show more +HbO/-Hb (Q2) than –HbO/+Hb (Q4) dyads in innocuous brush. However, in pain condition, –HbO/+Hb (Q4) tended to occur more saliently and frequently than in non-pain condition. The presence of –HbO/+Hb should account

for the failure of detecting as much statistically significant hemodynamic response to pinch as to brush over the brain.

The typical +HbO/-Hb is believed to be a hemodynamic signature of nerve functioning. The increase in [HbO] indicates a demand of oxygen while the decrease in [Hb] indicates a demand of removing the accumulated Hb during nerve activation. On the other hand, an atypical -HbO/+Hb was also reported in human brain during functional activation and hypothesized to be aging-related (Villringer et al., 1993). A recent age-matched study with young and elderly subjects failed to prove this hypothesis (Mehagnoul-Schipper et al., 2002). Our previous study indicated that the –HbO/+Hb was correlated to a formalin-induced long-lasting nociception in rat brain (See Chapter 1). It suggested that –HbO/+Hb was also a hemodynamic signature of nerve activation, and its occurrence tended to be brain status-dependent. When firing neurons constantly demand for more oxygen (e.g. the late phase of formalin injection), the vascular bed may encounter a ceiling effect of providing excessive HbO and removing Hb rapidly, which results in –HbO/+Hb. In an acute condition (pinch), when neurons fire intensively and briefly, the vascular bed may not satisfy the massive demand of oxygen supply and Hb removal, which also results in –HbO/+Hb.

# CHAPTER 3

# A VALIDATION OF THE FIBER OPTIC SYSTEM

## 3.1 Background

Inflammation is the typical reaction of the biological tissue to a harmful stimulus. It is characterized by four cardinal signs: Redness (rubor), warmth (calor), swelling (tumor), and pain (dolor), which were first described by Cornelius Celsus almost 2000 years ago. Redness and warmth are primarily due to an increase in blood influx and vasodilatation in the inflamed area, where oxygen and other nutrients are urgently and massively demanded by local neurons, immune cells, endothelial cells, mast cells, and vessels. Swelling is secondary to plasma extravasation from venules in response to a release of substance P (SP) at sensory neuron terminals (Lembeck and Holzer, 1979; Wallengren and Hakanson, 1987; Jacques et al., 1989). Pain is the subjective aspect of agitation of nociceptive sensory neurons in response to a harmful stimulus. Cells in the inflamed area interact profoundly via numerous chemical mechanisms (Steinhoff et al., 2003; Zegarska et al., 2006), which lead to a complicated biological process, called inflammation.

Optical technologies allow us to noninvasively and simultaneously measure regional concentrations of oxygenated ([HbO]) and deoxygenated hemoglobins ([Hb]), and the light scattering property of a tissue. On one hand, lights at 500 to 600 nm wavelengths are potently absorbed by hemoglobin in the red blood cells. Within this range, absorptions for the HbO and Hb are distinctive at various wavelengths, so that absolute [HbO] and [Hb] can be obtained (Nagashima et al., 2000). A total hemoglobin concentration ([HbT]) can also be calculated by adding [HbO] and [Hb] together, which indicates a regional blood volume. Furthermore, oxygen saturation rate (SO2; calculated by [HbO] / [HbT]) demonstrates an oxygenation level. On the other hand, lights over 700 nm wavelength are predominantly influenced by the scattering

property of a tissue where the lights travel through (Liu et al., 2008). In early studies, an increase in light scattering was observed during neuronal electrical charge in crab leg nerves and squid giant axons (Hill and Keynes, 1949; Cohen and Keynes, 1971; Cohen et al., 1972a; Cohen et al., 1972b). An optical imaging system named optical coherence tomography (OCT) had been developed to detect scattering changes in the retina (Huang et al., 1991; Yao et al., 2005; Srinivasan et al., 2006; Srinivasan et al., 2009), somatosensory cortex (Aguirre et al., 2006; Chen et al., 2009) and visual cortex (Maheswari et al., 2003; Rajagopalan and Tanifuji, 2007) during functional activations with high spatial and temporal resolutions. An even higher spatial-resolved imaging system, optical coherence microscopy, confirmed the scattering changes during evoked action potentials at a single neuron level (Graf et al., 2009). However, the origin of tissue scattering change is unclear and its functional significance needs further investigation.

Formalin is a well-known chemical to induce inflammatory pain (Hunskaar and Hole, 1987). Following injection, an increase in cutaneous blood flow was indicated by cutaneous blood velocity, skin temperature, and paw volume (Wheeler-Aceto and Cowan, 1991; Taylor et al., 2000; Fu et al., 2001). It is also demonstrated that noxious insult not only generates inflammatory responses ipsilaterally through local axonal reflexes (Lin et al., 1999), but also contralaterally through dorsal root reflexes (Peng et al., 2003). In the current study, we used a new analytical method to obtain absolute [HbO], [Hb], [HbT], SO2 and light scattering coefficient ($\mu_s$') noninvasively by using optical needle probe. The goal was to assess physiological significances of the aforementioned parameters in the formalin-induced inflammation. It was hypothesized that inflammatory response following formalin injection would cause changes of these hemodynamic parameters not only on the ipsilateral side, but also on the contralateral side. This was the first study to investigate the vascular oxygenation dynamic and concurrent light scattering changes simultaneously following formalin-induced inflammation.

## 3.2 Methods

*3.2.1. Animal Preparation*

Six Sprague-Dawley male rats were used with a mean age of 294.2 ± 0.9 days (± SEM) and a mean weight of 489.2 ± 7.4 g. All rats were initially anesthetized by sodium pentobarbital (50 mg/kg, intraperitoneal injection), and then immobilized in a stereotaxic frame. Anesthesia was maintained by a continuous intravenous (i.v.) administration of sodium pentobarbital (5 mg/ml; 0.02ml/min) during experiment. Animal was paralyzed by i.v. injection of pancuronium (1ml; 1ml/min) right before formalin injection to prevent any muscular twitches and reflexes during data acquisition. Artificial ventilation (Model 683, Harvard) was maintained throughout the experiment.

*3.2.2 Data Acquisition*

Two needle probes were placed above the right and left hind paws (i.e. one probe for each side). Each probe scanned a similar glabrous area close to the heel, ~10 mm away from the center of the hind paw (Figure 3.1), where formalin was injected. There were two reasons to select this region. First, the surface of the area was flat, and not wrinkled so that the probes tended to receive a consistent and maximal level of reflectance of light. Second, both published (Taylor et al., 2000) and our preliminary Doppler images indicated that a formalin-induced enhancement in cutaneous blood flow spread out over the entire paw, including our targeted area.

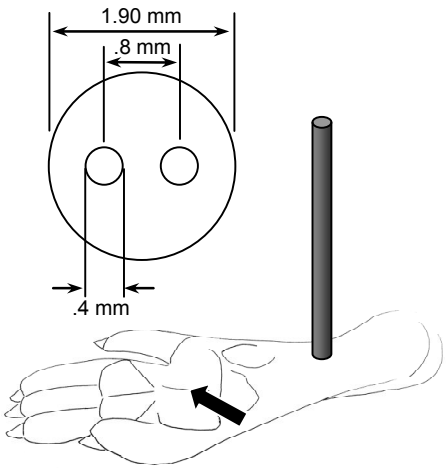


Figure 3.1 Specifications of The Needle-Like Optical Probe and An Illustration of Probe Placement. The black arrow indicates the injection site in rat hind paw.

Each probe was bifurcated. It contained a light source and a detector fiber. The physical separation of the source and detector embedded in a probe is 500 μm (Figure 3.1). Optical signal generated by a linear DC regulated source (3900 Smart-Lite, Illumination Technologies, US) was transmitted to one probe at a time. A multiplexer (Fiberoptic Multiplexer, Avantes, US) was used to switch the light-recipient probe back and forth at a fixed rate. Reflectance of light in the skin was collected by a detector in the light-recipient probe, and further converted into digital signal (with an integration time of 50 ms) by a spectrometer (S2000, Ocean Optics, US). A PC was connected to the spectrometer, and saved the spectrum continuously and automatically. The entire data acquisition system was controlled by LabView (National Instruments, Austin) codes under Windows operation system. The sampling rate was ~.6 Hz for each probe.

*3.2.3 Converting Optical Signals to Functional Signals*

After data collection was complete, the optical signals were converted into [HbO], [Hb], and $\mu_s'$ (at a selected wavelength) by using an iterative algorithm (Matlab compatible). This method was developed in Dr. Hanli Liu's lab at Bioengineering Department of the University of Texas at Arlington. In general, it tended to find a best set of solutions (e.g. [HbO], [Hb], and $\mu_s'$)

to fit a particular optical model which was designed to describe this short-source-detector-separation scenario. Accuracy of this optical model relies on two parameters, K1 and K2 (Zonios and Dimou, 2006), which were determined by a serial of horse-blood-phantom measures prior to our current study. Conversion of the entire optical signals (including all time points from two probes over all subjects) was accomplished by a UNIX high-performance-computing (HPC) system.

*3.2.4 Determine The Probe-Skin-Distance Effect on Optical Signals*

Photon propagation length is an important factor. The longer the photons travel, the less photon density is along the direction of photon propagation. It is necessary to evaluate the influence of a distance between probe and the skin surface (probe-skin-distance) on our measurement, because swelling following formalin injection might potentially affect the optical signal reading. A microdrive controller (6000ULN, Burleigh) was used to position the optical probes at 18 distances as of -50, -20, -10, 0, 10, 20, 50, 100-1000 (with a step of 100), and 1500 μm above the skin surface. A negative distance indicated a dent. A surgical microscope (Zeiss) was able to provide an "ideal contact" between probe and the skin without a dent (i.e. 0-distance). Measurements were performed on rat hind paws in a resting status without any external stimulus.

Twelve groups of such optical measures were obtained from both paws of six rats. At 0-distance, [HbO] = 21.52 ± 2.45 μM; [Hb] = 12.15 ± 1.30 μM; SO2 = .64 ± .02; $\mu_s'$ = 15.91 ± .78 $cm^{-1}$. A univariate within-subject one-way ANOVA indicated significant effects of the distance on [HbO], [Hb], SO2 and $\mu_s'$ in percentage change (Table 3.1). *Post hoc* analysis in multiple comparisons with Bonferroni correction (Figure 3.2) and contrast analysis (Table 3.1) revealed a salient linear component of such effects. That is, the greater a distance was, the stronger an effect appeared; an effect was predicted reliably by a linear equation as a function of the distance. Particularly, as the probe was moved above the skin, [HbO], [Hb], and SO2 tended to be suppressed, whereas $\mu_s'$ be inflated (Figure 3.2). [HbT] (i.e. [HbO] + [Hb]) was not shown

purposely, because that it should follow the same trend as [HbO] and [Hb]. There was also a noticeable but slight (i.e. less than 10% of measure at 0-distance) quadratic component of the distance-induced effects (Table 3.1) below distances of 200 μm (Figure 3.2).

Table 3.1 Statistics of The Distance-Induced Effects on [HbO], [Hb], SO2 and $\mu_s$' in Percent Change ($n$ = 12). A one-way within-subject ANOVA was utilized to assess a main effect of the distance and a contrast test to assess the linear and quadratic components of such effect. *Note:* * $p$ < .05.

| Parameter (percent) | Main effect | Contrast (linear) | Contrast (quadratic) |
|---|---|---|---|
| [HbO] | $p$ < .001 (*) | $p$ < .001 (*) | $p$ = .054 |
| [Hb] | $p$ < .001 (*) | $p$ < .001 (*) | $p$ = .077 |
| SO2 | $p$ < .001 (*) | $p$ < .001 (*) | $p$ = .046 (*) |
| $\mu_s$' | $p$ < .001 (*) | $p$ < .001 (*) | $p$ < .001 (*) |

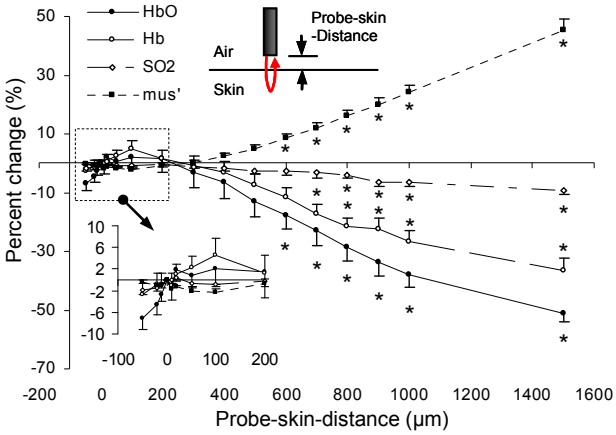


Figure 3.2 Percent Changes in [HbO], [Hb], SO2 and $\mu_s$' for 18 Levels Probe-Skin-Distance ($n$ = 12). The distances (on $x$-axis) were -50, -20, -10, 0, 10, 20, 50, 100-1000, and 1500 μm, as depicted by the top inset. The bottom left inset illustrates the distance-induced effect between -50 and 200 μm distances. A baseline measure was at 0-distance. *Note:* * $p$ < .05.

### *3.2.5 Formalin Injection*

Formalin (50 μl; 3%) was injected into the plantar area of rat hind paw unilaterally. The injection site was in center of the plantar area (pointed by a black arrow in Figure 1). A basal

level of optical signals in the hind paw was acquired for 1-2 min, and an additional 1-hour recording was obtained post injection.

Swelling in the hind paw was observed within 5 min post formalin injection as examined by measuring the paw thickness (Wheeler-Aceto and Cowan, 1991). A dent in the skin, to some extent, will cause redistributions of the cutaneous structures. It appears that a dent in the skin reduced the [HbO] at distances of -50 and -20 μm (Figure 3.2). With this regard, the optical probe was positioned at a fixed height of 400-600 μm above the ipsilateral hind paw prior to injection in order to prevent too much dent due to swelling.

*3.2.6 Data Analysis*

It should be noted that the raw value and percent change profiles equally reflect a formalin-induced effect. Any discrepancy between the two should be related to a hypothesis: whether the amount of change is dependent on a basal level. If it is not, the raw value is more representative than the percent change, and vice versa. For a better demonstration, we provided both formats for all functional parameters.

Since that a probe-skin-distance was introduced during baseline measure, and such distance influenced all functional parameters (See section 3.2.4), their basal values needed to be corrected. The percent change at a certain distance obtained in section 3.2.3 was used to counterbalance the distance-effect for each individual rat. A 5-min-average strategy was used for statistical analysis over time which resulted in 11 levels over a 5-min baseline and a 50 min post-injection period. A univariate within-subject two-way ANOVA was utilized to assess changes in two paws. Side of the hind paws and time were two independent variables. Post hoc analysis was performed with Bonferroni error correction followed by ANOVA if applicable. Alpha = .05. All statistical analyses were performed by SPSS Statistics17.0 (SPSS Inc.). All numeric measures were presented in mean ± standard error of the mean (SEM) unless specifically noted.

## 3.3 Results

**[HbO].** A significant change in the ipsilateral, but not the contralateral hind paw post injection was indicated by a two-way ANOVA and the follow-up simple effect tests (Table 3.2). Specifically, *post hoc* multiple comparisons between two sides at all time levels showed a long-lasting increase in raw value and percent change (noted by † in Figures 3.3A-B). *Post hoc* comparisons between baseline and all the other time levels in the ipsilateral side indicated a significant increase only in percent change (noted by * in Figure 3.3B). A maximal increase over 50 min in the ipsilateral side was 21.13 ± 4.80 μM (123.62 ± 28.40% of basal level). Due to the fact that a maximal change for an individual rat tended to occur at different time post injection, values of such maximal increase might not be necessarily matched to Figures 3.3A-B.

**[Hb].** ANOVAs failed to indicate a significant change in response to formalin injection (Table 3.2). Temporal profiles of two paws in raw value and percent change are shown in Figures 3C-D. However, by further grouping, four rats tended to show an increase (Max: 11.83 ± 5.66 μM; 108.16 ± 37.45% of basal level), and two a decrease (Min: -4.31 ± .28 μM; -39.92 ± 6.61% of basal level) post injection in the ipsilateral side. In other words, the formalin-induced [Hb] dynamics demonstrated a subject-specific pattern.

Table 3.2 Statistics of The Formalin-Induced Effects on [HbO], [Hb], [HbT], SO2 and $\mu_s$' in Raw Value and Percent Change ($n$ = 6). A two-way within-subject ANOVA was utilized to assess a formalin-induced response in the ipsilateral paw by using an interaction between side (ipsi- and contralateral) and time (11 levels). Simple effects on both sides of the paw were performed if applicable. *Note:* * $p$ < .05.

| | Raw | | | Per cent | | |
|---|---|---|---|---|---|---|
| Parameter | Side X Time Interaction | Simple Effect (contra) | Simple Effect (ipsi) | Side X Time Interaction | Simple Effect (contra) | Simple Effect (ipsi) |
| [HbO] | $p$ < .001 (*) | $p$ = .15 | $p$ < .001 (*) | $p$ < .001 (*) | $p$ = .29 | $p$ < .001 (*) |
| [Hb] | $p$ = .119 | - | - | $p$ = .144 | - | - |
| [HbT] | $p$ = .001 (*) | $p$ = .31 | $p$ = .002 (*) | $p$ < .001 (*) | $p$ = .28 | $p$ = .001 (*) |
| SO2 | $p$ < .001 (*) | $p$ = .56 | $p$ = .009 (*) | $p$ < .001 (*) | $p$ = .56 | $p$ = .007 (*) |
| $\mu_s$' | $p$ = .241 | - | - | $p$ = .239 | - | - |

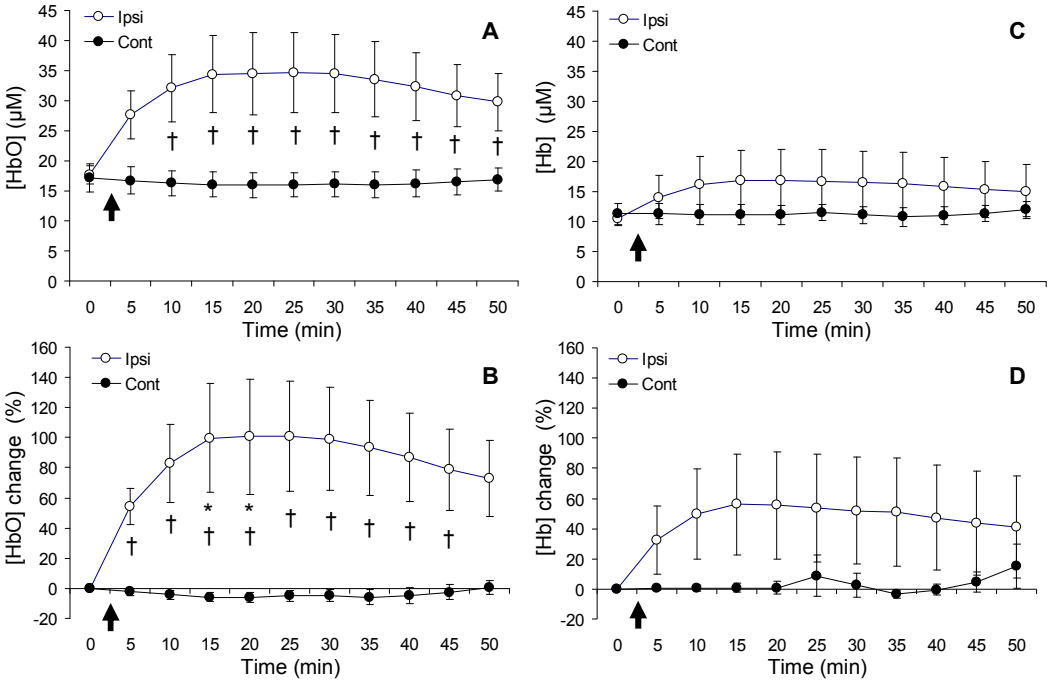


Figure 3.3 Bilateral [HbO] and [Hb] Responses in Hind Paws Post Formalin Injection (*n* = 6). [HbO] response is shown in raw value (**A**) and percent change (**B**); [Hb] response in raw value (**C**) and percent change (**D**). The black arrows indicate the injection time.
Note: * $p < .05$ against baseline; † $p < .05$ between two sides;
open circle: ipsilateral; and closed circle: contralateral.

**[HbT].** Similar to [HbO], statistics indicated a significant change only in the ipsilateral hind paw post injection (Table 3.2). *Post hoc* multiple comparisons between two sides showed a long-lasting increase in raw value and percent change (Figures 3.4A-B). A maximal increase in the ipsilateral side was 28.85 ± 8.82 μM (104.17 ± 26.76% of basal level).

**SO2.** Similar to [HbO] and [HbT], a significant change only in the ipsilateral hind paw was suggested (Table 3.2). *Post hoc* analysis between two sides indicated an increase post injection (Figures 3.4C-D). The maximal change was .08 ± .03 (13.44 ± 4.75% of basal level).

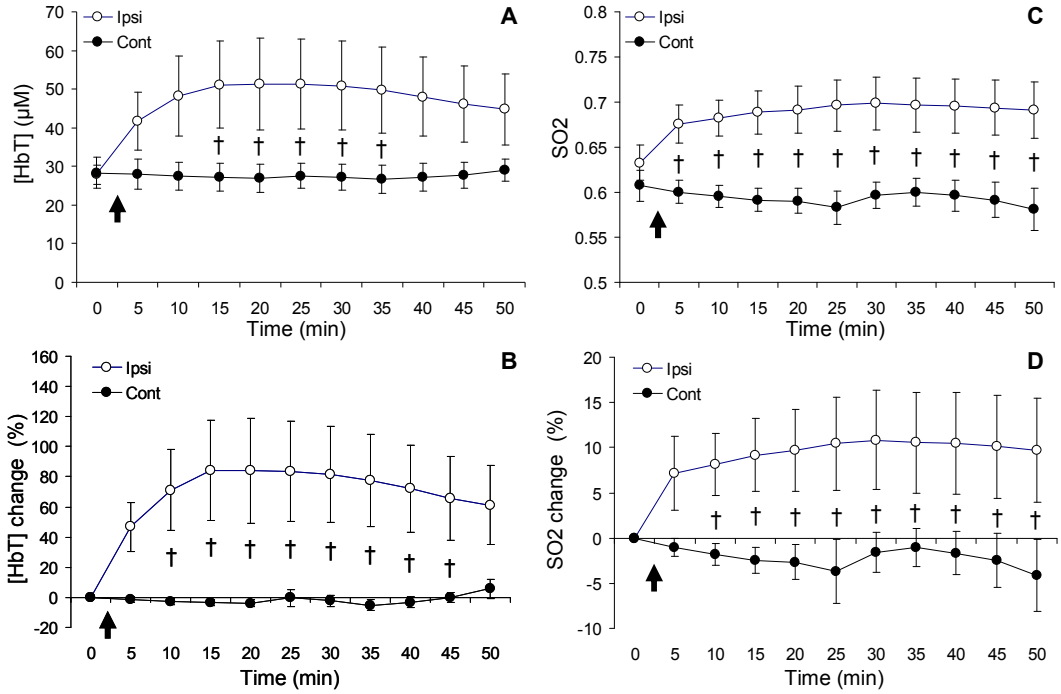


Figure 3.4 Bilateral [HbT] and SO2 Responses in Hind Paws Post Formalin Injection ($n$ = 6). [HbT] response is shown in raw value (**A**) and percent change (**B**); SO2 response in raw value (**C**) and percent change (**D**). The black arrows indicate the injection time. *Note:* * $p < .05$ against baseline; open circle: ipsilateral; and closed circle: contralateral.

***$\mu_s$'.*** We failed to detect a significant change over time (Table 3.2, Figures 3.5A-B). No consistent pattern of change could be found among all subjects in response to formalin injection.

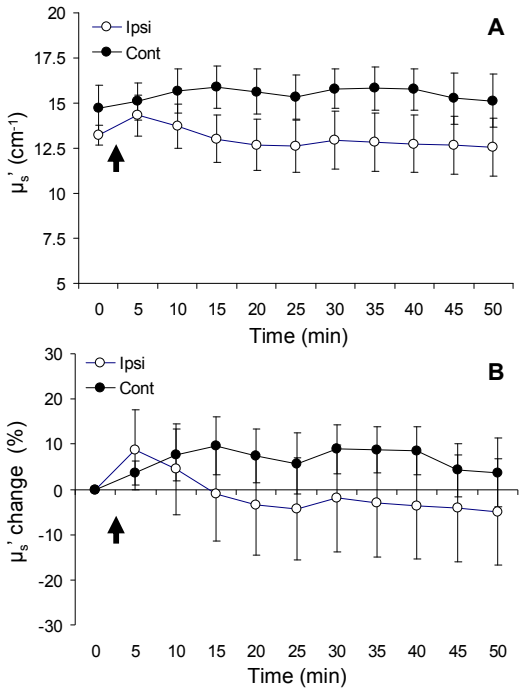


Figure 3.5 Bilateral $\mu_s$' Response in Hind Paws Post Formalin Injection in Raw Value (**A**) and Percent Change (**B**) (*n* = 6). *Note:* open circle: ipsilateral; and closed circle: contralateral.

## 3. 4 Discussion

It is unsurprising that there were increases in cutaneous [HbT] and SO2 post formalin injection. An inflammation-induced increase in cutaneous blood perfusion examined by Doppler flowmetry was reported by other studies (Taylor et al., 2000; Lin et al., 2003; Van der Schueren et al., 2008). An increase in cutaneous SO2 was also reported by a study measuring inflamed human skin (Newton et al., 1996). However, it is interesting that our data suggested the [HbO], but not the [Hb], being the major attribute of this elevation. The response in [Hb] post injection was subject-specific. Finally, we failed to observe any inflammation-induced scattering change in the skin near injection side.

### *3.4.1 SO2 in The Cutaneous Vascular Bed*

SO2 is a ratio of [HbO] to [HbT], ranging between 0 and 1. It is a measure of tissue metabolic level. An increase in SO2 means more oxygen molecules contained in tissue, and, in turn, indicates a greater metabolism. In blood circulation system, arterial SO2 is always greater

than venous SO2. The normal range of arterial SO2 is from .95 to .97 (Keys and Snell, 1937), whereas venous SO2 spans over a much broader range from .3 to .9 (Keys, 1938). Arterial SO2 represents a supply of oxygen, while venous SO2 describes a need and consumption of oxygen (Bloos and Reinhart, 2005). A normal value of venous SO2 varies from region to region and from time to time, because that tissue's demand for oxygen is dependent on its functionality and state (Bloos and Reinhart, 2005).

There are two distinct methods to measure blood SO2: Oxygen tension and optical methods. Oxygen tension (in mm Hg) is a direct measure of oxygen concentration in blood sample (including the oxygen bound to hemoglobins and the one dissolved in the plasma) by using oxygen electrode and a properly selected reagent (Severinghaus et al., 1998). SO2, then, can be calculated with a given oxygen dissociation curve (ODC) as a function of oxygen tension (Severinghaus et al., 1979). It is noteworthy that the ODC for normal adults is also a function of temperature, pH, CO2 tension (pCO2), and 2,3 diphosphoglycreate (Siggaard-Andersen and Siggaard-Andersen, 1995; Siggaard-Andersen and Gothgen, 1995; Hamilton et al., 2004; Clerbaux et al., 2006). Therefore, the arterial ODC is always different from the venous ODC (Shiao and Ou, 2007). The accuracy of obtaining a venous SO2 by using oxygen tension is, therefore, dependent on quality of the ODC. On the other hand, optical methods obtain an SO2 by directly measuring oxy- and other types of hemoglobin (e.g. deoxyhemoglobin, CO-hemoglobin, methemoglobin, NO-hemoglobin etc) concentrations. Optical-related measures of SO2 can be obtained invasively (by using blood sample or placing the optical probe in blood vessels) or noninvasively (by placing the optical probes on the skin).

Our measures of basal cutaneous SO2 in rat hind paw (.64 ± .02) were in accordance with the reports from other groups. Our noninvasive method indeed provided reliable measures of cutaneous SO2. In the cutaneous vascular bed, there are three different vascular structures, namely arteriole, capillary, and venule. A basal level of skin SO2 is determined by these physical structures (Lima and Bakker, 2005). According to the studies by using various

techniques, in normal adults, cutaneous SO2 at the finger tip, big toe and ear is close to arterial SO2 (~.9) (Lundsgaard and Moller, 1922; Lilienthal and Riley, 1944; Caspary et al., 1995; Thum et al., 1997; Bernet-Buettiker et al., 2005; Zavorsky et al., 2007). Cutaneous SO2 at the forehead, volar forearm, back of hand, forefoot, abdomen, and calf ranges from .4 to .8 (Detry et al., 1972; Harrison et al., 1992; Caspary et al., 1995; Newton et al., 1996; Yoxall and Weindling, 1997; Thum et al., 1997; Nagashima et al., 2000; Wolf et al., 2003; Ogrin et al., 2005), which is close to venous SO2.

Anesthetics have substantial microcirculatory actions (BAEZ and ORKIN, 1963; Longnecker and Harris, 1980). This action was shown to be type- and dose-dependent (Lovell et al., 1999; Hou et al., 2003). In general, isoflorane tends to increase SO2 (Hou et al., 2003; Abramovic et al., 2007); ketamine-xylasine tends to decrease it (Lei et al., 2001; Abramovic et al., 2007; Schlosser et al., 2009); barbiturates show both effects (Chen et al., 2008). A recent study using photoacoustic tomography imaging technology differentiated arteriola and venula in the back skin of the rat, and suggested that cutaneous venous SO2 was ~.5 whereas arterial SO2 was ~.75 under general anesthesia with ketamine-xylasine (Sivaramakrishnan et al., 2007). Considering the suppressive effect of ketamine-xylasine on SO2, such measures in rats were similar to those in human. Therefore, our results were in a normal range of SO2.

*3.4.2 Absolute Values of [HbO], [Hb] and [HbT] in The Skin*

Absolute values of regional [HbO], [Hb], and [HbT] are not easy to get. Optical signals which diffuse into tissue are often influenced by various factors, such as vascular structures, and photon travel distance. A classical model, e.g. Beer-Lambert equation, cannot appropriately describe such a heterogeneous medium, e.g. the cutaneous vascular bed and the nerve tissue. A perspective to overcome this is to modify the optical models. According to an *in vivo* study measuring absolute [HbT] in rodent parietal cortex by using a near infrared technology with an improved analytical model, a mean [HbT] of 6.1 ± 1.7 mg/ml (± SD) or 94.6 ± 26.4 μM, was found (Plesnila et al., 2002).

Alternatively, absolute values of regional [HbO], [Hb], and [HbT] can be obtained indirectly by using mathematical models with some given parameters that indicate vascular properties. With the properly estimated cerebral blood volume (Hamberg et al., 1996), cerebral tissue density (Sabatini et al., 1991), oxygen partial pressure (Hudetz, 1999), and cerebral large vessel density (Wyatt et al., 1990), cerebral [HbT] can be calculated (Zheng et al., 2005). A value of 75 μM is considered to be an averaged basal [HbT] over the brain (Zheng et al., 2005). This estimate was close to the optical-related measure mentioned earlier.

According to our data, a mean basal [HbT] in rat hind paw skin was 33.67 ± 3.54 μM, and a maximal [HbT] in the ipsilateral hind paw post injection was 56.77 ± 9.99 μM. Since the capillary density is ~300 per $mm^2$ in rat brain (Klein et al., 1986; Gobel et al., 1990; Zoccoli et al., 2000), and ~30 per $mm^2$ in rat and human skin (Lamah et al., 1996; Rendell et al., 1999; Lamah et al., 2000), the brain tissue should contain more blood than the skin does. However, a quantitative comparison of [HbT] between the brain and skin requires additional vascular parameters, such as blood pressure, arteriole, and venule densities. Nevertheless, our measured absolute [HbT] in rat skin should be in a physiological range.

*3.4.3 Light Scattering Changes Under Inflammatory Condition Remain Further Investigation*

We failed to detect any statistically significant change in $\mu_s'$ associated with the formalin-induced inflammation (Figure 3.5). Several factors might account for this. First, despite an increase in light scattering during nerve activation (Liu et al., 2008; Graf et al., 2009), density of nerve fibers in the skin beneath the optical probe should be a critical factor of detecting the nerve-induced light scattering change. The failure of seeing any significant change might be due to a low density of sensory fibers in the measured area. It might also suggest that light scattering change could be specific to neural tissue. Second, an inflammation is associated with plasma extravasation which is responsible for swelling and edema. OCT studies showed an increased thickness of epidermis associated with inflammation and it was accompanied by a decrease in light scattering (Welzel et al., 2003; Gambichler et al., 2005). A possible

mechanism was postulated elsewhere that (1) inflammation caused structural changes in the skin; and (2) density of the collagen, a natural protein widely distributed in the skin with a potent light scattering effect (LaCroix and Haidekker, 2009; Koopmans et al., 2009), was reduced as an accumulation of plasma in the interstitial area (Welzel et al., 2003). Finally, as there were a nerve-induced increase and a collagen-induced decrease in light scattering, two effects might cancel out each other, resulting in our failure of detecting a scattering change post formalin injection.

*3.4.4 Hemodynamic Change in The Contralateral Paw*

Although some evidence has shown that dorsal root reflexes can be recorded on the contralateral side (Bagust et al., 1989; Peng et al., 2003), we failed to prove our original hypothesis that dorsal root reflexes might contribute to the neurogenic inflammation on the contralateral side. Bilateral blood perfusion increase (as detected by laser Doppler imager) has been reported (Blumberg and Wallin, 1987; Kurvers et al., 1996), and observed in our lab following electrical stimulation of dorsal root, capsaicin- or formalin-injection (unpublished data). The failure to observe contralateral hemodynamic change could attribute to sensitivity of the optical needle probe technology.

## 3.5 Conclusion

Our noninvasive optical method provided reliable absolute measures of [HbO], [Hb], [HbT], SO2, and $\mu_s'$ in the skin in response to formalin-induced inflammation. The pattern of hemodynamic change in the skin could be used to further study the response in the brain.

# CHAPTER 4

# FOCAL HEMODYNAMIC AND LIGHT SCATTERING CHANGES DURING NOCICEPTION

## 4.1 Background

A relationship between nerve and its neighboring vascular structures (e.g. arteriole, capillary, and venule) during functional activation is referred to as neurovascular coupling. Relying on this phenomenon, modern neuroimaging technologies, such as laser Doppler imager (LDI), positron emission tomography (PET) and functional magnetic resonance imager (fMRI), are used to measure regional cerebral blood flow (CBF), blood volume (CBV) and blood-oxygen-level-dependent (BOLD) signal to estimate local metabolism and in turn, infer neuronal activation. However, there is some degree of uncoupling between aforementioned vascular-related measures and local metabolism. In a human subject PET study, the somatosensory stimulation induced an increase in CBF (29%) that remarkably surpassed the local metabolic enhancement (5%) (Fox and Raichle, 1986). A succeeding study suggested that tissue metabolism could be maintained without an increase in CBF (Mintun et al., 2001). A LDI study in rats indicated that CBV in the contralateral somatosensory cortex remained steady during forepaw stimulation (Detre et al., 1998). Despite that a positive BOLD signal was tightly correlated to neuronal electrical activities (Logothetis et al., 2001; Goense and Logothetis, 2008), the physiological significance of a negative BOLD was paradoxical. Both inhibition (Shmuel et al., 2006; Pasley et al., 2007) and excitation (Schridde et al., 2008) of neuronal activities were concomitant with a negative BOLD. Thus, the preciseness of interpreting neurovascular coupling-based imaging data requires a careful characterization of vascular dynamic and a more reliable measure of local metabolism.

Optical method is able to measure regional oxy- ([HbO]) and deoxyhemoglobin concentrations ([Hb]) respectively at a high sampling rate. It provides a direct measure of local oxygen dynamic. An increase in [HbO] coupled with a decrease in [Hb] was believed to be a hemodynamic signature of nerve functioning as examined by functional near infrared imager (fNIRI) in humans during somatic sensory, visual, and motor stimulation (Mehagnoul-Schipper et al., 2002; Huppert et al., 2006; Sakatani et al., 2007). However, the hemodynamic patterns during pain processing (Becerra et al., 2008) and cognitive task (Tian et al., 2009b) tended to be more complex. Furthermore, light scattering describes an effect that photons are dispersed when diffuse into biological tissues. A light scattering alternation was associated with nerve activation as examined by many techniques in various species, from the crab leg nerves to squid giant axons (Hill and Keynes, 1949; Cohen et al., 1972a), and from the retina, somatosensory to visual cortices in cats and rats (Huang et al., 1991; Maheswari et al., 2003; Srinivasan et al., 2006; Aguirre et al., 2006; Rajagopalan and Tanifuji, 2007). This finding suggested a possibility of simultaneously measuring hemodynamics and neuronal activation at a focal area by using optical methods.

A fiber optic system was newly developed to obtain absolute measures of [HbO], [Hb], blood volume ([HbT], calculated by [HbO] + [Hb]), oxygen saturation rate (SO2, calculated by [HbO] / [HbT]), and light scattering coefficient ($\mu_s$') by using reflectance of light from a focal area (Chapter 3). In this present work, we sought to discover biomarkers of pain by investigating temporal and regional characteristics of hemodynamic parameters (e.g. [HbO], [Hb], [HbT], and SO2) and $\mu_s$' alternation in rat primary somatosensory cortex (SI) and spinal cord in pain processing, induced by both brief and long-lasting modalities, including mechanical, electrical and chemical stimuli.

## 4.2 Methods

### *4.2.1 Animal Preparation*

Ten male Sprague-Dawley rats were recruited, with a mean age of 102.1 ± .6 (± SEM) days and a mean weight of 377.9 ± 14.5 g. All animals were initially anesthetized by intraperitoneal injection of pentobarbital sodium solution (50 mg/kg). A PE10 tubing was inserted into the jugular vein for continuous intravenous administration of pentobarbital sodium (5 mg/ml) at a fixed rate of 0.02 ml/min to maintain anesthesia during data acquisition (Peng et al., 1996a). The lumbasacral segment of rat spinal cord was exposed following laminectomy and then animal was immobilized on a stereotaxic frame. The dura mater was removed, and a pool of mineral oil was formed over the spinal cord to preserve moisture. Rat body temperature was maintained at 37°C by a feedback controlled heating blanket (Homoeothermic Blanket, Harvard). Animal was further paralyzed by i.v. injection of pancuronium (1ml; 1ml/min) to prevent any muscular twitches and reflexes. Artificial ventilation (Model 683, Harvard) was maintained throughout the experiment. All procedures were approved by the Institutional Animal Care and Use Committee (IACUC) at the University of Texas at Arlington. Procedures also followed the guidelines described by the Committee for Research and Ethical Issues of IASP (Zimmermann, 1983).

### *4.2.2 Instrumentation*

A home-made optical system was used to collect reflectance of light at wavelengths between 400 and 1000 nm by a needle-like fiber optic placed above the spinal cord or primary somatosensory cortex (SI). The scheme of the system was introduced in great details in our previous work (See Chapter 3). Four needle-like fiber optics (.85 mm in diameter) were positioned at the dorsal surface of the dorsal root entry zones at the lumbar segment and SI for the hind limb (at posterior Bregma .8 mm and 2 mm lateral) bilaterally. The size of scanned area is restricted by the physical size of fiber optics and the separation between a source and detector tubes embedded in the fiber (100 μm). Prior to the optic placement on the spinal cord,

a silver ball-electrode was used to locate the ipsilateral dorsal root entry zone which received a maximal primary afferent input during gentle tapping of rat hind paw. Two holes above the bilateral SI areas were made following craniotomy, and were filled with few drops of mineral oil before the optic placement to avoid any air gap. A surgical microscope (Zeiss) was used to ensure that the optic tip contacted the SI or spinal cord without dent. To investigate the microcirculation system during functional activation, we purposely avoided large vessels when placing optic. After the experiment, optical signals were converted into [HbO], [Hb], and $\mu_s'$ by using an iterative algorithm in Matlab (MathWorks, US). The conversion procedures were introduced in our previous work (See Chapter 3).

*4.2.3 Mechanical, Electrical and Chemical Stimuli*

Graded 10 s mechanical (e.g. brush, pressure and pinch) and electrical (e.g. 5-, 10-, and 15-V) stimuli at 10 Hz and 1 ms pulse-duration (Grass S48 stimulator, US), were applied to rat hind limb unilaterally. Mechanical stimuli were applied on the plantar surface (Peng et al., 1996b; Ativanichayaphong et al., 2008). Electrical stimuli were delivered to the ankle by connecting two leads (i.e. bent syringe needles) penetrated into the skin. Both mechanical and electrical stimulations were conducted in a block design with five trials and an interval of 2 min on the same paw for each animal. After mechanical and electrical stimulation, formalin (50 µl; 3%) was injected into the central plantar area of the other paw.

*4.2.4 Statistical Analysis*

A directional one-sample t test was utilized to assess any significant changes in all physiological parameters, e.g. [HbO], [Hb], [HbT], SO2, and $\mu_s'$. A univariate one-way within-subject ANOVA was utilized to assess formalin-induced parameter changes over time. Contrast analysis and *post hoc* Fisher LSD multiple comparisons were used to reveal the temporal pattern of a signal change if necessary. Alpha level was set at 0.05. All data were expressed in mean ± standard error of the mean (SEM). All statistical analyses were performed in SPSS 17.0 (SPSS Inc. US).

## 4.3 Results

### *4.3.1 Basal Levels of Hemodynamic Parameters and Light Scattering Coefficient*

Table 4.1 illustrates baseline measures of [HbO], [Hb], SO2, [HbT], and $\mu_s'$ before the first stimulation (i.e. brush) from four locations ($n$ = 10). There were considerable subject-related variations for [HbO], [Hb], and [HbT] as shown by SEM. The mean SO2 ranged from .4 to .7 over the SI and spinal cord. A significant difference between the SI and spinal cord was found in $\mu_s'$ (Contralateral: $t(9) = 8.88$, $p < 0.001$; Ipsilateral: $t(9) = 3.18$, $p < 0.01$), indicating that the light scattering effect in the SI tended to be weaker than that in the spinal cord.

Table 4.1 Absolute values of hemodynamic parameters and light scattering in baseline from bilateral spinal cord and SI ($n$ = 10).

| | **SI** | | **Spinal Cord** | |
|---|---|---|---|---|
| | **Contralateral** | **Ipsilateral** | **Ipsilateral** | **Contralateral** |
| **[HbO]** (μM) | 71.8 ± 15.6 | 112.1 ± 21.7 | 31.1 ± 18.7 | 14.5 ± 4.5 |
| **[Hb]** (μM) | 68.1 ± 18.9 | 46.7 ± 16.7 | 50.5 ± 28.7 | 18.8 ± 7.9 |
| **SO2** | .51 ± .07 | .70 ± .08 | .40 ± .07 | .52 ± .07 |
| **[HbT]** (μM) | 140.0 ± 30.7 | 160.1 ± 24.7 | 81.3 ± 47.0 | 33.4 ± 11.0 |
| $\mu_s'$ ($cm^{-1}$) | 11.5 ± .6 | 13.5 ± 2.9 | 29.5 ± 3.6 | 35.1 ± 2.8 |

### *4.3.2 Mechanical- and Electrical-Stimuli-Induced Hemodynamic and Light Scattering Changes*

A typical example of electrical-stimulation-induced hemodynamic and light scattering from a rat ipsilateral spinal cord over time is shown in Figure 4.1. There were consistent stimulation-induced responses in [HbO], [Hb], [HbT] and SO2 over 5 blocks. After averaging all blocks and subtracting baseline, as shown in Figure 4.2, relative changes of five physiological parameters over animals were obtained from the bilateral spinal cord (A-B) and SI (C-D). In particular, the ipsilateral, but not the contralateral, spinal cord tended to show long-lasting (~30 s) responses in [HbO], [Hb], [HbT] and SO2. In contrast, the contralateral, but not the ipsilateral, SI tended to show short (~10 s) responses in [HbO], [HbT], SO2, and $\mu_s'$. Averages of 30 s and

10 s were used to assess any statistically significant stimulus-induced effect in the spinal cord and SI, respectively.

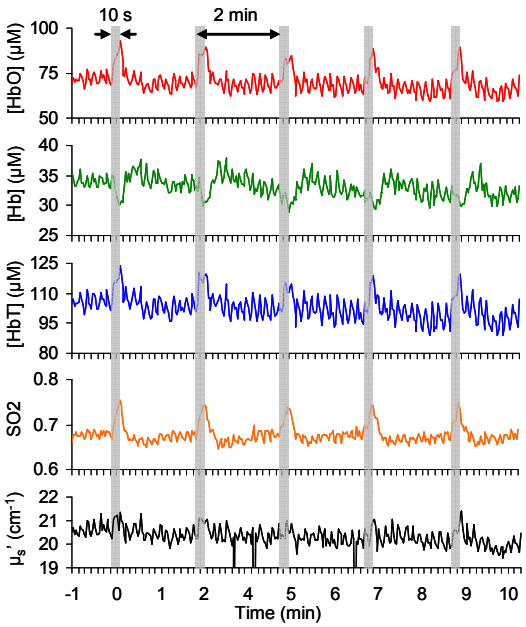


Figure 4.1 An Example of Hemodynamic Parameters and Light Scattering in The Ipsilateral Spinal Cord During Electrical Stimulation (15 V-10 Hz-1 ms pulse duration). Stimulation length was 10 s in a 5-blocks design noted by grey bars.

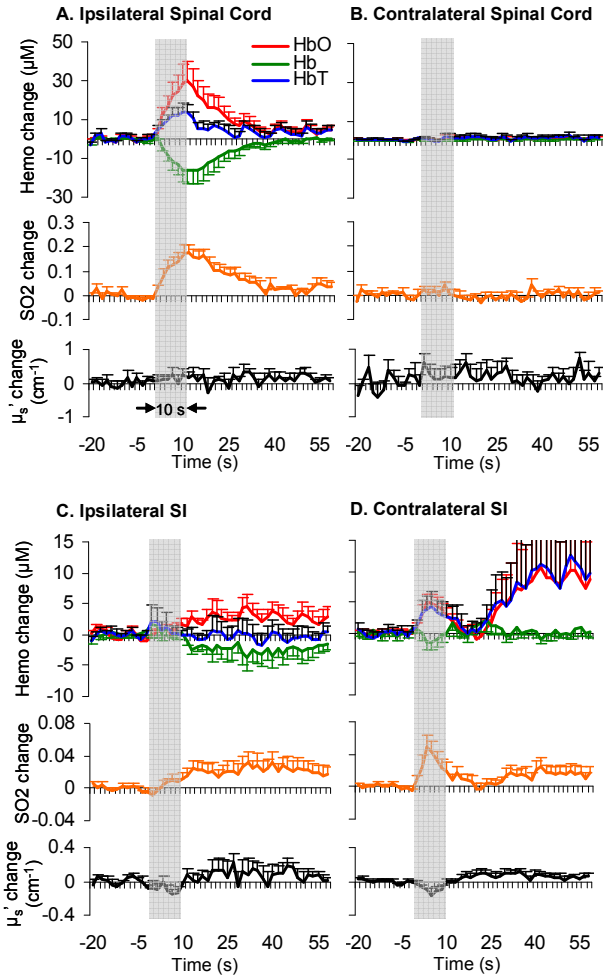


Figure 4.2 Examples of Relative Changes in Hemodynamic Parameters and Light Scattering from Bilateral Spinal Cord and SI During Electrical Stimulation (15-V; *n* = 10). **A**: ipsilateral spinal cord; **B**: contralateral spinal cord; **C**: ipsilateral SI; **D**: contralateral SI.

Figure 4.3 indicates stimulus-induced effects in all five physiological parameters under six stimuli in the spinal cord and SI. At the spinal cord level, [HbO] and SO2 in the ipsilateral side showed a reliable stimulus-induced increase as indicated by comparisons against 0 and/or between two sides. A decrease in [Hb] and an increase in [HbT] in the ipsilateral side were only showed under some stimuli. A significant decrease in $\mu_s'$ was shown associated with mechanical brush and pressure in the contralateral spinal cord. At the SI level, mechanical

stimuli failed to produce a significant change. Electrical stimuli induced changes in [HbO], [HbT], and SO2 only from the contralateral side. A decrease in $\mu_s'$ was shown bilaterally under 10- and 15-V electrical stimulation.

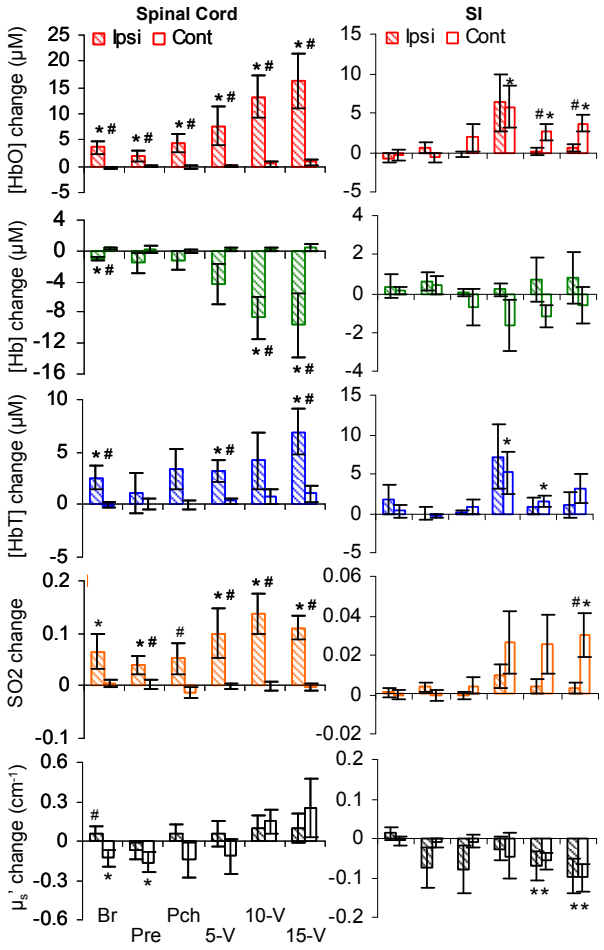


Figure 4.3 Mean Changes in Hemodynamic Parameters and Light Scattering During Mechanical and Electrical Stimulation ($n$ = 10). Left panel: spinal cord; right panel: SI. Shaded bar: ipsilateral side; empty bar: contralateral side. A significant change is noted by *; a significant difference between two sides is noted by # ($p$ < 0.05).

*4.3.3 Temporal Characteristics of Hemodynamics in The Spinal Cord and SI*

All hemodynamic parameters, i.e. [HbO], [Hb], [HbT] and SO2, tended to give reliable responses to peripheral stimuli (Figure 4.3). However, these parameters appeared to bear various degrees of noise-like oscillation as shown in the baseline and inter-stimulus periods

(Figure 4.1). Prior to investigating a stimulus-induced temporal pattern of hemodynamics, a parameter with the highest level of signal-noise-ratio (SNR) needed to be determined. This parameter should be considered as the most reliable candidate to describe a temporal profile.

A Z score, calculated by a maximal change (within 30 s in the spinal cord or 10 s in the SI) divided by standard deviation of a 20 s-baseline in individual rat, was utilized to approximate a SNR. The greater a Z score is, and the better a SNR is. Figure 4.4 demonstrates the SNRs in the ipsilateral spinal cord (A) and contralateral SI (B) under various stimuli. The mechanical-stimuli-induced responses in SI were excluded, because it was failed to show any statistical significance (Figure 4.3). Overall, SO2 and [HbO] tended to provide better SNRs than [Hb] and [HbT] in both the spinal cord and SI under various stimuli (Figure 4.4).

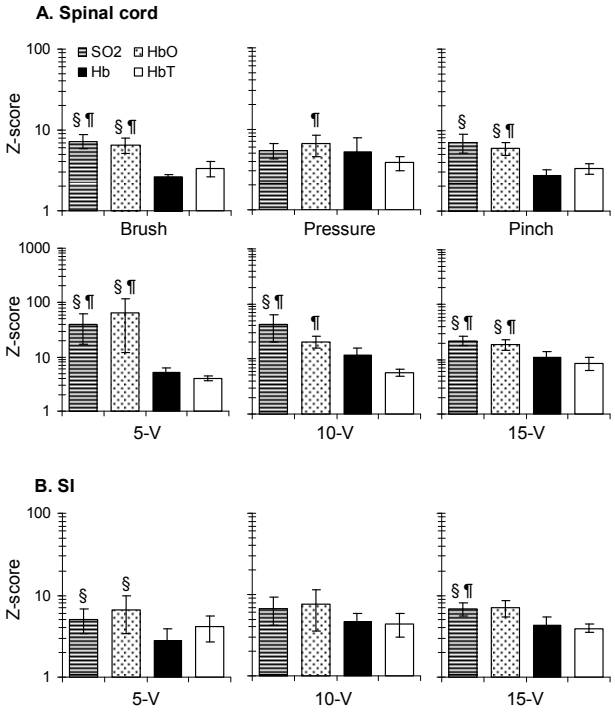


Figure 4.4 Signal-Noise-Ratios of Hemodynamic Parameters from The Spinal Cord and SI During Peripheral Stimulation (*n* = 10). SO2 and HbO were compared to the other two parameters, respectively. A significant difference from Hb is noted by §; a different from HbT is noted by ¶.

Table 4.2 depicts three temporal characteristics of [HbO] and SO2 during functional activation, including onset, peak, and duration. Onset was defined as the first time point from the start of stimulation when a Z score (i.e. [HbO] or SO2 change divided by standard deviation of a 20 s-baseline) was greater than 1.96 (i.e. it reached to a statistically significant level; $p$ = .05). Peak was defined as the time point when a maximal change occurred. Duration was defined as a period between an onset and the first time point when a Z score returned below 1.96 (i.e. an effect was nullified). The column next to duration denotes number of subjects showing an onset (i.e. a significant change happened; Z > 1.96; $p$ < .05).

Table 4.2 Temporal Characteristics in Terms of Onset, Peak, and Duration (s) in HbO and SO2. Number of subjects showing a significant onset is noted by n ($p$ < 0.05).

| | | HbO | | | | SO2 | | | |
|---|---|---|---|---|---|---|---|---|---|
| | | Onset | Peak | Duration | n | Onset | Peak | Duration | n |
| Ipsi SP | Br | 4.8 ± 1.1 (‡) | 9.8 ± .9 | 15.6 ± 3.1 | 8 | 7.3 ± 1.6 | 13.8 ± 1.4 | 19.5 ± 3.6 | 10 |
| | Pre | 4.6 ± 1.4 | 13.7 ± 2.6 | 17.4 ± 4.0 | 9 | 5.0 ± 1.0 | 13.7 ± 2.6 | 17.2 ± 3.7 | 9 |
| | Pch | 4.0 ± 1.0 (‡) | 10.0 ± 1.1 | 15.6 ± 3.3 | 8 | 3.5 ± .5 | 13.1 ± 1.8 | 19.8 ± 3.2 | 8 |
| | 5-V | 3.2 ± .7 (‡) | 10.8 ± .9 (†) | 23.5 ± 4.1 (†) | 10 | 4.2 ± .7 (‡ †) | 12.3 ± .8 (†) | 30.8 ± 4.5 (†) | 10 |
| | 10-V | 4.0 ± 1.0 (‡) | 11.5 ± .9 (†) | 29.2 ± 3.8 (†) | 10 | 2.8 ± .5 (‡) | 11.0 ± .4 (†) | 35.3 ± 3.8 (†) | 10 |
| | 15-V | 3.8 ± 1.5 | 12.3 ± 1.1 (†) | 33.7 ± 5.2 (†) | 10 | 4.2 ± 1.5 (‡ †) | 13.3 ± 1.0 (†) | 30.7 ± 6.2 (†) | 10 |
| Cont SI | Br | 2.2 ± 1.5 | 5.0 ± 1.9 | 15.0 ± 13.3 | 3 | 3.3 ± 1.7 | 3.3 ± 1.7 | 2.5 ± .8 | 2 |
| | Pre | 5.0 ± 3.3 | 5.0 ± 3.3 | 1.7 ± 0 | 2 | 8.3 | 8.3 | 1.7 | 1 |
| | Pch | 4.2 ± 4.2 | 6.7 ± 1.7 | 4.2 ± 2.5 | 2 | 2.8 ± 2.8 | 4.4 ± 2.4 | 3.3 ± 1.7 | 3 |
| | 5-V | 1.9 ± .8 | 4.1 ± 1.1 | 6.7 ± 2.1 | 7 | 1.1 ± .6 | 4.4 ± 1.2 | 9.2 ± 2.3 | 6 |
| | 10-V | 3.3 ± .7 | 4.8 ± .7 | 4.5 ± 1.6 | 7 | 2.5 ± .5 | 4.0 ± .6 | 5.8 ± 1.7 | 8 |
| | 15-V | 2.9 ± .9 | 5.4 ± .8 | 13.8 ± 4.6 | 8 | 1.9 ± .5 | 3.7 ± .2 | 10.4 ± 2.1 | 9 |
| Ipsi SI | Br | 23.8 ± 6.2 | 38.3 ± 9.1 | 19.0 ± 8.7 | 8 | 15.3 ± 7.3 | 33.1 ± 12.3 | 22.8 ± 10.8 | 6 |
| | Pre | 9.8 ± 3.1 | 21.9 ± 9.8 | 19.5 ± 9.1 | 7 | 13.7 ± 9.7 | 33.0 ± 13.4 | 24.0 ± 15.9 | 5 |
| | Pch | 27.4 ± 9.5 | 47.6 ± 8.4 | 18.8 ± 5.6 | 7 | 22.8 ± 8.5 | 52.5 ± 12.7 | 32.8 ± 11.6 | 6 |
| | 5-V | 20.2 ± 8.8 | 30.5 ± 6.7 | 21.4 ± 12.1 | 7 | 23.3 ± 6.5 | 35.4 ± 5.8 | 16.3 ± 9.5 | 8 |
| | 10-V | 15.0 ± 4.4 | 33.0 ± 5.4 | 26.5 ± 5.9 | 9 | 15.6 ± 5.2 | 26.7 ± 6.4 | 13.2 ± 4.0 | 9 |
| | 15-V | 7.6 ± 2.6 | 23.5 ± 7.5 | 21.7 ± 8.8 | 9 | 18.5 ± 6.1 | 29.8 ± 6.2 | 31.3 ± 9.8 | 8 |

The ipsilateral spinal cord and contralateral SI tended to show a similar onset of a hemodynamic response (in [HbO] or SO2) under electrical stimulation (Table 4.2). No

comparison between the two regions was performed under mechanical stimulation, because the sample sizes in the contralateral SI were very small. Moreover, the hemodynamic response in the ipsilateral spinal cord reached to a peak later and sustained longer than those in the contralateral SI (as noted by † in Table 4.2). Finally, the ipsilateral SI tended to show a delayed hemodynamic response as compared to the spinal cord (as noted by ‡ in Table 4.2).

*4.3.4 Formalin-Induced Hemodynamic and Light Scattering Changes*

Figure 4.5 demonstrates hemodynamic and light scattering changes in the first 5 min post formalin injection from four areas. Vigorous signal changes tended to occur in the first 60 s from all areas. Statistical analyses on the first 60 s-averages confirmed (1) significant increases in [HbO] and SO2 with concomitant decreases in [Hb] and [HbT] from the ipsilateral SI; (2) an increase in [HbO] and a decrease in [Hb] from the ipsilateral spinal cord; (3) an increase in SO2 from the contralateral spinal cord (Table 4.3). It is noteworthy that due to massive bleeding at some scanning sites and a death of one rat, the sample sizes at four areas were varied (bilateral SI and contralateral spinal cord: $n$ = 8; ipsilateral spinal cord: $n$ = 9).

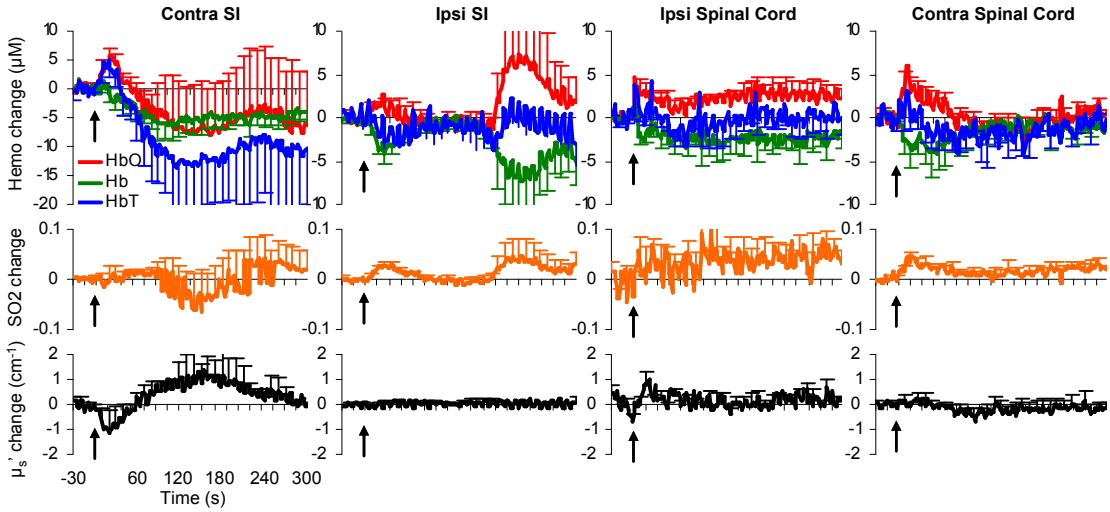


Figure 4.5 Time Courses of Hemodynamic and Light Scattering Changes from the Spinal Cord and SI for the First 300 s Post Formalin Injection. Black arrows denote the injection time. Sampling rate: 0.6 Hz.

Table 4.3 Mean Changes of Hemodynamic Parameters and Light Scattering within 60 s Post Formalin Injection from Bilateral Spinal Cord and SI. *: significant change ($p < 0.05$).

| | Cont SI | Ipsi SI | Ipsi SP | Cont SP |
|---|---|---|---|---|
| **[HbO]** (μM) | 2.1 ± 1.3 | .8 ± .3 (*) | 2.2 ± .8 (*) | 2.5 ± 1.8 |
| **[Hb]** (μM) | -1.5 ± 1.3 | -2.3 ± .6 (*) | -1.6 ± .7 (*) | -2.8 ± 1.8 |
| **SO2** | .003 ± .01 | .02 ± .002 (*) | .02 ± .03 | .03 ± .007 (*) |
| **[HbT]** (μM) | .5 ± 2.2 | -1.3 ± .6 (*) | .3 ± .5 | -.1 ± .8 |
| **$\mu_s$'** ($cm^{-1}$) | -.5 ± .5 | -.002 ± .02 | .3 ± .2 | .05 ± .2 |

Figure 4.6 depicts time courses of hemodynamic and light scattering changes over 45 min at a resolution of 5 min. A long-lasting effect post injection was indicated by some parameters from the bilateral SI and ipsilateral spinal cord (Table 4.4). Contrast analysis (as noted by [a] in Table 4.4) and *post hoc* multiple comparisons with Fisher LSD (as noted by * in Figure 4.6) suggested (1) a linear decrease in SO2 from the contralateral SI; (2) a linear decrease in [HbT] from the ipsilateral SI; and (3) a linear decrease in SO2 from the ipsilateral spinal cord.

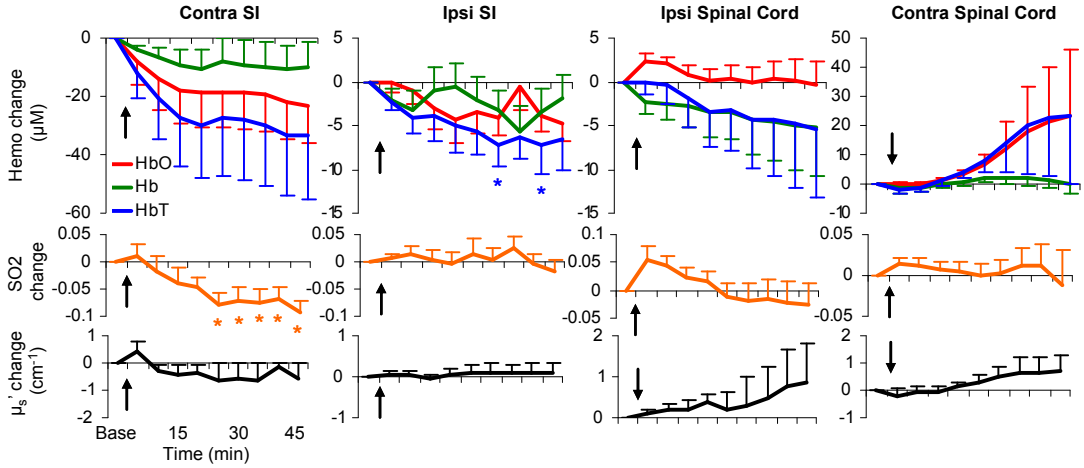


Figure 4.6 Full Time Courses of Hemodynamic and Light Scattering Changes from The Spinal Cord and SI Post Formalin Injection. Black arrows denote the injection time. A significant change is noted by * (*post hoc* Fisher LSD; $p < 0.05$).

Table 4.4 P-Values of Main Effects of Time on Hemodynamic and Light Scattering Changes over Full Time Course. *: significant change; [a]: significant linear component by *post hoc* contrast analysis ($p < 0.05$).

| | Cont S1 | Ipsi S1 | Ipsi SP | Cont SP |
|---|---|---|---|---|
| **SO2** | .001 (*[a]) | .61 | .024 (*[a]) | .98 |
| **[HbO]** | .012 (*) | .08 | .48 | .38 |
| **[Hb]** | .45 | .40 | .71 | .33 |
| **[HbT]** | .046 (*) | .046 (*[a]) | .79 | .33 |
| **$\mu_s$'** | .35 | .98 | .80 | .35 |

## 4.4 Discussion

We measured focal hemodynamic and light scattering changes in the SI and spinal cord by using fiber optics. According to a phantom experiment with a similar system, penetration depth of optical signal was ~1 mm (Liu et al., 2008). Thus, measured areas should overlap a considerable volume of regions of interest, including arteriole, capillary, venule, and neurons. Our absolute measures of [HbT] in the SI were in a physiological range as compared to other study (Plesnila et al., 2002). It is unsurprising that stimulus-induced responses were commonly shown in the ipsilateral spinal cord and contralateral SI. This was in line with the neuroanatomy of somatosensory pathways. When the primary afferents are activated by external stimuli (e.g. brushing) in peripheral, action potentials are generated and transmitted on the primary afferents. They first reach the ipsilateral spinal cord dorsal horn. Then, several ascending tracts that originate in the spinal cord deliver the sensory information to supraspinal structures, such as the thalamus in the contralateral hemisphere. As the information further reaches the contralateral SI via the ventral posterolateral nucleus of thalamus, the somatic sensory aspect of the stimulation is perceived. The ipsilateral SI was also suggested to be involved in somatosensory processing as examined by human neuroimaging techniques (Nihashi et al., 2005; Hlushchuk and Hari, 2006; Zhu et al., 2007). This ipsilateral activation tended to be relied on the interconnection between two hemispheres via the corpus callosum (Killackey et al.,

1983). The neuronal electrical activity in the ipsilateral SI occurred later, and was weaker in intensity as compared to that in the contralateral side (Zhu et al., 2007). Our observed hemodynamic responses were alike the electrophysiology in both aspects (Figure 4.2 and Table 4.2). Up to date, physiological significance of the activation in the ipsilateral SI is unclear.

*4.4.1 Electrical, But Not Mechanical, Stimuli Produced An Intensity-Dependent [HbO] Increase*

As shown in Figure 4.2, the electrical stimulus-induced increase in [HbO] from the ipsilateral spinal cord tended to be positively correlated to the stimulus intensity, indicated by a one-way within-subject ANOVA ($F(2, 18) = 4.15$, $p = 0.03$). On the other hand, the mechanical stimulus-induced failed to show such dependence ($F(2, 18) = 1.85$, $p = 0.19$). Such dependence should be related to the spinal cord metabolic level determined by local neuronal activities in response to periphery stimulation. The disparity between two stimuli may be related to the nature of stimuli.

In periphery, the primary afferents respond differently to external stimuli in intensity- and modality-dependent manners. Modality is defined as a general type of stimulus and the specific type of receptor activated by such stimulus (Kandel et al., 2010). As an innocuous stimulus, brushing only activates A-β primary afferent fibers carrying information from mechanoreceptors, whereas noxious pinching primarily activates A-δ and C fibers carrying information from mechanoreceptors and nociceptors (Georgopoulos, 1976). As an unnatural stimulus, 15-V electrical stimulation was more likely to activate A-δ fibers than 5- and 10-V stimulation (Peng et al., 1999). There is no evidence indicating that electrical stimulation-induced primary afferent activation is modality-specific. Furthermore, mechanical pressuring and pinching persisted for 10 s, whereas electrical stimulation was delivered in terms of individual pulses at 10 Hz for 10 s. Therefore, electrical stimuli might activate more neurons than mechanical stimuli at a certain parameter. At the spinal cord level, there are low-threshold (only respond to innocuous stimuli), high-threshold (only respond to noxious stimuli), and wide-dynamic-range neurons (respond to both innocuous and noxious stimuli), which receive sensory inputs from multiple primary

afferents (Chung et al., 1986). The electrophysiological energy consumption at the spinal cord level is the sum of these three types of neurons. It was, therefore, likely that the energy consumptions at the spinal cord were similar among graded mechanical stimulation, whereas they were correlated to intensities of electrical stimuli.

*4.4.2 Regional Characteristics of Hemodynamic Responses*

Both the ipsilateral spinal cord and contralateral SI showed bell-shaped hemodynamic responses that were correlated to neuronal activation (Figure 4.2). However, there were some noticeable differences between two regions. First, amplitudes of [HbO] and SO2 increases in the spinal cord tended to be greater (Figure 4.3), and to persist longer, as compared to those in the SI (Table 4.2). These findings indicated that metabolism at the spinal cord level tended to be greater than that at the SI level in sensory processing. Sensory information is first processed at the spinal cord level, and transmitted through various ascending tracts to supraspinal structures. These processes may require more energy (e.g. oxygen and glucose) than the processes in the contralateral SI, where neuron clusters are highly isolated for perception of a specific body surface (known as dermatome).

Second, a decrease in [Hb] during neuronal activation was shown in the spinal cord, but not in the contralateral SI (Figures 4.2-3). Instead, an increase in [HbO] was shown in both areas. A growing body of evidence indicated that during neuronal activation, a local increase in blood flow was mainly due to vasodilatation of arteries but not veins in the somatosensory cortex (Takano et al., 2006; Kim et al., 2007). As the arteries are the major HbO carriers, arterial dilation should be responsible for the observed increase in [HbO]. Changes in [Hb] tend to be affected by local metabolism and vasodilatation of venules. An increase in local metabolism results in more Hb, whereas dilating venule diameter accelerates the removal of Hb away from the activated area that results in a decrease in [Hb]. At the spinal cord level, the later effect was likely predominant.

*4.4.3 Hemodynamic Signatures of Spinal Cord and SI in Responses to A Long-lasting Noxious Stimulus*

Formalin test is a well-established model to study long-lasting pain. Following single subcutaneous injection of formalin, animals showed immediate pain-behaviors (e.g. licking and elevating injected paw) for the first 5 min (Phase I), and after a 10-15 min quiescent period, they started to show such pain-behaviors again for more than 1 hour (Phase II) (Dubuisson and Dennis, 1977). This biphasic pattern was also shown by excitability of the spinal cord sensory neurons in anesthetized animals (Dickenson and Sullivan, 1987). In Phase I period, significant hemodynamic responses were shown in the ipsilateral SI and bilateral spinal cord, but not in the contralateral SI (Table 4.3, Figure 4.5). A long-lasting linear decrease in SO2 was only shown in the contralateral SI and ipsilateral spinal cord (Table 4.4, Figure 4.6). The sustained decrease in SO2 tended to be correlated to the Phase II.

An increase in blood flow to a specific brain region during activation is believed to be a hemodynamic signature of neuronal activation, which is referred as to hyperemia (Iadecola, 2004). It was primarily due to arterial dilation (Takano et al., 2006; Kim et al., 2007). As the metabolic rate increase was far less than the arterial blood influx (Fox and Raichle, 1986), the regional SO2 should be elevated and approach to arterial SO2. Our observations of [HbO], [Hb], [HbT] and SO2 during electrical stimulation were coincident. However, this phenomenon seemed unlikely in formalin test. None of hemodynamic parameters showed significant changes in the contralateral SI during Phase I (Figure 4.5). One explanation was that formalin induced such intense neuronal activation in SI that the concomitant metabolic rate raised up quickly and resulted in a considerable amount of Hb accumulated in the activated area. The SO2 as a ratio of [HbO] / ([HbO] + [Hb]) will not be changed if an increase in [Hb] is identical to that in [HbO] in percentage. In Phase II, vessels might meet a ceiling effect and were unable to dilate any more in order to provide excessive HbO to the activated area. Regional SO2 decreased, as oxygen was constantly consumed by neurons during activation.

*4.4.4 Regional Characteristics of Light Scattering*

The light scattering effect of the white matter was greater than that of the grey matters (Gebhart et al., 2006), which were confirmed by our observations in the spinal cord and SI (Table 1). As our measures were obtained on the surface of the spinal cord and SI, the light scattering effect was mainly from the white matter at the spinal cord level, whereas scattering effect was from the grey matter at the brain level. No significant change in light scattering was found in the ipsilateral spinal cord during neural activation (Figure 4.3). A decrease followed by an increase was shown in bilateral SI during high level electrical stimulation (10 and 15-V). Such temporal shape tended to occur in the contralateral SI during Phase I of formalin test (Figure 4.6). Both positive and negative light scattering changes were shown by a functional OCT study in rat somatosensory cortex during forepaw stimulation (Aguirre et al., 2006). Our observed decease might be an integrated response over the regions of interest.

## 4.5 Conclusion

Changes in multiple quantifiable hemodynamic parameters were found in the spinal cord and SI during brief periphery stimulation. Patterns of hemodynamic responses did not show a distinction between innocuous and noxious stimulation. Pattern of hemodynamic response during formalin-induced sustained pain was different from that during brief stimulation. A linear decrease in SO2 was correlated to neural activation in the ipsilateral spinal cord and contralateral SI.

# APPENDIX A

# SUPPLEMENTAL MATERIALS ON DIFFUSE OPTICAL IMAGER

*Data acquisition*

A commercialized, continuous-wave, NIRS brain imager for Dynamic Near-Infrared Optical Tomography (DYNOT, NIRx Medical Technologies, USA) was used to measure hemodynamics of the rat brain. DYNOT can drive up to 31 bifurcated optical optodes and utilize two wavelengths of near infrared light (760 and 830 nm). Signals at two wavelengths were acquired simultaneously and independently. During one data acquisition cycle, each optode was used as light source once, in an order from Optode 1 to the last one. When an optode served as a source, all other optodes (including the source optode itself) detected reflectance of light simultaneously. The light propagation path is illustrated in Figure A.1A, where two detectors are receiving optical signals that are emitted from a source optode. The optical penetration depth is a function of the source-detector separation (Feng et al., 1995). The wider the separation is, the deeper depth the optical signal could reach to.

*Optode-array arrangement for rat brain measurement*

In the rat measurement, 26 optodes (2 mm in diameter) were used and arranged by a plastic frame in a horizontal plane (Figures A.1B and 1C). A total number of 676 (26 X 26) data points (signals from total source-detector pairs) were gathered after one data acquisition cycle at one wavelength of light. The sampling rate was about 2 data acquisition cycles per second (2 Hz). This 26-optode array covered a rectangular region with an anterior-to-posterior distance of 16.1 mm and a left-to-right distance of 16.4 mm (Figure A.1C). To obtain the consistency of array placement in the measurement protocol, the most posterior row of the array (including Optode 23-26) was aligned by the lambdoid sutures; the two middle probes (i.e. Optode 24, and 25) were evenly sided from the midline suture (shown in Figure A.1B). The last check was to make sure Optode 2 on the midline suture (Figure A.1B). All of the optical probes were in good contact with the rat skull, and a layer of mineral oil (Equate, US) was applied before array placement to avoid air gap between the optodes and surface of the bone.

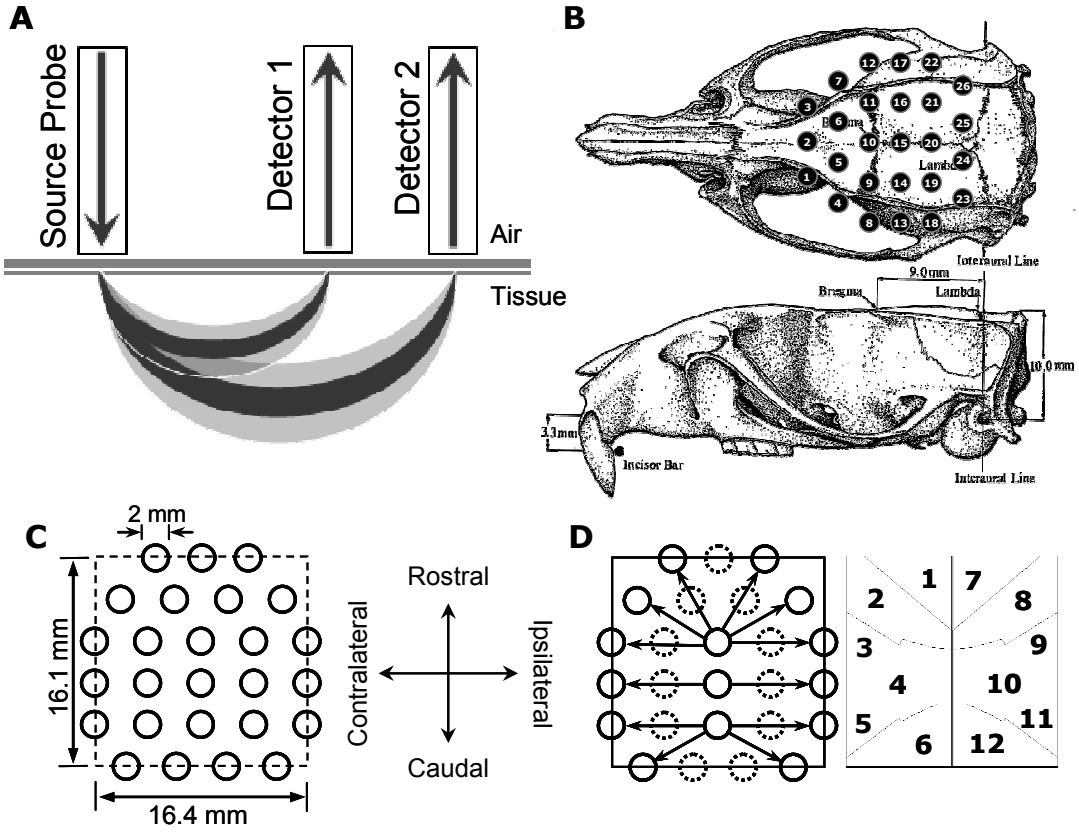


Figure 1. General Information on Optical Theory and Instrumentations. **A**. Light propagation paths from a source optical probe to two detectors. Photons initially enter into the tissue, travel through a banana-like pathway, and emit out of tissue and to be detected by detectors. **B**. The placement of optode array (containing 26 optodes) above the rat skull (Paxinos, 1998). **C**. Physical dimensions of the 26-optodes-array and directions for each reconstructed image (e.g. rostral, caudal, contra-, and ipsilateral). In particular, the right side represents the ipsilateral; the left represents the contralateral. **D**. Optode selections for topography. 12 source-detector pairs were used. Of the total 26 optodes, the selected ones are highlighted by solid circle, and the un-selected by dash-line circle. Arrow presents a direction from a source to a detector. The source optodes are #10, #15, and #20 in the midline. 12 patches are made, each of which is associated with one source-detector pair.

*Image reconstruction: tomography*

A NIR data processing program, HOMER (PMI, US), was used to analyze optical signals obtained by DYNOT. This software is based on a widely accepted mathematical light diffusion model, which has two assumptions to be satisfied: (a) the light scattering coefficient

($\mu_s$') of the target (either rat brain or tissue phantom) is constant and much larger than its absorption coefficient ($\mu_a$) and (b) both the spatial and temporal variation in $\mu_a$ are small (Durduran et al., 1997; Li et al., 2004). Thus, a change in optical density (ΔOD) obtained by a pair of source and detector is mainly determined by the absorption changes in both oxy- (Δ[HbO]) and deoxy- hemoglobin concentration (Δ[Hb]) along a photon pathway inside the tissue, as shown by Eq. 1,

$$\begin{bmatrix} \Delta OD_{\lambda_1} \\ \Delta OD_{\lambda_2} \end{bmatrix} = A \cdot \begin{bmatrix} \Delta[HbO] \\ \Delta[Hb] \end{bmatrix}, \quad (1)$$

where ΔOD is wavelength dependent, and *A* is a transfer function (a constant matrix) that describes direct relationships between changes in optical densities and hemodynamic chromosphere concentrations (Li et al., 2004; Kim et al., 2005). Since Matrix *A* is usually easy to determine, [HbO] and [Hb] changes could be solved by multiplying the inversed *A* on both sides of Eq. 1. To ensure that [HbO] and [Hb] changes are solvable, two or more wavelengths of optical measures are needed.

A diffusion equation has been widely accepted as a photon migration model to quantify the photon density ($P(\mathbf{r}, t)$) in diffusive turbid media (Arridge, 1999),

$$\frac{1}{\boldsymbol{c}}\frac{\partial}{\partial \boldsymbol{t}}\boldsymbol{P}(\mathrm{r},\boldsymbol{t}) - \boldsymbol{D}\nabla^2\boldsymbol{P}(\mathrm{r},\boldsymbol{t}) + \mu_{\boldsymbol{a}} \cdot \boldsymbol{P}(\mathrm{r},\boldsymbol{t}) = \boldsymbol{S}(\mathrm{r},\boldsymbol{t}), \quad (2)$$

where *c* is the light speed in a tissue, ***r*** a vector representing a relative distance to the origin (0,0), *t* the time, *D* the diffusion coefficient, and *S* the light source. According to Eq. 2, a photon density at any spatial location and any time can be determined if all the other variables are known. In other words, Eq. 2 describes a quantitative relationship between a regional photon density and the light source.

In our study, the measures by various source-detector pairs can be written as,

$$\begin{bmatrix} \Delta OD(\text{Ch } 1) \\ \dots \\ \Delta OD(\text{Ch } n) \end{bmatrix}_{z=0} = B \cdot \begin{bmatrix} \Delta S(x_1 y_1) & \dots & \Delta S(x_1 y_m) \\ \dots & \dots & \dots \\ \Delta S(x_l y_1) & \dots & \Delta S(x_l y_m) \end{bmatrix}_{z=k} \quad (3)$$

where Δ*OD*(Ch i) is a change in optical density captured by a detector at the surface of tissue (*z* = 0) from a source-detector pair, labeled by channel i (i = 1...*n*); *B* is a transfer function determined by Eq. 2; Δ*S* is a perturbation distribution in $\mu_a$ at a certain depth along z-axis (*z* = *k*) inside the tissue. Eq. 3 indicates that if an absorption perturbation map is known, a change in optical density measured at the tissue surface (*z* = 0) can be determined. Inversely, from a backward perspective, an absorption perturbation in the tissue can be solved under two conditions that changes in optical density are measured at the air-tissue boundary (*z* = 0), and the inverse of Matrix *B* exists. However, Matrix *B* is ill-posed, and its inverse matrix does not usually exist. One of the solutions to the inverse problem is to regularize Matrix *B* when solving the inverse problem. In our study, a regularization method was selected in HOMER (Li et al., 2004); therefore, the 2D absorption perturbation maps (Δ*S*) in *x*-*y* the coordinate plane at any *z*-depth can be obtained at two wavelengths, respectively. Changes in hemodynamic parameters, such as Δ[HbO] and Δ[Hb], at each pixel can be further determined by Eq. 1.

The general schemes to form tomographic images for rat brain data were to: (a) convert the DYNOT outputs to a specific format to be compatible with HOMER; (b) normalize each channel (i.e. divide any channel with source = i and detector = j, by another channel with source and detector = i); (c) run a median filter (every 5 data points or 2.5 s); (d) adjust contra-and-ipsilateral presentations (i.e. always put the left side of image as the contralateral); (e) provide a low pass filter with a cutoff frequency at 0.1 Hz; (f) set the measures of 5 s before injection as baseline; (g) assuming that the combined thickness of the skull, pia mater, and dura mater is 1 mm, set the *z* plane of reconstructed rat brain images at 2 mm (for the SI), 3 mm (for the ACC) and 6 mm (for the SII, thalamus, and PAG), respectively; (h) generate reconstructed images (21 by 21 pixels) at two wavelengths, respectively; and (i) use Eq. 1 to get the hemodynamic responses in terms of Δ[HbO], Δ[Hb], and Δ[HbT] (i.e. Δ[HbO] + Δ[Hb]). As a result, temporal resolution of the tomographic images was 2.5 s (0.4 Hz), and the pixel size was

0.77 X 0.78 $mm^2$ (i.e. an *x*- or *y*-axis length divided by 21). All processing procedures were completed in either HOMER or Matlab (MathWorks, US).

*Image reconstruction: topography*

Topography is a simple way to interpret hemodynamic responses by using fewer source-detector pairs than those used in tomography. These selected pairs were independent or nearly independent to each other. Thus, regional hemodynamics is solely determined by only one geometrically related source-detector pair. Validity of this method is based on one assumption that light intensity change is mainly due to absorption perturbation, but not light scattering change.

Twelve source-detector pairs were selected (Figure A.1D). Of those pairs, Optodes 10, 15, and 20 (on the midline) served as sources, and the rest of the chosen optodes (Optodes 1, 4, 8, 13, 18, 23 on the left and Optode 3, 7, 12, 17, 22, and 26 on the right) acted as detectors (Figure A.1B). The distance between the sources and detectors ranged from 6.5 to 8.2 mm. The brain image was, therefore, divided into 12 subdivisions (Figure A.1D). Hemodynamic responses in each subdivision were only determined by one geometrically affiliated source-detector pair. Signal change in a subdivision, theoretically, represents a comprehensive effect of all optical property changes (i.e. absorption) along the full length of photon pathway depicted in Figure A.1A.

The general schemes to form topography images were to: (a) get logarithm of each data point from DYNOT output; (b) normalize each channel by subtracting the baseline measure (i.e. the median value of 5-s recording prior injection); (c) run a median filter (every 20 data points, or 10 s); (d) adjust contra-and-ipsilateral presentations (i.e. always put the left side of image as the contralateral); and (e) use Eq. 1 to obtain the hemodynamics. Temporal resolution of the topographic image was then reset at 10 s (0.1 Hz). All procedures to obtain topography were finished in Matlab.

*Validation of imaging a phantom absorber by using tomographic image reconstruction*

A phantom measurement was conducted to investigate the performance of tomographic method based on DYNOT signals. 28 optodes were used (Figure A.2A), resulting in a 784 data points per data acquisition cycle. The sampling rate was also about 2 Hz, and this 28-optodes-array covered a 12.2 X 18.8 $mm^2$ region (Figure A.2A). A tissue phantom made of 3% intralipid solution (Fresenius Kabi, Sweden) was used to simulate the scattering effect of natural tissue on optical signals. As demonstrated in Figure A.2A, a black capillary (2 mm in diameter) was completely merged in the intralipid solution to mimic an absorber within the medium or an activated brain area in the rat brain. The capillary was detached vertically at the center of a rectangular container filled with the intralipid solution. The 28-optodes-array was fixed in position with a constant distance of 5 mm above the tip of the capillary. The initial position of the capillary was beneath the center of the array. The container was placed on a grid paper and was able to move freely. Fourteen movements were made from the initial central spot (leftward: 5, 10, and 15 mm; rightward: 5, 10, and 15 mm; forward: 5, 10, 15, and 20 mm; backward: 5, 10, 15, and 20 mm). At each position, 60-s-steady-state data was measured and processed.

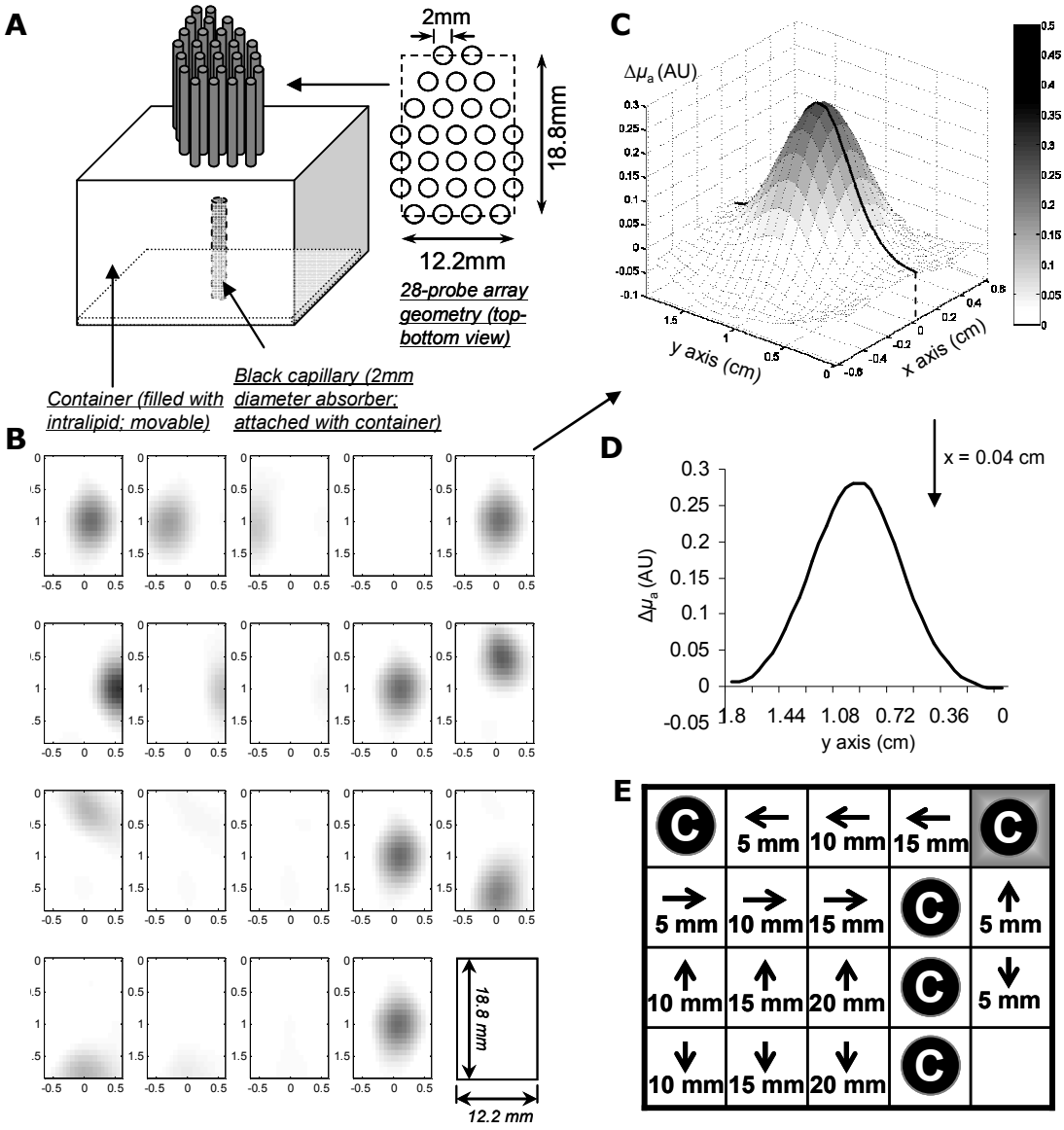


Figure A.2 Experimental setup and results from phantom study. **A**. Experimental step for phantom protocol. A 28-optodes-array was used, and perpendicularly immersed into an Intralipid solution in a container. A black capillary (act as an absorber) was 5 mm below the surface of the optical array in the Intralipid solution. The capillary was vertically attached to the bottom of the box. **B**. Tomographic images at a wavelength of 760 nm and a depth of 5 mm, with respect of 3 displacements (5, 10, 15 mm) in each of 4 directions (arrow: left, right, up, down), as illustrated in **E**. "C" means the absorber positioned in the center of the array. **C.** A representative 3-D surf presentation (Matlab) was generated. **D**. A 2D presentation was plotted at $x$ = 0.04 cm.

A set of reconstructed tomographic images at the wavelength of 760 nm were obtained using the procedures mentioned above. The spatial dimension was 0.58 X 0.89 $mm^2$ of a pixel. Figure A.2B shows 4 rows of images at a depth of 5 mm; they represent different absorber locations by moving the ink-filled, 2 mm-diameter capillary (Figure A.2A) in four directions: left, right, up, and down from the center, 5 mm in step interval, as described in Figure A.2E. A boundary-identifiable dark spot is seen in each sub-figure (Figure A.1B), indicating an increase in absorption caused by the capillary in each of the respective case. An example of 2D absorption perturbation induced by the central-positioned capillary is re-plotted in a 3D pattern, in which the *z* axis indicates signal intensity (Figure A.2C). Figure A.2D illustrates a 2D representation of the absorption change ($\Delta\mu_a$) at the coordinate of $x$ = 0.04 cm, where a global maximum was included at $y$ = 0.81 cm in Figure A.2C. The full width at half maximum (FWHM) is a parameter commonly used to define the length of an object reconstructed by an imaging system. According to this phantom measure, the FWHM of the dark spot was about 6 mm. In short, our phantom data indicated that the tomographic method was reliably detecting absorption change obtained by DYNOT system with short source-detector optode arrangements.

*Depth location of an activated area in NIR tomography*

With a given depth, 2D tomographic images demonstrate a decent spatial resolution, as indicated by our phantom measures. As shown in Figure A.2B, 5-mm-incremental-motions of the 2-mm-diameter capillary in four directions were correctly reflected by the reconstructed images at an image depth of 5 mm. However, tomographic images at different depths between 2 to 4 mm also gave a clear incidence of the black capillary (data not shown). With the current image reconstruction algorithm, a 2D tomographic image can provide an accurate lateral location, but not depth location for the imaged object or activated area. In other words, any response shown in a tomographic image reconstructed at a chosen depth might actually occur

at a different nearby depth. With this regard, no depth analysis was performed in this study; the depths chosen for 2D tomographic images were 2, 3, and 6 mm to target specific brain regions. A recent development (Niu et al., 2010) had introduced a depth compensation algorithm (DCA) to counterbalance the decay nature of light propagation in tissue. It is possible to form a 3D tomography with DCA; the investigation on how deep the hemodynamic response has occurred post formalin injection will be performed by our next study.

# APPENDIX B

## A MATHMATICAL MODEL OF [HBT]

*Calculate Pearson correlation coefficient r*

In *Discussion*, we calculated a Pearson correlation coefficient between [HbT] and two other hemodynamic components, i.e. [HbO] and [Hb], when these two components had a substantial a linear relationship with each other. Assume that HbO and Hb changes are followed by a linear regression model, expressed by

$$\mathrm{Hb} = a \cdot \mathrm{HbO} + b + \varepsilon\ ,\ \varepsilon \sim N(\mu, \sigma)\ ,$$

where $a$ is the slope, $b$ the intercept, $\varepsilon$ a random Gaussian noise with a mean of $\mu$ and a standard deviation of $\sigma$.

Replacing Hb by $Y$, and HbO by $X$, respectively, we get

$$Y = a \cdot X + b + \varepsilon\ .$$

The Pearson correlation coefficient $r$ between $Y$ (i.e. $a \cdot X + b + \varepsilon$; Hb) and $X$ (HbO) is,

$$r_{XY} = \frac{E\left[\left(X - \overline{X}\right) \cdot \left(Y - \overline{Y}\right)\right]}{stdev(X) \cdot stdev(Y)} = \frac{E\left\{\left(X - \overline{X}\right) \cdot \left[a \cdot X + b + \varepsilon - \left(a \cdot \overline{X} + b + \mu\right)\right]\right\}}{\sigma_X \cdot stdev(a \cdot X + b + \varepsilon)}$$

$$= \frac{E\left[a \cdot \left(X - \overline{X}\right)^2 + \left(X - \overline{X}\right) \cdot (\varepsilon - \mu)\right]}{\sigma_X \cdot \sqrt{a^2 \cdot \sigma_X^2 + \sigma^2}} = \frac{a \cdot E\left[\left(X - \overline{X}\right)^2\right] + E\left[\left(X - \overline{X}\right) \cdot (\varepsilon - \mu)\right]}{\sigma_X \cdot \sqrt{a^2 \cdot \sigma_X^2 + \sigma^2}}.$$

Since the random noise $\varepsilon$ is independent to $X$,

$$E\left[(X - \overline{X}) \cdot (\varepsilon - \mu)\right] = E(X - \overline{X}) \cdot E(\varepsilon - \mu) = 0 \cdot 0 = 0\ .$$

Then,

$$r_{XY} = \frac{a \cdot \sigma_X^2}{\sigma_X \sqrt{a^2 \cdot \sigma_X^2 + \sigma^2}} = \frac{a}{\sqrt{a^2 + \sigma^2 / \sigma_X^2}} \qquad \text{(Eq. 1)}.$$

Given that HbT = HbO + Hb, the Pearson correlation coefficient $r$ between HbT ($X$ + $Y$) and HbO ($X$) can be further referred to an $r$ between (1 + $a$) · $X$ + $b$ + $\varepsilon$ and $X$.

Simply replacing $a$ by 1 + $a$ in Eq. 1, we get

$$r_{\mathrm{HbT \cdot HbO}} = \frac{1 + a}{\sqrt{(1 + a)^2 + \sigma^2 / \sigma_{\mathrm{HbO}}^2}}\ .$$

*Weak correlations between [HbT] and two other hemodynamics were due to low signal-noise-ratio*

There was a substantial linear relationship between [HbO] and [Hb] changes during brain functioning. [HbT] was a linear function of [HbO] and [Hb] (i.e. [HbO] + [Hb]). In principle, [HbT] should also have a substantial linear relationship with either one. In fact, such relationships were fairly weak (Column 1 and 2 in Table B.1), as compared to the relationships between [HbO] and [Hb] (Column 6 in Table 2.3 in 2.4 *Discussion*). Here, we utilized a mathematical method to prove that the linearity between [HbO] and [Hb] during functional activation was valid, and the paradoxical weak correlations between [HbT] and two other hemodynamics did not contradict the previous statement.

Table B.1 The Pearson Correlation Coefficients between [HbT] and [HbO] or [Hb]. The values in Columns 1 – 2 were obtained by the regular calculation, whereas the values in Column 4 were obtained by a method based on a linear model between [HbO] and [Hb]. The values in Column 3 were used by the later method.

| Period (s) | | Pearson Corr vs [HbO] | Pearson Corr vs [Hb] | Est. $\sigma_{Error}/\sigma_{HbO}$ | Est. Corr vs [HbO] |
|---|---|---|---|---|---|
| Baseline | -5 – -.5 | .13 | .5 | .7 | .13 |
| Brush | 0 – 20 | .16 | .34 | .51 | .17 |
| | 40 – 60 | .45 | .64 | 1.07 | .45 |
| Pinch | 0 – 20 | -.09 | .5 | .49 | -.08 |
| | 40 – 60 | .15 | .54 | .78 | .15 |

We used a linear equation to estimate the [Hb] change as a function of [HbO] change which was symbolized by

$$\mathrm{Hb} = a \cdot \mathrm{HbO} + b + \varepsilon\,, \qquad \text{(Eq. 2)}$$

where *a* denoted a slope, *b* an intercept, and *ε* a random Gaussian noise with a mean of *μ* and a standard deviation of $\sigma_{Error}$. Thus, a Pearson correlation coefficient *r* between [HbT] and [HbO] was expressed by

$$r = \frac{1+a}{\sqrt{(1+a)^2 + (\sigma_{\text{Error}} / \sigma_{\text{HbO}})^2}}, \qquad \text{(Eq. 3)}$$

in which $\sigma_{HbO}$ was the standard deviation of [HbO] changes (Eq. 1). Eq. 3 indicates that *r* is solely determined by *a*, $\sigma_{Error}$, and $\sigma_{HbO}$, when a linear relationship between [HbO] and [Hb] changes (Eq. 2) exists. Estimates of $\sigma_{Error}/\sigma_{HbO}$ were obtained by a regression analysis, and results were shown in Column 3 in Table B.1. Estimates of *r* based on Eq. 3 and $\sigma_{Error}/\sigma_{HbO}$ were almost identical to the conventionally-obtained *r* (Table B.1). This finding indicated that (1) the linear model (Eq. 2) was valid in our scenario; (2) as shown in Eq. 3, the weak [HbT] correlation to either [HbO] or [Hb] was due to a small [HbT] change. The slope between [HbO] and [Hb] was close to -1 (Column 7 in Table 2.3 in 2.4 *Discussion*), indicating that two components tended to cancel out each other and resulted in a tiny [HbT] change. The correlation *r* was, therefore, reduced remarkably by a constant noise (e.g. $\sigma_{Error}/\sigma_{HbO}$). The noise tended to be heavily influenced by non-neuronal factors. As shown in Column 3 in Table B.1, the noise level in the late periods of brush and pinch (i.e. refractory period) tended to be greater than that in baseline (i.e. no brain functioning); the noise in baseline tended to be greater than that in the initial periods (i.e. brain functioning).

REFERENCES

Abrahams V. C., Clinton R. J. and Downey D. (1988) Somatosensory projections to the superior colliculus of the anaesthetized cat. *J. Physiol* **396,** 563-580.

Abramovic Z., Sentjurc M., Kristl J., Khan N., Hou H. and Swartz H. M. (2007) Influence of different anesthetics on skin oxygenation studied by electron paramagnetic resonance in vivo. *Skin Pharmacol. Physiol* **20,** 77-84.

Aguirre A. D., Chen Y., Fujimoto J. G., Ruvinskaya L., Devor A. and Boas D. A. (2006) Depth-resolved imaging of functional activation in the rat cerebral cortex using optical coherence tomography. *Opt. Lett.* **31,** 3459-3461.

Alreja M., Mutalik P., Nayar U. and Manchanda S. K. (1984) The formalin test: a tonic pain model in the primate. *Pain* **20,** 97-105.

Arridge S. R. (1999) Optical tomography in medical imaging. *Inverse Problems* **15,** R41-R93.

Ativanichayaphong T., He J. W., Hagains C. E., Peng Y. B. and Chiao J. C. (2008) A combined wireless neural stimulating and recording system for study of pain processing. *J. Neurosci. Methods* **170,** 25-34.

BAEZ S. and ORKIN L. R. (1963) EFFECTS OF ANESTHETICS ON THE RESPONSE OF THE MICROCIRCULATION TO CIRCULATING HUMORS. *Anesthesiology* **24,** 568-579.

Bagust J., Kerkut G. A. and Rakkah N. I. (1989) The dorsal root reflex in isolated mammalian spinal cord. *Comp Biochem. Physiol A Comp Physiol* **93,** 151-160.

Bartocci M., Bergqvist L. L., Lagercrantz H. and Anand K. J. (2006) Pain activates cortical areas in the preterm newborn brain. *Pain* **122,** 109-117.

Becerra L., Harris W., Joseph D., Huppert T., Boas D. A. and Borsook D. (2008) Diffuse optical tomography of pain and tactile stimulation: activation in cortical sensory and emotional systems. *Neuroimage.* **41,** 252-259.

Berendse H. W. and Groenewegen H. J. (1991) Restricted cortical termination fields of the midline and intralaminar thalamic nuclei in the rat. *Neuroscience* **42,** 73-102.

Bernet-Buettiker V., Ugarte M. J., Frey B., Hug M. I., Baenziger O. and Weiss M. (2005) Evaluation of a new combined transcutaneous measurement of PCO2/pulse oximetry oxygen saturation ear sensor in newborn patients. *Pediatrics* **115,** e64-e68.

Berwick J., Johnston D., Jones M., Martindale J., Martin C., Kennerley A. J., Redgrave P. and Mayhew J. E. (2008) Fine detail of neurovascular coupling revealed by spatiotemporal analysis of the hemodynamic response to single whisker stimulation in rat barrel cortex. *J. Neurophysiol.* **99,** 787-798.

Blatow M., Nennig E., Durst A., Sartor K. and Stippich C. (2007) fMRI reflects functional connectivity of human somatosensory cortex. *Neuroimage.* **37,** 927-936.

Bloos F. and Reinhart K. (2005) Venous oximetry. *Intensive Care Med.* **31,** 911-913.

Blumberg H. and Wallin B. G. (1987) Direct evidence of neurally mediated vasodilatation in hairy skin of the human foot. *J. Physiol* **382,** 105-121.

Boivie J. (1971) The termination of the spinothalamic tract in the cat. An experimental study with silver impregnation methods. *Exp. Brain Res.* **112,** 331-353.

Bornhovd K., Quante M., Glauche V., Bromm B., Weiller C. and Buchel C. (2002) Painful stimuli evoke different stimulus-response functions in the amygdala, prefrontal, insula and somatosensory cortex: a single-trial fMRI study. *Brain* **125,** 1326-1336.

Buchel C., Bornhovd K., Quante M., Glauche V., Bromm B. and Weiller C. (2002) Dissociable neural responses related to pain intensity, stimulus intensity, and stimulus awareness within the anterior cingulate cortex: a parametric single-trial laser functional magnetic resonance imaging study. *J. Neurosci.* **22,** 970-976.

Caspary L., Thum J., Creutzig A., Lubbers D. W. and Alexander K. (1995) Quantitative reflection spectrophotometry: spatial and temporal variation of Hb oxygenation in human skin. *Int. J. Microcirc. Clin. Exp.* **15,** 131-136.

Chen H. I., Malhotra N. R., Oddo M., Heuer G. G., Levine J. M. and LeRoux P. D. (2008) Barbiturate infusion for intractable intracranial hypertension and its effect on brain oxygenation. *Neurosurgery* **63,** 880-886.

Chen J. I., Ha B., Bushnell M. C., Pike B. and Duncan G. H. (2002) Differentiating noxious- and innocuous-related activation of human somatosensory cortices using temporal analysis of fMRI. *J. Neurophysiol.* **88,** 464-474.

Chen Y., Aguirre A. D., Ruvinskaya L., Devor A., Boas D. A. and Fujimoto J. G. (2009) Optical coherence tomography (OCT) reveals depth-resolved dynamics during functional brain activation. *J. Neurosci. Methods* **178,** 162-173.

Chung J. M., Surmeier D. J., Lee K. H., Sorkin L. S., Honda C. N., Tsong Y. and Willis W. D. (1986) Classification of primate spinothalamic and somatosensory thalamic neurons based on cluster analysis. *J. Neurophysiol.* **56,** 308-327.

Clemo H. R. and Stein B. E. (1991) Receptive field properties of somatosensory neurons in the cat superior colliculus. *J. Comp Neurol.* **314,** 534-544.

Clerbaux T., Detry B., Geubel A., Veriter C., Liistro G., Horsmans Y. and Frans A. (2006) The oxyhemoglobin dissociation curve in liver cirrhosis. *Chest* **129,** 438-445.

Cohen L. B. and Keynes R. D. (1971) Changes in light scattering associated with the action potential in crab nerves. *J. Physiol* **212,** 259-275.

Cohen L. B., Keynes R. D. and Landowne D. (1972a) Changes in axon light scattering that accompany the action potential: current-dependent components. *J. Physiol* **224,** 727-752.

Cohen L. B., Keynes R. D. and Landowne D. (1972b) Changes in light scattering that accompany the action potential in squid giant axons: potential-dependent components. *J. Physiol* **224,** 701-725.

Davis S. L., Fadel P. J., Cui J., Thomas G. D. and Crandall C. G. (2006) Skin blood flow influences near-infrared spectroscopy-derived measurements of tissue oxygenation during heat stress. *J. Appl. Physiol* **100,** 221-224.

Detre J. A., Ances B. M., Takahashi K. and Greenberg J. H. (1998) Signal averaged laser Doppler measurements of activation-flow coupling in the rat forepaw somatosensory cortex. *Brain Res.* **796,** 91-98.

Detry J. M., Brengelmann G. L., Rowell L. B. and Wyss C. (1972) Skin and muscle components of forearm blood flow in directly heated resting man. *J. Appl. Physiol* **32,** 506-511.

Dickenson A. H. and Sullivan A. F. (1987) Peripheral origins and central modulation of subcutaneous formalin-induced activity of rat dorsal horn neurones. *Neurosci. Lett.* **83,** 207-211.

Dubuisson D. and Dennis S. G. (1977) The formalin test: a quantitative study of the analgesic effects of morphine, meperidine, and brain stem stimulation in rats and cats. *Pain* **4,** 161-174.

Durduran T., Yodh A. G., Chance B. and Boas D. A. (1997) Does the photon-diffusion coefficient depend on absorption? *J. Opt. Soc. Am. A Opt. Image Sci. Vis.* **14,** 3358-3365.

Dykes R. W. (1978) The anatomy and physiology of the somatic sensory cortical regions. *Prog. Neurobiol.* **10,** 33-88.

Dykes R. W., Landry P., Hicks T. P., Diadori P. and Metherate R. (1988) Specificity of connections in the ventroposterior nuclei of the thalamus. *Prog. Neurobiol.* **30,** 87-103.

Feng S., Zeng F.-A. and Chance B. (1995) Photon migration in the presence of a single defect: a perturbation analysis. *Appl. Opt.* **34,** 3826-3837.

Fox P. T. and Raichle M. E. (1986) Focal physiological uncoupling of cerebral blood flow and oxidative metabolism during somatosensory stimulation in human subjects. *Proc. Natl. Acad. Sci. U. S. A* **83,** 1140-1144.

Fu K. Y., Light A. R. and Maixner W. (2001) Long-lasting inflammation and long-term hyperalgesia after subcutaneous formalin injection into the rat hindpaw. *J. Pain* **2,** 2-11.

Gambichler T., Moussa G., Sand M., Sand D., Orlikov A., Altmeyer P. and Hoffmann K. (2005) Correlation between clinical scoring of allergic patch test reactions and optical coherence tomography. *J. Biomed. Opt.* **10,** 064030.

Gebhart S. C., Lin W. C. and Mahadevan-Jansen A. (2006) In vitro determination of normal and neoplastic human brain tissue optical properties using inverse adding-doubling. *Phys. Med. Biol.* **51,** 2011-2027.

Georgopoulos A. P. (1976) Functional properties of primary afferent units probably related to pain mechanisms in primate glabrous skin. *J. Neurophysiol.* **39,** 71-83.

Gobel U., Theilen H. and Kuschinsky W. (1990) Congruence of total and perfused capillary network in rat brains. *Circ. Res.* **66,** 271-281.

Goense J. B. and Logothetis N. K. (2008) Neurophysiology of the BOLD fMRI signal in awake monkeys. *Curr. Biol.* **18,** 631-640.

Graf B. W., Ralston T. S., Ko H. J. and Boppart S. A. (2009) Detecting intrinsic scattering changes correlated to neuron action potentials using optical coherence imaging. *Opt. Express* **17,** 13447-13457.

Groenewegen H. J., Wright C. I. and Uylings H. B. (1997) The anatomical relationships of the prefrontal cortex with limbic structures and the basal ganglia. *J. Psychopharmacol.* **11,** 99-106.

Groenewegen H. J. W. M. P. (2004) Thalamus, in *The Rat Nervous System,* (Paxinos G., ed), pp. 407-453. Academic Press, San Diego, CA.

Hamberg L. M., Hunter G. J., Kierstead D., Lo E. H., Gilberto G. R. and Wolf G. L. (1996) Measurement of cerebral blood volume with subtraction three-dimensional functional CT. *AJNR Am. J. Neuroradiol.* **17,** 1861-1869.

Hamilton C., Steinlechner B., Gruber E., Simon P. and Wollenek G. (2004) The oxygen dissociation curve: quantifying the shift. *Perfusion* **19,** 141-144.

Harris F. A. (1978) Functional subsets of neurons in somatosensory thalamus of the cat. *Exp. Neurol.* **58,** 149-170.

Harris F. A. (1980) Wide-field neurons in somatosensory thalamus of domestic cats under barbiturate anesthesia. *Exp. Neurol.* **68,** 27-49.

Harrison D. K., Evans S. D., Abbot N. C., Beck J. S. and McCollum P. T. (1992) Spectrophotometric measurements of haemoglobin saturation and concentration in skin during the tuberculin reaction in normal human subjects. *Clin. Phys. Physiol Meas.* **13,** 349-363.

Hess A., Sergejeva M., Budinsky L., Zeilhofer H. U. and Brune K. (2007) Imaging of hyperalgesia in rats by functional MRI. *Eur. J. Pain* **11,** 109-119.

Hill D. K. and Keynes R. D. (1949) Opacity changes in stimulated nerve. *J. Physiol* **108,** 278-281.

Hlushchuk Y. and Hari R. (2006) Transient suppression of ipsilateral primary somatosensory cortex during tactile finger stimulation. *J. Neurosci.* **26,** 5819-5824.

Horovitz S. G. and Gore J. C. (2004) Simultaneous event-related potential and near-infrared spectroscopic studies of semantic processing. *Hum. Brain Mapp.* **22,** 110-115.

Hou H., Grinberg O. Y., Taie S., Leichtweis S., Miyake M., Grinberg S., Xie H., Csete M. and Swartz H. M. (2003) Electron paramagnetic resonance assessment of brain tissue oxygen tension in anesthetized rats. *Anesth. Analg.* **96,** 1467-72, table.

Huang D., Swanson E. A., Lin C. P., Schuman J. S., Stinson W. G., Chang W., Hee M. R., Flotte T., Gregory K., Puliafito C. A. and . (1991) Optical coherence tomography. *Science* **254,** 1178-1181.

Hudetz A. G. (1999) Mathematical model of oxygen transport in the cerebral cortex. *Brain Res.* **817,** 75-83.

Hunskaar S. and Hole K. (1987) The formalin test in mice: dissociation between inflammatory and non-inflammatory pain. *Pain* **30,** 103-114.

Huppert T. J., Hoge R. D., Diamond S. G., Franceschini M. A. and Boas D. A. (2006) A temporal comparison of BOLD, ASL, and NIRS hemodynamic responses to motor stimuli in adult humans. *Neuroimage.* **29,** 368-382.

Iadecola C. (2004) Neurovascular regulation in the normal brain and in Alzheimer's disease. *Nat. Rev. Neurosci.* **5,** 347-360.

Jacques L., Couture R., Drapeau G. and Regoli D. (1989) Capillary permeability induced by intravenous neurokinins. Receptor characterization and mechanism of action. *Naunyn Schmiedebergs Arch. Pharmacol.* **340,** 170-179.

Kandel E. R., Schwartz J. H. and Jessell T. M. (2010) Coding of Sensory Information, in *Principles of Neural Science,* pp. 411-429. McGraw-Hill.

Keys A. (1938) The Oxygen Saturation of the Venous Blood in Normal Human Subjects. *Am. J. Physiol* 13-21.

Keys A. and Snell A. M. (1937) Respiratory Properties of the Arterial Blood in Normal Man and in Patients with Disease of the Liver: Position of the Oxygen Dissociation Curve. *J. Clin. Invest* **17,** 59-67.

Killackey H. P., Gould H. J., III, Cusick C. G., Pons T. P. and Kaas J. H. (1983) The relation of corpus callosum connections to architectonic fields and body surface maps in sensorimotor cortex of new and old world monkeys. *J. Comp Neurol.* **219,** 384-419.

Kim J. G., Xia M. and Liu H. (2005) Extinction coefficients of hemoglobin for near-infrared spectroscopy of tissue. *IEEE Eng Med. Biol. Mag.* **24,** 118-121.

Kim T., Hendrich K. S., Masamoto K. and Kim S. G. (2007) Arterial versus total blood volume changes during neural activity-induced cerebral blood flow change: implication for BOLD fMRI. *J. Cereb. Blood Flow Metab* **27,** 1235-1247.

Klein B., Kuschinsky W., Schrock H. and Vetterlein F. (1986) Interdependency of local capillary density, blood flow, and metabolism in rat brains. *Am. J. Physiol* **251,** H1333-H1340.

Koopmans G., Hasse B. and Sinis N. (2009) Chapter 19: The role of collagen in peripheral nerve repair. *Int. Rev. Neurobiol.* **87,** 363-379.

Kuo C. C. and Yen C. T. (2005) Comparison of anterior cingulate and primary somatosensory neuronal responses to noxious laser-heat stimuli in conscious, behaving rats. *J. Neurophysiol.* **94,** 1825-1836.

Kurvers H. A., Tangelder G. J., De Mey J. G., Slaaf D. W., van den Wildenberg F. A., Kitslaar P. J., Reneman R. S., Rouwet E. V. and Jacobs M. J. (1996) Skin blood flow disturbances in the contralateral limb in a peripheral mononeuropathy in the rat. *Neuroscience* **74,** 935-943.

LaCroix J. T. and Haidekker M. A. (2009) Quantifying light scattering with single-mode fiber - optic confocal microscopy. *BMC. Med. Imaging* **9,** 19.

Lamah M., Mortimer P. S. and Dormandy J. A. (1996) Heterogeneity of capillary density of skin over the dorsum of the foot and toes of healthy subjects. *Int. J. Microcirc. Clin. Exp.* **16,** 271-276.

Lamah M., Mortimer P. S. and Dormandy J. A. (2000) Interpretation of quantitative measurement of skin capillaries using native in vivo microscopy. *Microvasc. Res.* **60,** 189-192.

Lei H., Grinberg O., Nwaigwe C. I., Hou H. G., Williams H., Swartz H. M., Dunn J. F., Grebstad J. A., Svendsen L. and Gulsvik A. (2001) The effects of ketamine-xylazine anesthesia on cerebral blood flow and oxygenation observed using nuclear magnetic resonance perfusion imaging and electron paramagnetic resonance oximetry precision of arterial blood gases and cutaneous oxygen saturation in healthy non-smokers. *Brain Res.* **913,** 174-179.

Lembeck F. and Holzer P. (1979) Substance P as neurogenic mediator of antidromic vasodilation and neurogenic plasma extravasation. *Naunyn Schmiedebergs Arch. Pharmacol.* **310,** 175-183.

Li A., Zhang Q., Culver J. P., Miller E. L. and Boas D. A. (2004) Reconstructing chromosphere concentration images directly by continuous-wave diffuse optical tomography. *Opt. Lett.* **29,** 256-258.

Lilienthal J. L. and Riley R. L. (1944) ON THE DETERMINATION OF ARTERIAL OXYGEN SATURATIONS FROM SAMPLES OF "CAPILLARY" BLOOD. *J. Clin. Invest* **23,** 904-906.

Lima A. and Bakker J. (2005) Noninvasive monitoring of peripheral perfusion. *Intensive Care Med.* **31,** 1316-1326.

Lin Q., Wu J. and Willis W. D. (1999) Dorsal root reflexes and cutaneous neurogenic inflammation after intradermal injection of capsaicin in rats. *J. Neurophysiol.* **82,** 2602-2611.

Lin Q., Zou X., Fang L. and Willis W. D. (2003) Sympathetic modulation of acute cutaneous flare induced by intradermal injection of capsaicin in anesthetized rats. *J. Neurophysiol.* **89,** 853-861.

Liu H., Radhakrishnan H., Senapati A. K., Hagains C. E., Peswani D., Mathker A. and Peng Y. B. (2008) Near infrared and visible spectroscopic measurements to detect changes in light scattering and hemoglobin oxygen saturation from rat spinal cord during peripheral stimulation. *Neuroimage.* **40,** 217-227.

Logothetis N. K., Pauls J., Augath M., Trinath T. and Oeltermann A. (2001) Neurophysiological investigation of the basis of the fMRI signal. *Nature* **412,** 150-157.

Longnecker D. E. and Harris P. D. (1980) Microcirculatory actions of general anesthetics. *Fed. Proc.* **39,** 1580-1583.

Lovell A. T., Owen-Reece H., Elwell C. E., Smith M. and Goldstone J. C. (1999) Continuous measurement of cerebral oxygenation by near infrared spectroscopy during induction of anesthesia. *Anesth. Analg.* **88,** 554-558.

Lowe A. S., Beech J. S. and Williams S. C. (2007) Small animal, whole brain fMRI: innocuous and nociceptive forepaw stimulation. *Neuroimage.* **35,** 719-728.

Lui F., Duzzi D., Corradini M., Serafini M., Baraldi P. and Porro C. A. (2008) Touch or pain? Spatio-temporal patterns of cortical fMRI activity following brief mechanical stimuli. *Pain* **138,** 362-374.

Lundsgaard C. and Moller E. (1922) INVESTIGATIONS ON THE OXYGEN CONTENT OF CUTANEOUS BLOOD (SO CALLED CAPILLARY BLOOD). *J. Exp. Med.* **36,** 559-573.

Maheswari R. U., Takaoka H., Kadono H., Homma R. and Tanifuji M. (2003) Novel functional imaging technique from brain surface with optical coherence tomography enabling visualization of depth resolved functional structure in vivo. *J. Neurosci. Methods* **124,** 83-92.

Maihofner C. and Kaltenhauser M. (2009) Quality discrimination for noxious stimuli in secondary somatosensory cortex: A MEG-study. *Eur. J. Pain*.

Malisza K. L., Gregorash L., Turner A., Foniok T., Stroman P. W., Allman A. A., Summers R. and Wright A. (2003) Functional MRI involving painful stimulation of the ankle and the effect of physiotherapy joint mobilization. *Magn Reson. Imaging* **21,** 489-496.

Mehagnoul-Schipper D. J., van der Kallen B. F., Colier W. N., van der Sluijs M. C., van Erning L. J., Thijssen H. O., Oeseburg B., Hoefnagels W. H. and Jansen R. W. (2002) Simultaneous measurements of cerebral oxygenation changes during brain activation by near-infrared spectroscopy and functional magnetic resonance imaging in healthy young and elderly subjects. *Hum. Brain Mapp.* **16,** 14-23.

Mintun M. A., Lundstrom B. N., Snyder A. Z., Vlassenko A. G., Shulman G. L. and Raichle M. E. (2001) Blood flow and oxygen delivery to human brain during functional activity: theoretical modeling and experimental data. *Proc. Natl. Acad. Sci. U. S. A* **98,** 6859-6864.

Mohr C., Binkofski F., Erdmann C., Buchel C. and Helmchen C. (2005) The anterior cingulate cortex contains distinct areas dissociating external from self-administered painful stimulation: a parametric fMRI study. *Pain* **114,** 347-357.

Morrow T. J., Paulson P. E., Danneman P. J. and Casey K. L. (1998) Regional changes in forebrain activation during the early and late phase of formalin nociception: analysis using cerebral blood flow in the rat. *Pain* **75,** 355-365.

Nagashima Y., Yada Y., Hattori M. and Sakai A. (2000) Development of a new instrument to measure oxygen saturation and total hemoglobin volume in local skin by near-infrared spectroscopy and its clinical application. *Int. J. Biometeorol.* **44,** 11-19.

Newton D. J., Harrison D. K. and McCollum P. T. (1996) Oxygen extraction rates in inflamed human skin using the tuberculin reaction as a model. *Int. J. Microcirc. Clin. Exp.* **16,** 118-123.

Nihashi T., Naganawa S., Sato C., Kawai H., Nakamura T., Fukatsu H., Ishigaki T. and Aoki I. (2005) Contralateral and ipsilateral responses in primary somatosensory cortex following electrical median nerve stimulation--an fMRI study. *Clin. Neurophysiol.* **116,** 842-848.

Niu H., Tian F., Lin Z. and Liu H. (2010) Development of a compensation algorithm for accurate depth localization in diffuse optical tomography. *Optics Letters* **35,** 429-431.

Ogawa S., Lee T. M., Kay A. R. and Tank D. W. (1990) Brain magnetic resonance imaging with contrast dependent on blood oxygenation. *Proc. Natl. Acad. Sci. U. S. A* **87,** 9868-9872.

Ogrin R., Darzins P. and Khalil Z. (2005) Age-related changes in microvascular blood flow and transcutaneous oxygen tension under Basal and stimulated conditions. *J. Gerontol. A Biol. Sci. Med. Sci.* **60,** 200-206.

Pasley B. N., Inglis B. A. and Freeman R. D. (2007) Analysis of oxygen metabolism implies a neural origin for the negative BOLD response in human visual cortex. *Neuroimage.* **36,** 269-276.

Paxinos G. W. C. (1998) in *The Rat Brain in Stereotaxic Coordinates,* Academic Press, San Diego, CA.

Peng Y. B., Kenshalo D. R. and Gracely R. H. (2003) Periaqueductal gray-evoked dorsal root reflex is frequency dependent. *Brain Res.* **976,** 217-226.

Peng Y. B., Lin Q. and Willis W. D. (1996a) Effects of GABA and glycine receptor antagonists on the activity and PAG-induced inhibition of rat dorsal horn neurons. *Brain Res.* **736,** 189-201.

Peng Y. B., Lin Q. and Willis W. D. (1996b) The role of 5-HT3 receptors in periaqueductal gray-induced inhibition of nociceptive dorsal horn neurons in rats. *J. Pharmacol. Exp. Ther.* **276,** 116-124.

Peng Y. B., Ringkamp M., Campbell J. N. and Meyer R. A. (1999) Electrophysiological assessment of the cutaneous arborization of Adelta-fiber nociceptors. *J. Neurophysiol.* **82,** 1164-1177.

Peyron R., Garcia-Larrea L., Gregoire M. C., Costes N., Convers P., Lavenne F., Mauguiere F., Michel D. and Laurent B. (1999) Haemodynamic brain responses to acute pain in humans: sensory and attentional networks. *Brain* **122 ( Pt 9),** 1765-1780.

Peyron R., Laurent B. and Garcia-Larrea L. (2000) Functional imaging of brain responses to pain. A review and meta-analysis (2000). *Neurophysiol. Clin.* **30,** 263-288.

Pitcher G. M. and Henry J. L. (2002) Second phase of formalin-induced excitation of spinal dorsal horn neurons in spinalized rats is reversed by sciatic nerve block. *Eur. J. Neurosci.* **15,** 1509-1515.

Plesnila N., Putz C., Rinecker M., Wiezorrek J., Schleinkofer L., Goetz A. E. and Kuebler W. M. (2002) Measurement of absolute values of hemoglobin oxygenation in the brain of small rodents by near infrared reflection spectrophotometry. *J. Neurosci. Methods* **114,** 107-117.

Quaresima V., Lepanto R. and Ferrari M. (2003) The use of near infrared spectroscopy in sports medicine. *J. Sports Med. Phys. Fitness* **43,** 1-13.

Rajagopalan U. M. and Tanifuji M. (2007) Functional optical coherence tomography reveals localized layer-specific activations in cat primary visual cortex in vivo. *Opt. Lett.* **32,** 2614-2616.

Rendell M. S., Finnegan M. F., Pisarri T., Healy J. C., Lind A., Milliken B. K., Finney D. E. and Bonner R. F. (1999) A comparison of the cutaneous microvascular properties of the spontaneously hypertensive rat and the Wistar-Kyoto rat. *Comp Biochem. Physiol A Mol. Integr. Physiol* **122,** 399-406.

Rose J. E. and Woolsey C. N. (1948) The orbitofrontal cortex and its connections with the mediodorsal nucleus in rabbit, sheep and cat. *Res. Publ. Ass. nerv. ment. Dis.* **27,** 210-232.

Rovati L., Salvatori G., Bulf L. and Fonda S. (2007) Optical and electrical recording of neural activity evoked by graded contrast visual stimulus. *Biomed. Eng Online.* **6,** 28.

Ruehle B. S., Handwerker H. O., Lennerz J. K., Ringler R. and Forster C. (2006) Brain activation during input from mechanoinsensitive versus polymodal C-nociceptors. *J. Neurosci.* **26,** 5492-5499.

Sabatini U., Celsis P., Viallard G., Rascol A. and Marc-Vergnes J. P. (1991) Quantitative assessment of cerebral blood volume by single-photon emission computed tomography. *Stroke* **22,** 324-330.

Sakatani K., Murata Y., Fujiwara N., Hoshino T., Nakamura S., Kano T. and Katayama Y. (2007) Comparison of blood-oxygen-level-dependent functional magnetic resonance imaging and near-infrared spectroscopy recording during functional brain activation in patients with stroke and brain tumors. *J. Biomed. Opt.* **12,** 062110.

Schlosser S., Spanholtz T., Merz K., Dennler C., Banic A., Erni D. and Plock J. A. (2009) The Choice of Anesthesia Influences Oxidative Energy Metabolism and Tissue Survival in Critically Ischemic Murine Skin. *J. Surg. Res.*

Schridde U., Khubchandani M., Motelow J. E., Sanganahalli B. G., Hyder F. and Blumenfeld H. (2008) Negative BOLD with large increases in neuronal activity. *Cereb. Cortex* **18,** 1814-1827.

Schroeter M. L., Kupka T., Mildner T., Uludag K. and von Cramon D. Y. (2006) Investigating the post-stimulus undershoot of the BOLD signal--a simultaneous fMRI and fNIRS study. *Neuroimage.* **30,** 349-358.

Seifert F. and Maihofner C. (2009) Central mechanisms of experimental and chronic neuropathic pain: findings from functional imaging studies. *Cell Mol. Life Sci.* **66,** 375-390.

Seiyama A., Seki J., Tanabe H. C., Sase I., Takatsuki A., Miyauchi S., Eda H., Hayashi S., Imaruoka T., Iwakura T. and Yanagida T. (2004) Circulatory basis of fMRI signals: relationship between changes in the hemodynamic parameters and BOLD signal intensity. *Neuroimage.* **21,** 1204-1214.

Severinghaus J. W., Astrup P. and Murray J. F. (1998) Blood gas analysis and critical care medicine. *Am. J. Respir. Crit Care Med.* **157,** S114-S122.

Severinghaus J. W., Severinghaus J. W. and BRADLEY A. F. (1979) Simple, accurate equations for human blood O2 dissociation computations
Electrodes for blood pO2 and pCO2 determination. *J. Appl. Physiol* **46,** 599-602.

Shah Y. B., Haynes L., Prior M. J., Marsden C. A., Morris P. G. and Chapman V. (2005) Functional magnetic resonance imaging studies of opioid receptor-mediated modulation of noxious-evoked BOLD contrast in rats. *Psychopharmacology (Berl)* **180,** 761-773.

Shiao S. Y. and Ou C. N. (2007) Validation of oxygen saturation monitoring in neonates. *Am. J. Crit Care* **16,** 168-178.

Shih Y. Y., Chang C., Chen J. C. and Jaw F. S. (2008) BOLD fMRI mapping of brain responses to nociceptive stimuli in rats under ketamine anesthesia. *Med. Eng Phys.* **30,** 953-958.

Shmuel A., Augath M., Oeltermann A. and Logothetis N. K. (2006) Negative functional MRI response correlates with decreases in neuronal activity in monkey visual area V1. *Nat. Neurosci.* **9,** 569-577.

Shyu B. C., Chen W. F. and Shih H. C. (2008) Electrically and mechanically evoked nociceptive neuronal responses in the rat anterior cingulate cortex. *Acta Neurochir. Suppl* **101,** 23-25.

Siggaard-Andersen M. and Siggaard-Andersen O. (1995) Oxygen status algorithm, version 3, with some applications. *Acta Anaesthesiol. Scand. Suppl* **107,** 13-20.

Siggaard-Andersen O. and Gothgen I. H. (1995) Oxygen and acid-base parameters of arterial and mixed venous blood, relevant versus redundant. *Acta Anaesthesiol. Scand. Suppl* **107,** 21-27.

Sikes R. W., Vogt L. J. and Vogt B. A. (2008) Distribution and properties of visceral nociceptive neurons in rabbit cingulate cortex. *Pain* **135,** 160-174.

Sivaramakrishnan M., Maslov K., Zhang H. F., Stoica G. and Wang L. V. (2007) Limitations of quantitative photoacoustic measurements of blood oxygenation in small vessels. *Phys. Med. Biol.* **52,** 1349-1361.

Slater R., Cantarella A., Gallella S., Worley A., Boyd S., Meek J. and Fitzgerald M. (2006) Cortical pain responses in human infants. *J. Neurosci.* **26,** 3662-3666.

Srinivasan V. J., Chen Y., Duker J. S. and Fujimoto J. G. (2009) In vivo functional imaging of intrinsic scattering changes in the human retina with high-speed ultrahigh resolution OCT. *Opt. Express* **17,** 3861-3877.

Srinivasan V. J., Wojtkowski M., Fujimoto J. G. and Duker J. S. (2006) In vivo measurement of retinal physiology with high-speed ultrahigh-resolution optical coherence tomography. *Opt. Lett.* **31,** 2308-2310.

Steinhoff M., Stander S., Seeliger S., Ansel J. C., Schmelz M. and Luger T. (2003) Modern aspects of cutaneous neurogenic inflammation. *Arch. Dermatol.* **139,** 1479-1488.

Strangman G., Culver J. P., Thompson J. H. and Boas D. A. (2002) A quantitative comparison of simultaneous BOLD fMRI and NIRS recordings during functional brain activation. *Neuroimage.* **17,** 719-731.

Sutherland M. T. and Tang A. C. (2006) Reliable detection of bilateral activation in human primary somatosensory cortex by unilateral median nerve stimulation. *Neuroimage.* **33,** 1042-1054.

Takano T., Tian G. F., Peng W., Lou N., Libionka W., Han X. and Nedergaard M. (2006) Astrocyte-mediated control of cerebral blood flow. *Nat. Neurosci.* **9,** 260-267.

Takeuchi M., Hori E., Takamoto K., Tran A. H., Satoru K., Ishikawa A., Ono T., Endo S. and Nishijo H. (2009) Brain cortical mapping by simultaneous recording of functional near infrared spectroscopy and electroencephalograms from the whole brain during right median nerve stimulation. *Brain Topogr.* **22,** 197-214.

Taylor B. K., Peterson M. A., Roderick R. E., Tate J., Green P. G., Levine J. O. and Basbaum A. I. (2000) Opioid inhibition of formalin-induced changes in plasma extravasation and local blood flow in rats. *Pain* **84,** 263-270.

Thum J., Caspary L., Creutzig A., Stappler T. and Alexander K. (1997) Non-invasive determination of dermal hemoglobin oxygenation and concentration in patients with peripheral arterial occlusive disease. *Vasa* **26,** 11-17.

Tian F., Alexandrakis G. and Liu H. (2009a) Optimization of probe geometry for diffuse optical brain imaging based on measurement density and distribution. *Appl. Opt.* **48,** 2496-2504.

Tian F., Chance B. and Liu H. (2009b) Investigation of the prefrontal cortex in response to duration-variable anagram tasks using functional near-infrared spectroscopy. *J. Biomed. Opt.* **14,** 054016.

Timmermann L., Ploner M., Haucke K., Schmitz F., Baltissen R. and Schnitzler A. (2001) Differential coding of pain intensity in the human primary and secondary somatosensory cortex. *J. Neurophysiol.* **86,** 1499-1503.

Toronov V. Y., Zhang X. and Webb A. G. (2007) A spatial and temporal comparison of hemodynamic signals measured using optical and functional magnetic resonance imaging during activation in the human primary visual cortex. *Neuroimage.* **34,** 1136-1148.

Tracey I. and Mantyh P. W. (2007) The cerebral signature for pain perception and its modulation. *Neuron* **55,** 377-391.

Tromberg B. J., Cerussi A., Shah N., Compton M., Durkin A., Hsiang D., Butler J. and Mehta R. (2005) Imaging in breast cancer: diffuse optics in breast cancer: detecting tumors in pre-menopausal women and monitoring neoadjuvant chemotherapy. *Breast Cancer Res.* **7,** 279-285.

Van der Schueren B. J., Rogiers A., Vanmolkot F. H., Van Hecken A., Depre M., Kane S. A., De L., I, Sinclair S. R. and de Hoon J. N. (2008) Calcitonin gene-related peptide8-37

antagonizes capsaicin-induced vasodilation in the skin: evaluation of a human in vivo pharmacodynamic model. *J. Pharmacol. Exp. Ther.* **325,** 248-255.

Villringer A., Planck J., Hock C., Schleinkofer L. and Dirnagl U. (1993) Near infrared spectroscopy (NIRS): a new tool to study hemodynamic changes during activation of brain function in human adults. *Neurosci. Lett.* **154,** 101-104.

Wallace M. T., Wilkinson L. K. and Stein B. E. (1996) Representation and integration of multiple sensory inputs in primate superior colliculus. *J. Neurophysiol.* **76,** 1246-1266.

Wallengren J. and Hakanson R. (1987) Effects of substance P, neurokinin A and calcitonin gene-related peptide in human skin and their involvement in sensory nerve-mediated responses. *Eur. J. Pharmacol.* **143,** 267-273.

Welzel J., Bruhns M. and Wolff H. H. (2003) Optical coherence tomography in contact dermatitis and psoriasis. *Arch. Dermatol. Res.* **295,** 50-55.

Wheeler-Aceto H. and Cowan A. (1991) Neurogenic and tissue-mediated components of formalin-induced edema: evidence for supraspinal regulation. *Agents Actions* **34,** 264-269.

Wolf U., Wolf M., Choi J. H., Levi M., Choudhury D., Hull S., Coussirat D., Paunescu L. A., Safonova L. P., Michalos A., Mantulin W. W. and Gratton E. (2003) Localized irregularities in hemoglobin flow and oxygenation in calf muscle in patients with peripheral vascular disease detected with near-infrared spectrophotometry. *J. Vasc. Surg.* **37,** 1017-1026.

Wyatt J. S., Cope M., Delpy D. T., Richardson C. E., Edwards A. D., Wray S. and Reynolds E. O. (1990) Quantitation of cerebral blood volume in human infants by near-infrared spectroscopy. *J. Appl. Physiol* **68,** 1086-1091.

Xu C., Yuan B. and Zhu Q. (2008) Optimal probe design for breast imaging using near-infrared diffused light. *J. Biomed. Opt.* **13,** 044002.

Yao X. C., Yamauchi A., Perry B. and George J. S. (2005) Rapid optical coherence tomography and recording functional scattering changes from activated frog retina. *Appl. Opt.* **44,** 2019-2023.

Yoxall C. W. and Weindling A. M. (1997) Measurement of venous oxyhaemoglobin saturation in the adult human forearm by near infrared spectroscopy with venous occlusion. *Med. Biol. Eng Comput.* **35,** 331-336.

Zavorsky G. S., Cao J., Mayo N. E., Gabbay R. and Murias J. M. (2007) Arterial versus capillary blood gases: a meta-analysis. *Respir. Physiol Neurobiol.* **155,** 268-279.

Zegarska B., Lelinska A. and Tyrakowski T. (2006) Clinical and experimental aspects of cutaneous neurogenic inflammation. *Pharmacol. Rep.* **58,** 13-21.

Zheng Y., Johnston D., Berwick J., Chen D., Billings S. and Mayhew J. (2005) A three-compartment model of the hemodynamic response and oxygen delivery to brain. *Neuroimage.* **28,** 925-939.

Zhu Z., Disbrow E. A., Zumer J. M., McGonigle D. J. and Nagarajan S. S. (2007) Spatiotemporal integration of tactile information in human somatosensory cortex. *BMC. Neurosci.* **8,** 21.

Zimmermann M. (1983) Ethical guidelines for investigations of experimental pain in conscious animals. *Pain* **16,** 109-110.

Zoccoli G., Lucchi M. L., Andreoli E., Lenzi P. and Franzini C. (2000) Density of perfused brain capillaries in the aged rat during the wake-sleep cycle. *Exp. Brain Res.* **130,** 73-77.

Zonios G. and Dimou A. (2006) Modeling diffuse reflectance from semi-infinite turbid media: application to the study of skin optical preperties. *Optics Express* **14,** 8661-8674.

## BIOGRAPHICAL INFORMATION

Ji-Wei He earned his undergrad degrees in Electronic Engineering and English at the University of Electronic Science and Technology of China (UESTC). After one year in the Graduate School of UESTC, he withdrew and joined Dr. Yuan Bo Peng's lab at the University of Texas at Arlington to pursue his PhD degree on neuroscience. His academic interests were gradually established as his active involvements in multiple projects and collaborations with other faculties. He had been primarily trained as an electrophysiologist to study the physiology of pain and descending inhibitory pain mechanism in the central nervous system. In his PhD dissertation, he started to use several optical methods to study neurovascular correlate in the central nervous system during pain processing. He, therefore, became interested in multimodal studies and computational modeling to reveal neural networks and their communications during functioning at a system level.